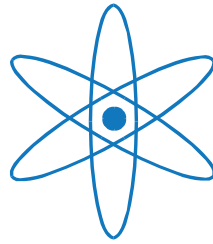


PHYSIK-DEPARTMENT



Femtosecond and Attosecond Electron  
Dynamics in Semiconductors and Dielectrics

Dissertation

von

Elisabeth Monika Ludmilla Bothschafter



TECHNISCHE UNIVERSITÄT  
MÜNCHEN



**Technische Universität München**

**Department für Physik**

**Lehrstuhl für Laser- und Röntgenphysik E11**

# **Femtosecond and Attosecond Electron Dynamics in Semiconductors and Dielectrics**

**Elisabeth Monika Ludmilla Bothschafter**

Vollständiger Abdruck der von der Fakultät für Physik der  
Technischen Universität München zur Erlangung des akademischen Grades eines

**Doktors der Naturwissenschaften**

genehmigten Dissertation.

Vorsitzender: Univ.-Prof. Dr. Peter Vogl

Prüfer der Dissertation:

1. Univ.-Prof. Dr. Reinhard Kienberger
2. Univ.-Prof. Jonathan J. Finley, Ph.D.

Die Dissertation wurde am 18.12.2013 bei der Technischen Universität München eingereicht und durch die Fakultät für Physik am 06.05.2014 angenommen.



*"Wahrheit und Klarheit sind komplementär"*  
attributed to Niels Bohr  
in *Dreams of a Final Theory* by Steven Weinberg,  
Vintage Books, New York (1994) p. 74

# Contents

<b>Zusammenfassung</b>	<b>i</b>
<b>Abstract</b>	<b>v</b>
<b>Introduction</b>	<b>1</b>
<b>1 Fundamentals of ultrashort laser pulse generation and characterization</b>	<b>5</b>
1.1 Waveform controlled few-cycle pulses in the near infrared . . . . .	6
1.1.1 Mathematical description of laser pulses . . . . .	6
1.1.2 The laser system . . . . .	7
1.1.3 Carrier-envelope phase stabilization . . . . .	10
1.2 Generation of few-femtosecond pulses in the ultraviolet . . . . .	13
1.3 Generation of isolated attosecond pulses with few-cycle laser pulses . . . . .	15
1.3.1 The three-step model of high harmonic generation . . . . .	15
1.3.2 Isolated attosecond pulses . . . . .	16
1.3.3 Setup for high harmonic generation in atomic gases . . . . .	18
1.4 Femtosecond and attosecond pulse metrology . . . . .	19
1.4.1 Frequency resolved optical gating of few-cycle NIR/VIS pulses . . . . .	19
1.4.2 XUV pulse characterization with the attosecond streak camera . . . . .	19
<b>2 Light-matter interaction at the femtosecond and attosecond timescale</b>	<b>25</b>
2.1 Coherent phonon generation and detection . . . . .	26
2.2 Nonlinear ultrashort pulse propagation in transparent media . . . . .	30
2.2.1 The nonlinear wave equation . . . . .	30

2.3	Strong-field induced electron dynamics in dielectric solids . . . . .	33
2.3.1	Femtosecond dielectric breakdown in SiO <sub>2</sub> . . . . .	33
2.3.2	Femtosecond polarization and ionization dynamics . . . . .	34
<b>3</b>	<b>Interplay between electronic and lattice dynamics in a resonantly excited semiconductor</b>	<b>37</b>
3.1	Setup for ultraviolet pump-probe transient reflectance experiments . . . . .	38
3.2	Electron-phonon correlations in TiO <sub>2</sub> . . . . .	40
3.3	Ultrafast evolution of the excited-state potential energy surface of TiO <sub>2</sub> . .	41
<b>4</b>	<b>Strong-field induced electron dynamics in SiO<sub>2</sub></b>	<b>51</b>
4.1	Experimental setup for broadband attosecond probe spectroscopy . . . . .	53
4.1.1	XUV-NIR Mach-Zehnder interferometer . . . . .	53
4.1.2	Simultaneous attosecond streaking and transient absorption spectroscopy . . . . .	55
4.1.3	Detection of optical breakdown in nanometric SiO <sub>2</sub> films . . . . .	57
4.2	Attosecond transient absorption of SiO <sub>2</sub> in combination with attosecond streaking . . . . .	59
4.2.1	Attosecond streaking of broadband XUV pulses . . . . .	60
4.2.2	Transient absorption of nanometric SiO <sub>2</sub> films . . . . .	61
4.3	Theory of attosecond transient absorption in SiO <sub>2</sub> . . . . .	68
4.3.1	Modification of excitonic resonances in the absorption spectrum . .	68
4.3.2	Quantum-mechanical model of valence band and conduction band dynamics . . . . .	68
4.4	Reversible sub-cycle dynamics of dielectric polarizability . . . . .	70
<b>5</b>	<b>Nonlinear polarization spectroscopy of SiO<sub>2</sub></b>	<b>75</b>
5.1	Time-resolved optical reflectance . . . . .	76
5.1.1	Experimental setup . . . . .	76
5.1.2	NIR/VIS pump-probe study of reversible polarization . . . . .	77
5.2	Attosecond nonlinear polarization spectroscopy . . . . .	81
5.2.1	Experimental setup . . . . .	81
5.2.2	Sample requirements . . . . .	84

5.2.3	Time-resolved manifestation of self-steepening and Kerr effect . . .	84
<b>6</b>	<b>Conclusions and Outlook</b>	<b>91</b>
<b>A</b>		<b>93</b>
A.1	Wien2k modeling parameters . . . . .	94
A.2	SiO <sub>2</sub> samples . . . . .	95
A.2.1	Sub-micrometer thin SiO <sub>2</sub> samples for XUV transmission . . . . .	95
A.2.2	Sub-50 micrometer thin SiO <sub>2</sub> samples for NIR transmission . . . . .	96
A.3	Storage of raw data and analysis programs . . . . .	98
	<b>Bibliography</b>	<b>111</b>
	<b>Danksagung</b>	<b>113</b>
	<b>Curriculum Vitae</b>	<b>115</b>







# Zusammenfassung

Die Anregung von elektronischen Zuständen in Festkörpern durch den Einfluss von elektromagnetischen Wellen ist ein Prozess von grundlegender Wichtigkeit, sowohl in der wissenschaftlichen Untersuchung von Materialeigenschaften als auch in technologischen Anwendungen, die vor allem im Bereich der Halbleitertechnik nicht mehr aus unserem Alltag wegzudenken und allgegenwärtig sind. Die Zeitskala, auf der die Wechselwirkung stattfindet, wird zum einen durch die Pulsdauer der elektromagnetischen Strahlung und ihre Frequenz relativ zu den elektronischen Resonanz-Zuständen des untersuchten Systems und zum anderen durch die Bandbreite der Zustände bestimmt. Die Bandbreite von elektronischen Resonanzen in der Bandstruktur von Halbleitern und Dielektrika kann mehrere Elektronenvolt betragen. Im Bereich des sichtbaren Lichts sind daher Reaktionszeiten der elektronischen Zustände auf die einwirkende Strahlung innerhalb weniger Femtosekunden ( $1 \text{ fs} = 10^{-15} \text{ s}$ ) bis hin zu Attosekunden ( $1 \text{ as} = 10^{-18} \text{ s}$ ) möglich.

Die Entwicklung von ultrakurzen Laserpulsen im nah-infraroten bis sichtbaren Spektralbereich, die weniger als zwei volle Schwingungen bei der Trägerfrequenz enthalten, ermöglichte die Erzeugung von noch kürzeren, kohärenten Pulsen im extrem-ultravioletten Spektral-

bereich von sub-femtosekunden Dauer durch die nichtlineare Erzeugung höherer Harmonischer. Damit wurde der Grundstein für die Attosekundenphysik gelegt. Mit der Hilfe von neu entwickelten Mess-Konzepten wie zum Beispiel der Attosekunden-Streaking-Spektroskopie wurden erstmals die Schwingungszyklen des elektrischen Feldes eines nah-infraroten Lichtpulses selbst messbar. Diese Messverfahren mit isolierten Attosekundenpulsen ermöglichen heute die Einblicke in die Dynamik der Elektronenbewegung in Atomen und Molekülen auf einer Zeitskala von wenigen Femtosekunden. Auch erste Messungen zur Emissionzeit von Photoelektronen aus metallischen Festkörpern lieferten überraschende Resultate und trugen bereits zur Entwicklung neuer Theorien zur Photoemission bei.

Als Weiterentwicklung der klassischen Anrege-Abfrage-Spektroskopie, deren Zeitauflösung durch die Einhüllende der Laserpulse bestimmt ist, geben zeitaufgelöste Messungen auf der Zeitskala der Schwingung des sichtbaren Lichts Aufschluss darüber, wie elektronische Prozesse und Zustände durch das elektrische Feld des Lichts beeinflusst werden können. Im Rahmen der hier vorgestellten Dissertation wurden bestehende experimentelle Konzepte der zeitaufgelösten Femtosekunden- und Attosekunden-spektroskopie genutzt und konsequent weiterentwickelt, um neue Erkenntnisse zur Elektronendynamik

in Festkörpern mit grosser Bandlücke zu gewinnen. Die Dynamik von resonanten und nichtresonanten elektronischen Anregungsprozessen durch intensive ultrakurze Lichtpulse in Halbleitern und Dielektrika wurde auf der sub-femtosekunden Zeitskala experimentell untersucht.

Zum einen wurde die Auswirkung einer resonanten Anregung von elektronischen Zuständen über dem Leitungsbandminimum von Titan-Dioxid ( $\text{TiO}_2$ ) und deren Relaxationsdynamik auf die Schwingungszustände des Kristallgitters untersucht. Durch die resonante Anregung mit einem wenige Femtosekunden kurzen Ultraviolett-puls und die damit verbundene Änderung der Gitterpotentialfläche wird eine kohärente Gitterschwingung ausgelöst. Diese wird mit Hilfe von zeitaufgelösten Reflektivitäts-Messungen mit ultrakurzen Ultraviolett-pulsen durch die Verknüpfung der optischen Eigenschaften mit der Gitterstruktur messbar. Die experimentell bestimmte Phase dieser Schwingung relativ zum Anregungszeitpunkt liefert Hinweise auf eine stark korrelierte Abhängigkeit zwischen der Dynamik des elektronischen Systems und der Gitterpotentialfläche. Unterstützt durch eine Berechnung der Gitterpotentialfläche in Abhängigkeit des Anregungszustandes basierend auf der Dichte-Funktional-Theorie, wurde ein Modell entwickelt, das zeigt, dass nicht nur die Anregung selbst, sondern auch die Relaxationsdynamik der hochangeregten Zustände hin zum Leitungsbandminimum die Gitterstruktur wesentlich beeinflusst.

Der andere Schwerpunkt dieser Arbeit liegt in der Untersuchung der Veränderung von elektronischen Zuständen und der induzierten nichtlinearen Polarisation in Quarzglas ( $\text{SiO}_2$ ) durch intensive nah-infrarote Lichtpulse von wenigen Femtosekunden Dauer.

Experimentelle Erkenntnisse hierzu liefern zeitaufgelöste Untersuchungen an sub-Mikrometer dünnen  $\text{SiO}_2$ -Schichten mit breitbandigen sub-100-Attosekunden-Pulsen und ultrakurzen nah-infraroten Pulsen. Das Spektrum der Attosekunden-Pulse liegt im Bereich von Kernzustand-zu-Leitungsband-Übergängen in  $\text{SiO}_2$  und ermöglichen somit die Untersuchung dieser Zustände durch zeitaufgelöste Absorptionsmessungen. Diese wurden mit Attosekunden-Streaking-Messungen zur Lichtfeld-Charakterisierung kombiniert und erstmals simultan in einem Experiment durchgeführt. Im zeitlichen Überlapp der beiden Pulse und bei Feldstärken des nah-infraroten Pulses von  $\sim 2 \text{ V}/\text{\AA}$  weist die Absorption der Attosekundenpulse im Bereich der Kernzustand-zu-Leitungsband-Übergänge eine deutliche Abnahme der optischen Dichte auf, die periodisch mit dem Betrag des Lichtfeldes oszilliert. Gleichzeitig lässt sich eine Stark-Verschiebung der Zustände an der Leitungsbandunterkante zu kleineren Energien feststellen, die durch das optische Feld ausgelöst werden. Die Änderung der optischen Dichte tritt, wenn auch mit kleinerer Amplitude, über einen grösseren, mehrere eV breiten Bereich auf. Diese grosse Bandbreite der durch die Attosekundenpulse induzierten Polarisation erlaubt eine schnelle Dephasierung und damit einen Einblick in die Dynamik der Zustände in Echtzeit. Die Veränderung der optischen Dichte tritt nur während der Pulsdauer des nah-infraroten Lichtpulses auf und beginnt und endet abrupt in einem sub-Femtosekunden-Zeitfenster. Die Korrelation mit den gleichzeitig gemessenen Schwingungszyklen des elektrischen Feldes ermöglicht den direkten Vergleich mit quantenmechanischen Simulationen, die das experimentell gemessene Feld als Parameter nutzen. Die Simulation modelliert die Interaktion ohne zu Hilfe-nahme der Störungstheorie, also nicht-perturbativ. Eine wesentliche Übereinstimmung

von Experiment und Theorie unterstützt die Interpretation, dass die Eigenschaften von Dielektrika prinzipiell mit intensiven, ultrakurzen Lichtpulsen reversibel beeinflusst werden können.

Die Reversibilität der induzierten Polarisation wurde in einem weiteren Experiment an  $\text{SiO}_2$ -Oberflächen mit Hilfe einer zeitaufgelösten Reflektivitätsmessung untersucht. Die mit einem starken ultrakurzen nah-infraroten Anrege-Puls erhöhte Reflektivität einer  $\text{SiO}_2$ -Oberfläche wurde hierfür mit einem schwachen Puls gleicher Pulsdauer und Frequenz zeitaufgelöst gemessen. Die Erhöhung der Reflektivität zeigte eine nur schwache Asymmetrie im zeitlichen Überlapp beider Pulse und die Reflektivität kehrte auf der Zeitskala der Pulsdauer wieder zum Ausgangsniveau zurück. Dieses Ergebnis liefert einen zusätzlichen und modell-unabhängigen Nachweis der Reversibilität der induzierten Polarisation.

Um die Wechselwirkung zwischen dem elektrischen Feld des Lichts und der induzierten Polarisation zeitlich noch genauer aufzulösen, wurde das Konzept zur nichtlinearen Attosekunden-Polarisations-Spektroskopie entwickelt. Hierbei werden die Schwingungen des elektrischen Feldes eines ultrakurzen nah-infraroten Lichtpulses, das durch eine wenige Mikrometer dünne  $\text{SiO}_2$ -Probe transmittiert wird, mit der Attosekunden-Streaking-Technik charakterisiert. Das elektrische Feld des Lichts wird durch die nichtlineare Propagation durch das Dielektrikum in Abhängigkeit von der maximalen elektrischen Feldstärke beeinflusst. Der Vergleich der transmittierten Wellenformen mit einer Referenzwellenform bei niedriger Maximalfeldstärke liefert somit Erkenntnisse über die induzierte Polarisation in der Probe. In einem ersten Experiment konnte damit die nichtlineare Polarisation durch die nichtlineare Suszeptibilität dritter Ordnung, die zu einem intensitätsabhängigen Brechungsindex führt, erstmals auf der Zeitskala der Schwingung des elektrischen Lichtfeldes aufgelöst werden. Mit Hilfe der nichtlinearen Attosekunden-Polarisations-Spektroskopie sollen zukünftig auch nicht-perturbative Effekte, die bei Feldstärken im Bereich von  $1.5\text{-}2.5 \text{ V/\AA}$  auftreten, messbar werden.



# Abstract

In the framework of this thesis, established concepts of time-resolved femtosecond and attosecond spectroscopy of atoms and molecules have been employed and developed further with the aim of gaining new insight into the electron dynamics in semiconductors and dielectrics, in particular in titanium dioxide ( $\text{TiO}_2$ ) and silicon dioxide ( $\text{SiO}_2$ ). The investigation of electron dynamics *inside* bulk solids with femtosecond to sub-100-as light pulses expands the scope of attosecond metrology in the field of solid state physics.

Under resonant excitation with ultrashort UV pulses, a strong correlation has been found between the electronic relaxation of hot electrons in  $\text{TiO}_2$  and the structural response to the excitation in form of a coherent phonon. This finding contributes to a better understanding of the dynamics of carrier excitation and relaxation in semiconductors.

Under the influence of an intense few-cycle near-infrared pulse, the absorption probability of core-level states to conduction band states in  $\text{SiO}_2$  has been found to be modulated by the electric field of the light pulse. The effect occurred and vanished at a sub-femtosecond time-scale. This finding provides compelling evidence for the reversible modification of the properties of a dielectric material with the electric field of light at the femtosecond time scale. The implications of this finding in combination with the study of light-induced conductivity in a dielectric [1] involve the possibility of technological applications such as an ultrafast light-driven insulator-based transistor and the investigation of nonlinear polarization beyond the perturbative regime.

The nonlinear polarization in  $\text{SiO}_2$  induced by intense ultrashort near-infrared pulses has been tested in a time-resolved optical reflectance experiment that confirmed the reversibility of the induced changes in optical properties at the few-femtosecond timescale.

In order to resolve the effects of nonlinear polarization with sub-femtosecond time resolution, the new experimental concept of attosecond polarization spectroscopy has been developed. It allows resolving changes in near-infrared waveforms due to the nonlinear interaction with the induced polarization during propagation through a transparent material. As a proof of the method, the effects of the third-order nonlinearities present in  $\text{SiO}_2$  on a few-cycle near-infrared pulse have been observed with sub-cycle resolution.



# Introduction

The excitation of electronic states in solids through the interaction with electromagnetic waves is a process of great importance, in fundamental research on material properties as well as in technological applications, which are ubiquitous in our everyday life foremost in form of semiconductor-based information technology. The time scale of this interaction is determined on the one hand by the duration of the electromagnetic impulse and its frequency relative to the electronic resonances of the solid state system and on the other hand by the bandwidth of the involved electronic states. In semiconductors and dielectrics, the electronic bands of states formed by the periodic potential in the solid can be several electron volts wide. In the spectral range of visible light, this implies response times to the electric field of light at the few femtosecond ( $1 \text{ fs} = 10^{-15} \text{ s}$ ) to attosecond timescale ( $1 \text{ as} = 10^{-18} \text{ s}$ ).

The development of ultrashort laser pulses in the near-infrared and visible spectral range that contain less than two full cycles of the electromagnetic carrier wave has enabled the generation of even shorter, coherent light pulses in the extreme ultraviolet spectral domain via the process of high harmonic generation. This paved the way for the fast-growing field of attophysics, that explores electron dynamics at the sub-femtosecond time scale. With the development of new measurement concepts such as the attosecond streaking spectroscopy [2, 3], the wave cycles of the electric field of near-infrared light pulses could be resolved in time. Nowadays, measurements using isolated attosecond pulses provide insight into the dynamics of electronic motion in atoms [4, 5] and molecules at and below the few-femtosecond time-scale. Also the first attosecond measurements attempting to time-resolve the process of photoemission from metal surfaces [6, 7, 8] yielded surprising results that have triggered the development of new microscopic theories of photoemission.

## Motivation

It is highly desirable to extend the investigation of such sub-femtosecond electron dynamics also to processes unfolding *inside* of solids, where collective electron phenomena and electron-electron-interactions are of great importance due to the high density of the material and the band structure emerging from the interactions of many particles. While the electron dynamics in atoms and molecules in the gas phase and at surfaces with few-cycle



---

near-infrared pulses and isolated attosecond pulses are accessible via the detection of high harmonic emission of radiation [9, 10] and photoemission of electrons [11, 4, 12, 6, 7] as well as through the ionized atoms and molecular fragments, e.g. [13, 14], the observation of electron dynamics *inside* the bulk requires a different approach based on all-optical techniques [15], where the light field that is used to trigger and to probe the electron dynamics penetrates into the bulk and interacts with it. To advance the field of solid state attosecond metrology and to explore the electron dynamics in wide band gap materials in the presence of intense, ultrashort light pulses, existing tools of attosecond metrology have been combined with new measurement concepts and applied in the framework of this thesis.

## Outline of the thesis

Chapter 1 gives an overview on few-femtosecond laser pulse generation with controlled carrier-envelope phase and the harmonic generation of even shorter pulses in the ultraviolet and extreme ultraviolet domain. The important methods for characterization of femtosecond and attosecond light pulses are presented. In chapter 2, the current understanding of the interaction of light pulses with solids at the femtosecond and attosecond time scale that is relevant within the scope of this thesis is summarized based on the state-of-the-art of time-resolved measurements in wide band gap semiconductors and dielectrics. This includes the excitation and detection of coherent phonons and the description of nonlinear propagation of ultrashort light pulses in transparent materials.

After this introductory part, the experiments are presented in three individual parts, each having its own focus. The first part, presented in chapter 3, addresses the correlation between resonant electronic excitation of titanium dioxide ( $\text{TiO}_2$ ) with ultrashort ultraviolet pulses and the structural response following the excitation. The second part, chapter 4, describes the investigation of electron dynamics *inside* a transparent solid, fused silicon dioxide ( $\text{SiO}_2$ ) that are induced by an intense few-cycle near-infrared pulse. The unfolding changes in the electronic structure of the dielectric are probed with sub-100-as light pulses by attosecond transient absorption spectroscopy. Simultaneous attosecond streaking provides the exact timing to the incident electric field. The modification of the electronic structure is shown to be largely reversible at a few-femtosecond time scale. In the third part, chapter 5, the nonlinear polarization induced in  $\text{SiO}_2$  by a few-cycle near-infrared pulse is investigated in a time-resolved reflectance experiment and with the newly developed concept of attosecond polarization spectroscopy. This new method draws on the possibility to fully characterize the electric field waveform of a laser pulse with the attosecond streaking technique. Waveforms of pulses that have propagated through a nonlinear medium at different intensities are compared to a reference waveform. This allows to observe the effects of the induced nonlinear polarization in the medium on the waveform with sub-cycle resolution. In chapter 6, the last chapter, the findings of this work are summarized and put into perspective of further research.

---

## List of the author's publications directly related to the content of this thesis

- P1** M. Schultze, **E. M. Bothschafter**, A. Sommer, S. Holzner, W. Schweinberger, M. Fiess, M. Hofstetter, R. Kienberger, V. Apalkov, V. S. Yakovlev, M. I. Stockman and F. Krausz. *Controlling dielectrics with the electric field of light*. Nature, vol. **493**, no. 7430, pp. 75-78, 2013.
- P2** **E. M. Bothschafter**, A. Paarmann, E. S. Zijlstra, N. Karpowicz, M. E. Garcia, R. Kienberger and R. Ernstorfer. *Ultrafast Evolution of the Excited-State Potential Energy Surface of TiO<sub>2</sub> Single Crystals Induced by Carrier Cooling*. Physical Review Letters, vol. **110**, no. 6, 067402, 2013.
- P3** M. Schultze, **E. M. Bothschafter**, A. Sommer, S. Holzner, M. Fiess, M. Hofstetter, R. Kienberger, V. Apalkov, V.S. Yakovlev, M. I. Stockman and F. Krausz. *Strong-field-induced attosecond dynamics in SiO<sub>2</sub>*. EPJ Web of Conferences vol. **41**, 02014, 2013.
- P4** **E. M. Bothschafter**, A. Paarmann, N. Karpowicz, E. S. Zijlstra, M. E. Garcia, F. Krausz, R. Kienberger and R. Ernstorfer. *Interband excitation and carrier relaxation as displacive driving force for coherent phonons*. EPJ Web of Conferences, vol. **41**, 02021, 2013.

## Further publications of the author

- P5** **E. M. Bothschafter**, S. Neppl and R. Kienberger. *Few-Femtosecond and Attosecond Electron Dynamics at Surfaces*. Progress in Ultrafast Intense Laser Science IX, Springer Series in Chemical Physics, vol. **104**, pp. 183-211, 2013.
- P6** S. Neppl, R. Ernstorfer, **E. M. Bothschafter**, A.L. Cavallieri, D. Menzel, J.V. Barth, F. Krausz, R. Kienberger and P. Feulner. *Attosecond Time-Resolved Photoemission from Core and Valence States of Magnesium*, Physical Review Letters, vol. **109**(8), 087401, 2012.
- P7** W. Schweinberger, A. Sommer, **E. M. Bothschafter**, J. Li, F. Krausz, R. Kienberger and M. Schultze. *Waveform-controlled near-single-cycle milli-joule laser pulses generate sub-10 nm extreme ultraviolet continua*. Optics Letters, vol. **37**, no. 17, pp. 3573-3575, 2012.
- P8** S. Kahra, G. Leschhorn, M. Kowalewski, A. Schiffrin, **E. M. Bothschafter**, W. Fu, R. de Vivie-Riedle, R. Ernstorfer, F. Krausz, R. Kienberger and T. Schaetz. *A molecular conveyor belt by controlled delivery of single molecules into ultrashort laser pulses*. Nature Physics, vol. **8**, pp. 238-242, 2012.
- P9** E. Magerl, S. Neppl, A. L. Cavalieri, **E. M. Bothschafter**, M. Stanislawski, Th. Uphues, M. Hofstetter, U. Kleineberg, J. V. Barth, D. Menzel, F. Krausz, R. Ernstorfer, R. Kienberger and P. Feulner. *A flexible apparatus for attosecond photoelectron spectroscopy of solids and surfaces*. Review of Scientific Instruments, vol. **82**, no. 6, 063104, 2011.
- P10** **E. M. Bothschafter**, A. Schiffrin, V. S. Yakovlev, A. M. Azzeer, F. Krausz, R. Ernstorfer and R. Kienberger. *Collinear generation of ultrashort UV and XUV pulses*. Optics Express, vol. **18**, no. 9, pp. 9173-9180, 2010.

---

## List of oral presentations at international conferences

- C1** **E. M. Bothschafter**, A. Sommer, W. Schweinberger, M. Jobst, T. Latka, C. Jakubeit, A. Guggenmos, V. Yakovlev, R. Kienberger, M. Schultze and F. Krausz. *Sub-Cycle Strong-Field Induced Modification of the Optical Properties of SiO<sub>2</sub>*. Conference on Lasers and Electro-Optics (CLEO- QELS: Fundamental Science), QTh4D.1. San Jose, USA, 2013.
- C2** M. Schultze, **E. M. Bothschafter**, A. Sommer, S. Holzner, M. Fiess, M. Hofstetter, R. Kienberger, V. Apalkov, V. S. Yakovlev, M. I. Stockman and F. Krausz. *Strong field-induced attosecond dynamics in SiO<sub>2</sub>*. XVIII<sup>th</sup> International Conference on Ultrafast Phenomena, Lausanne, Switzerland, 2012.
- C3** S. Neppl, **E.M. Bothschafter**, R. Ernstorfer, A. L. Cavalieri, E. Magerl, M. Stanislawski, M. Hofstetter, W. Helml, M. Jobst, A. Kim, N. Karpowicz, J. V. Barth, F. Krausz, D. Menzel, R. Kienberger and P. Feulner. *Absolute Timescale in Attosecond Photoelectron Emission from Solids*. 3<sup>rd</sup> International Conference on Attosecond Physics (ATT03), Sapporo, Japan, 2011.
- C4** **E. M. Bothschafter**, A. Paarmann, N. Karpowicz, R. Kienberger, R. Ernstorfer and F. Krausz. *Coherent Lattice Vibrations in TiO<sub>2</sub>*. DPG Frühjahrstagung der Sektion Kondensierte Materie, HL 82.4, Dresden, Germany, 2011.
- C5** **E. M. Bothschafter**, A. Schiffrin, V. S. Yakovlev, F. Krausz, R. Ernstorfer and R. Kienberger. *Collinear Generation of ultrashort UV and XUV pulses for pump/probe spectroscopy*. DPG Frühjahrstagung der Sektion Kondensierte Materie, O 87.5, Regensburg, 2010.

# Chapter 1

## Fundamentals of ultrashort laser pulse generation and characterization

Since the first report on successful light amplification by stimulated emission of radiation (LASER) in a ruby crystal by Maiman [16], laser technology has been developing at an incredibly high pace and has resulted in a plethora of available lasers with different characteristics such as wavelength, bandwidth, repetition rate and pulse duration. In particular, the development of short-pulsed lasers has pushed the resolution of time-resolved measurements to the femtosecond domain. The broadband emission and amplification characteristics of titanium-doped sapphire crystals (Ti:Sapphire,  $\Delta\nu_{emission} \sim 660 \text{ nm}-1100 \text{ nm}$ ) have enabled the development of laser oscillators emitting octave-spanning spectra with pulse durations of down to 5 fs. In combination with Ti:Sapphire multipass amplification, this technology forms the basis of current femtosecond lasers with pulse durations below 100 fs.

The current limit of temporal resolution in the investigation - and to some extent even control - of electron dynamics in atoms, molecules and solids is dictated by the minimal duration of coherent light pulses that can be achieved. Therefore, the laser system and the technology to create and characterize coherent, isolated attosecond light pulses deserve special attention and are described in this chapter.

In the first section, the state-of-the-art laser technology for the generation of waveform controlled, ultrashort pulses in the near-infrared/visible (NIR/VIS) spectral domain used in the framework of this thesis is presented. Using these NIR/VIS few-femtosecond pulses, the up-conversion in a noble gas medium to femtosecond ultraviolet (UV) pulses via third-harmonic generation and the generation of isolated attosecond pulses in the extreme ultraviolet (XUV) via high harmonic generation become feasible. The details of these processes are described in sections 1.2 and 1.3, respectively. The complete characterization of such ultrashort pulses via two different techniques, frequency resolved optical gating and attosecond streaking, is described in section 1.4.

## 1.1 Waveform controlled few-cycle pulses in the near infrared

The generation of isolated attosecond pulses and their use in time-resolved experiments in combination with few-femtosecond NIR/VIS laser pulses requires a high degree of control over the NIR/VIS laser pulse parameters such as spectral width and spectral phase, pulse duration, long-term pulse energy stability and pulse-to-pulse peak intensity. This section introduces important definitions to describe ultrashort laser pulses and the relevant technical details of the laser system used for the experiments.

### 1.1.1 Mathematical description of laser pulses

Laser pulses are defined by the spatial and temporal or spectral characteristics of their electric field  $E(\mathbf{r}, t)$  or  $E(\mathbf{r}, \omega)$ , where  $\mathbf{r}$  denotes the spatial coordinate and  $t$  and  $\omega$  the temporal and spectral coordinates, respectively. The spectral and temporal domain are connected via the Fourier theorem and it is convenient and common to describe the real field quantities  $E(t)$  or  $E(\omega)$  by complex quantities defined as

$$\begin{aligned} E(\omega) &= |E(\omega)| \cdot e^{i\phi(\omega)} = \int_{-\infty}^{+\infty} E(t) e^{i\omega t} dt \\ E(t) &= |E(t)| \cdot e^{i\phi(t)} = \frac{1}{2\pi} \int_{-\infty}^{+\infty} E(\omega) e^{i\omega t} d\omega \end{aligned} \quad (1.1)$$

where  $|E(t)|$  and  $|E(\omega)|$  denote the real temporal and spectral amplitude and  $\phi(t)$  and  $\phi(\omega)$  the temporal and spectral phases, cf. for example the book of Boyd [17].

Due to the relation via the Fourier transform the minimal duration of a laser pulse  $\Delta t$  is closely connected to the maximum spectral width  $\Delta\omega$  by an uncertainty relation, often referred to as the time-bandwidth product:

$$\Delta t \cdot \Delta\omega \geq C \quad (1.2)$$

where  $C$  is a constant that depends on the pulse shape as well as the definition of pulse duration (temporal width  $\Delta t$ ) and spectral width ( $\Delta\omega$ ). For a Gaussian pulse, for example, defined as

$$E(t) = E_0 e^{-\frac{2\ln 2 t^2}{\tau_p}} \quad (1.3)$$

with  $\tau_p$  being the pulse duration defined at full-width at half-maximum of the temporal intensity the constant  $C$  is  $2\pi \cdot 0.441$  [18].

To describe the laser pulse in the time domain, a real field envelope  $\tilde{E}(t)$  and a carrier frequency  $\omega_0$  are defined as

$$E(t) = \tilde{E}(t) e^{i\Phi_{CEP}} e^{i\Phi(t)} e^{i\omega_0 t} \quad (1.4)$$

with the time-dependent phase  $\Phi(t)$  and the constant phase term  $\Phi_{CEP}$ . If  $\Phi(t)$  is expanded in a Taylor series

$$\Phi(t) = a_0 t + a_1 t^2 + a_2 t^3 + \dots \quad (1.5)$$

the first time-derivative of  $\Phi(t)$  lends itself to the interpretation as a time-dependent contribution to the carrier frequency, establishing an instantaneous frequency

$$\omega(t) = \omega_0 + \frac{d\Phi(t)}{dt} = \omega_0 + \Phi'(t). \quad (1.6)$$

The variation of instantaneous frequency with time is also called *chirp*. Depending on the non-zero contributions to the chirp  $a_n$ , the chirp is referred to as linear, quadratic, etc. for  $n=1, 2$ , etc. and as positive or negative with the respective sign of the chirp parameters  $a_n$ . To achieve the minimum pulse duration or Fourier limit for a given spectrum,  $\Phi'(t)$  needs to be constant.  $\Phi_{CEP}$  describes the relative phase of the electric field or waveform at the carrier frequency under the envelope and is therefore called the carrier-envelope phase (CEP). For long pulses this relative phase is of little importance, but for short pulses approaching the regime of a single wave-cycle under the envelope it becomes an important parameter that determines the peak intensity of the pulse as shown in Fig.1.1. For the investigation of field or intensity dependent effects with such short pulses, e.g. [3, 2, 19] it is therefore mandatory to be able to lock and control the CEP for an extended period of time.

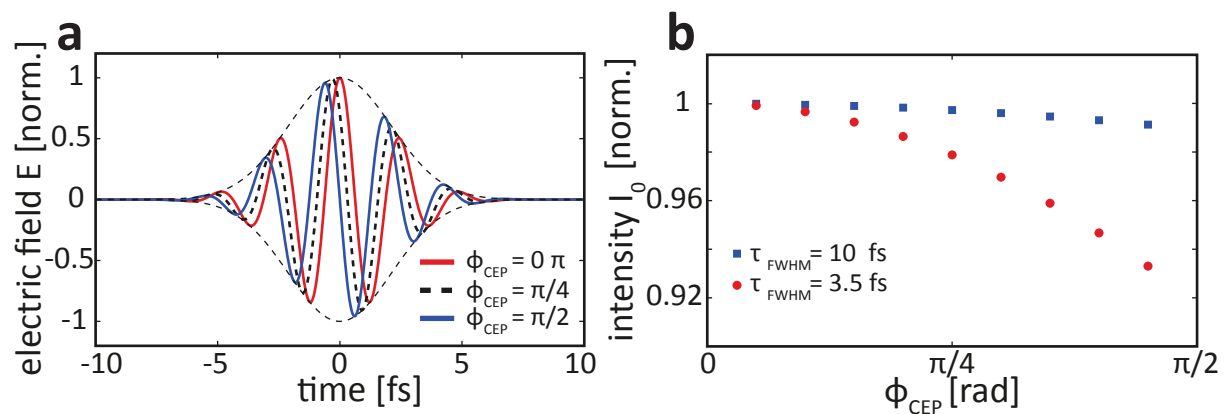


**Figure 1.1:** (a) Electric field of 1.5-cycle Gaussian pulses with a central wavelength of 750 nm with identical envelope but different CEP. (b) Relative peak intensity  $I_0$  in dependence of the CEP for pulses carried at 750 nm with identical envelope and energy for a pulse duration of 10 fs (blue) and 3.5 fs (red). When the pulse duration approaches a single cycle, the peak intensity is sensitive to the CEP.

### 1.1.2 The laser system

For the experiments presented in this thesis, two different Ti:Sapphire based femtosecond pulse laser sources have been used. A detailed description of the laser systems can be found in [20, 21]

and [22], respectively. Both laser systems have similar output pulse parameters and differ mainly in the technology used for temporal stretching and compression of the pulses in the chirped-pulse-amplification stage. Therefore an overview on one of them, the FP3 laser system [22] at the Max-Planck Institute of Quantum Optics, used with one amplification stage, shall be given here. The FP3 laser system is a modified version of a commercially available chirped-pulse-amplification laser source (Femtopower Compact Pro, Femtolasers Produktions GmbH) and consists of three main parts:

- A Kerr-lens mode-locked Ti:Sapphire laser oscillator, operating at 78 MHz repetition rate, emits pulses with a pulse duration below 7 fs (full width at half maximum, FWHM) and a pulse energy of 2-3 nJ. The spectral bandwidth extends from 700 nm to 1000 nm, enabled by a dispersive mirror design that compensates for intra-cavity dispersion. These pulses are focused on a periodically poled magnesium-oxide doped lithium-niobate (PP-MgO:LN) crystal for difference frequency generation (DFG) between the high and low ends of the spectrum. The spectrum of the fundamental pulse and the difference-frequency signal overlap spectrally. In this overlap region, a CEP dependent f-to-0 interference beat signal in the infrared occurs that can be detected with an IR photodiode and a spectrum analyzer. This beat signal is used as monitor signal in the fast-feedback CEP stabilization loop [23, 24], that will be described in more detail in section 1.1.3. The oscillator is pumped by a continuous wave (cw) pump laser with central wavelength at 532 nm (Verdi V6, Coherent Inc.) passing through an acousto-optical modulator (AOM), that permits to modulate the pump power.
- For chirped-pulse-amplification [25], the oscillator pulses are stretched in a 13.5 cm long SF57 glass block that introduces positive chirp to about 17 picoseconds (ps,  $1 \text{ ps} = 10^{-12} \text{ s}$ ) before they enter the first four passes through the Ti:Sapphire crystal of the multipass Ti:Sapphire amplifier stage at the full oscillator repetition rate. After the fourth pass, the repetition rate is reduced with a pulse picker (Pockels cell) to 4 kHz. At this stage, also the spectral amplitude is reduced in the center relative to the wings of the gain window with a programmable dispersive spectral shaper, a so called dazzler (Fastlite), to reduce gain narrowing and to optimize the amplification in the subsequent five passes. The Ti:Sapphire crystal is situated in a vacuum chamber equipped with Brewster entrance windows and is evaporation-cooled to 180 K to minimize thermal lensing effects. It is pumped by a frequency-doubled neodymium-doped ytterbium lithium fluoride (Nd:YLF) diode pumped laser at 527 nm (Photonics Industries, DM 30) with 30 W power at 4 kHz with nanosecond pulse width. After the ninth pass the NIR pulses have a pulse energy of 1.1 mJ. The positively chirped pulses are then re-compressed with a transmission grating compressor introducing negative dispersion. The amplified NIR pulses are compressed to  $\sim 23$  fs, which is close to the Fourier limit of their spectrum. Two position sensitive detectors (PSD1 and PSD2) monitor the beam path after the ninth pass and their signal is fed back to two piezo actuated mirrors to stabilize the beam path into a transmission grating compressor.
- The compressed pulses are then focused into a hollow core fused silica fiber with 250  $\mu\text{m}$  core diameter that resides inside a larger tube system filled with neon gas at an absolute pressure of 1.6 bar. The tube system can be evacuated prior to filling it with neon to



ensure high gas purity. Its entrance and exit windows are at Brewster's angle to minimize reflection losses. The NIR pulses form a stable filament inside of the hollow core fiber and the nonlinear interaction with the noble gas leads to spectral broadening due to self-phase modulation. The output spectrum covers the NIR and visible range from 450 nm to 1050 nm. The transmission through the fiber is  $\sim 50\text{-}60\%$ , so the pulse energy after spectral broadening is  $\sim 550\text{-}600 \mu\text{J}$ . Self-phase modulation leads to a positive chirp at the output of the hollow core fiber which results in an increased pulse duration. This chirp is subsequently compensated by eight reflections in a negatively chirped mirror compressor, where each reflection imprints a group delay dispersion (or linear chirp) of  $-35 \text{ fs}^2$  [26]. This tailored negative chirp allows to compress the pulses close to their Fourier limit of sub-4 fs and to precompensate the entrance window of the vacuum system that guides the beam to the experiment. The compression can be fine-tuned by relative movement of a pair of thin fused silica wedges that are set up in transmission under Brewster's angle resulting in an adjustable amount of glass the beam path. This changes the amount of positive dispersion imprinted on the pulse. The residual reflection of the first wedge's surface is used to generate the second harmonic of the octave-spanning output spectrum. The interference fringes resulting from the interference of the blue part of the fundamental radiation with the second harmonic of its red part are monitored with a spectrometer, forming the so-called f-to-2f interferometer that allows to detect slow CEP drifts occurring in the process of amplification, compression and spectral broadening, see section 1.1.3.

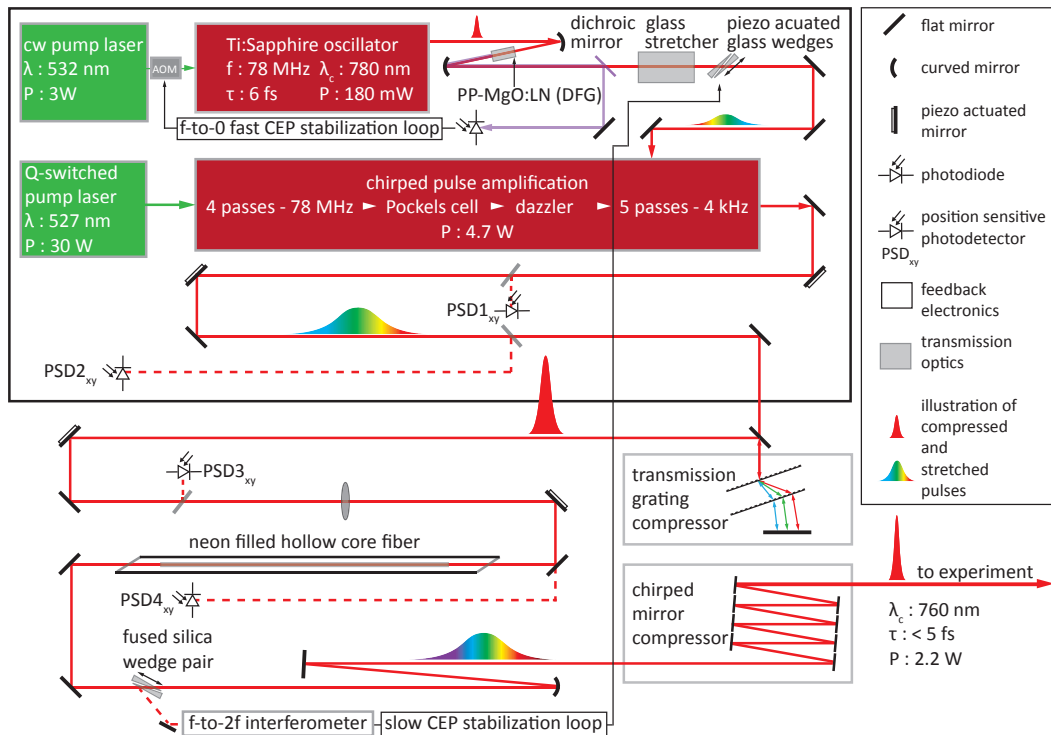


**Figure 1.2:** Layout of the FP3 laser system at the Max-Planck Institute of Quantum Optics.



### 1.1.3 Carrier-envelope phase stabilization

The output of a mode-locked laser oscillator cavity consists of a train of pulses when described in the time-domain. In the frequency domain, this corresponds to a so-called comb of equidistant frequency components [27] with a frequency separation corresponding to the repetition rate of the laser  $\nu_{rep}$ . The carrier-envelope phase  $\Phi_{CEP}$  difference of consecutive pulses is usually non-zero, even when the phase difference accumulated in one round-trip in the cavity,  $\Delta\Phi$ , equals multiples of  $2\pi$ , which can be achieved by proper intra-cavity dispersion control. Fluctuations of the pulse parameters can lead to nonlinear changes in the  $\Phi_{CEP}$  at each round trip and accumulate to a considerable phase jitter or drift of the  $\Phi_{CEP}$  [28] between individual pulses of the pulse train at the output. In the frequency domain, this leads to an offset of the comb lines relative to integer multiples of  $\nu_{rep}$ . This offset is called the carrier-envelope-offset frequency  $\nu_{CEO}$ . The measurement and stabilization of this  $\nu_{CEO}$  is therefore the key to a stable  $\Phi_{CEP}$  for all or a certain fraction of the output pulses [29].

#### CEP stabilization of the oscillator

The pulse train output of the broadband oscillator is focused in a periodically poled magnesium-

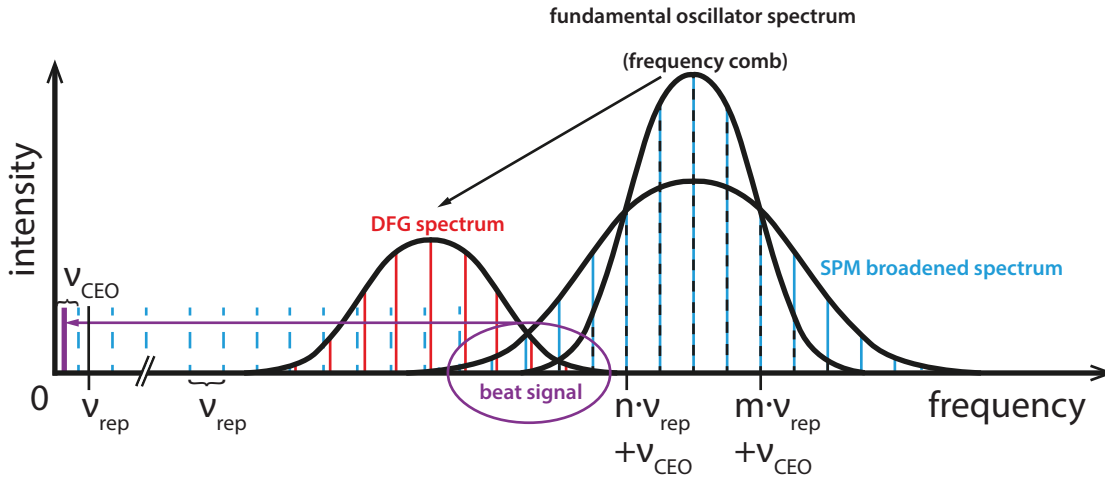


**Figure 1.3:** Illustration of the f-to-0 carrier-envelope-offset frequency  $\nu_{CEO}$  detection via the beating signal between the broadened spectrum of the fundamental oscillator output spectrum and the DFG signal generated from the fundamental spectrum in a PPLN crystal, adapted from [30].

oxide doped lithium-niobate (PP-MgO:LN) crystal chosen for optimal type-0 second harmonic generation (SHG) and difference frequency generation (DFG) [24] exhibiting a large nonlinearity, which also leads to additional spectral broadening due to self-phase modulation (SPM). The DFG process leads to comb lines in the infrared which are at integer multiples of the repetition rate  $\nu_{rep}$ , as

$$\nu_{DFG} = (m \cdot \nu_{rep} + \nu_{CEO}) - (n \cdot \nu_{rep} + \nu_{CEO}) = (m - n) \cdot \nu_{rep} \quad (1.7)$$

with  $m$  and  $n$  being integers describing the high and the low frequency part of the fundamental comb spectrum. In the region where the spectra of the fundamental comb (including the additional broadening due to SPM in the nonlinear crystal) and the DFG comb overlap, a heterodyne beat signal occurs at the frequency of the  $\nu_{CEO}$ , as illustrated in Fig.1.3. This signal is selected with a long-pass filter (cut-off at around 1400 nm) and detected with an infrared diode and a spectrum analyzer. A second diode detects the full repetition rate, which serves as the external radio-frequency oscillator to which the beat signal is then locked. In the current system, the intracavity dispersion is first adjusted such that  $\nu_{CEO} \sim 1/4 \cdot \nu_{rep}$  by means of an adjustable fused silica wedge pair inside of the cavity. The detected beat signal is then stabilized to exactly this value by an electronic feed-back loop that modulates the pump power in the oscillator with the AOM. This induces the appropriate Kerr-lens induced nonlinear phase shift in the cavity to minimize the error between signal and the reference. Stabilizing the  $\nu_{CEO}$  to one quarter of the repetition rate  $\nu_{rep}$  means that every fourth pulse in the pulse train from the oscillator exhibits the same CEP. This is sufficient as in the amplification stage the repetition rate is reduced to a fraction of the oscillator's repetition rate and the pulse picker is synchronized to pick the pulses with the same CEP.

### Correction of the CEP drift in the amplification stage

During the process of stretching, amplification, re-compression and spectral broadening of the amplified pulses in the hollow core fiber, power fluctuations of the pump laser and pointing instabilities causing a difference of beam paths in the grating compressor [30] can introduce nonlinear phase shifts which impair the longterm phase stability at the system's output. It is therefore necessary to compensate these comparably slow phase drifts and fluctuations in a second feedback loop to control the CEP at the output of the hollow core fiber. After broadening in the neon-filled fiber, the spectrum covers more than one octave. This allows for a different kind of CEO-phase detection, the so called f-to-2f-interferometer [31]. The residual reflection off the first wedge situated after the hollow core fiber (see Fig. 1.2) is focused in a thin beta-barium-borate (BBO) crystal for second harmonic generation. The spectral region where the second harmonic  $I_{SHG}$  of the red part of the fundamental spectrum  $I_F$  overlaps with the blue part of the fundamental spectrum is filtered with a bandpass and continuously recorded with a spectrometer. The relative intensity and polarization of both beams are adjusted with a half-wave-plate and a polarizer, with  $a$  being the polarizer transmission for the frequency doubled light. Due to the temporal walk-off  $\tau_0$  between the fundamental and the second harmonic in the crystal and their relative phase difference  $\Phi_{CEO}$ , interference fringes occur at the spectral overlap and the spectral intensity  $S(\omega)$  is modulated according to [31]:

$$S(\omega) = (1 - a) \cdot I_F(\omega) + a \cdot I_{SHG}(\omega) + 2 \cdot \sqrt{a(1 - a)} I_F(\omega) I_{SHG}(\omega) \cdot \cos(\Phi_{SHG} - \Phi_F + \omega\tau_0 + \Phi_{CEO}) \quad (1.8)$$

As the intensity instability at the output of the hollow core fiber is usually below 1%, the changes in spectral phase of the fundamental and the frequency doubled light,  $\Phi_F$  and  $\Phi_{SHG}$ , and  $\omega\tau_0$  are negligible. Therefore the phase of the cosine and with it the  $\Phi_{CEO}$  can be retrieved by a standard algorithm for Fourier-transform spectral interferometry [31, 32] and changes in

## 1.1 Waveform controlled few-cycle pulses in the near infrared

---

phase of subsequent pulses can be detected. This signal is then used in a feedback loop that controls the relative position of a wedge pair in the stretcher to compensate phase fluctuations. A CEP stability of typically less than 100 mrad root-mean-square error can be achieved with the combined fast and slow CEP stabilization [33].

## 1.2 Generation of few-femtosecond pulses in the ultraviolet

The broadening of NIR pulses in a noble-gas-filled hollow core fiber allows to produce more than one-octave-spanning spectra reaching from the far blue part of the visible at around 400 nm to the infrared spectrum well above 1000 nm, delivering sub-2-cycle pulses upon proper compression with broadband chirped mirrors. Recent highly sophisticated efforts of precise dispersion-controlled compression and well-timed superposition of different parts of this spectrum in a so-called wave-form-synthesizer [5, 34, 35] have produced the first light transients in the visible with sub-femtosecond duration. Few- or single-cycle pulses in the ultraviolet (UV) are desirable for excitation and observation of the evolution of electronic states at and above the valence states, that are important in the formation and breaking of bonds in molecules, e.g. [36], intramolecular charge migration, e.g. [14] and non-equilibrium electron dynamics in wide band gap semiconductors.

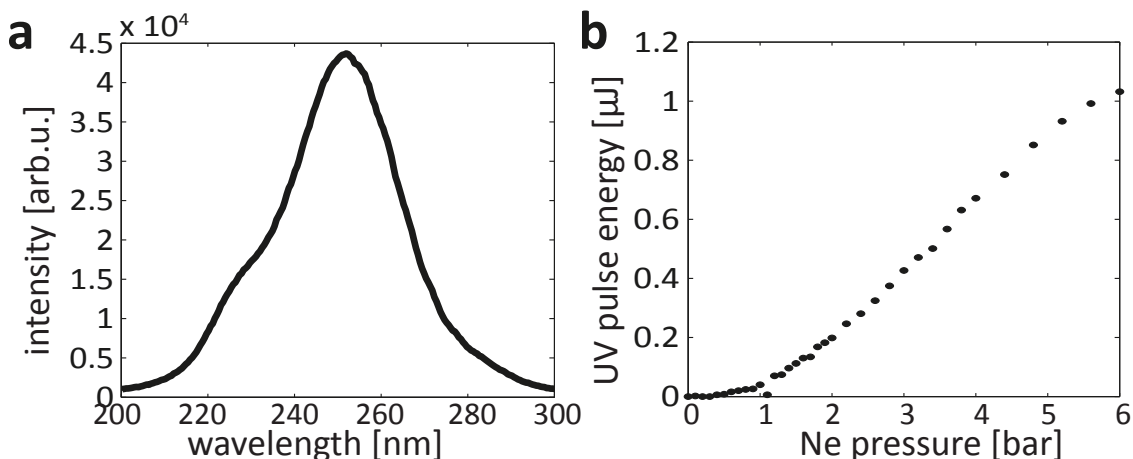


**Figure 1.4:** (a) Spectrum of the third harmonic of a sub-5-fs NIR/VIS laser pulse generated in a high pressure quasi-static gas cell [37]. (b) Resulting UV pulse energy in function of the neon gas pressure.

Using already broadband femtosecond NIR/VIS laser pulses as driving pulses in nonlinear frequency mixing or frequency up-conversion processes, ultrashort UV pulses can be generated in the nonlinear interaction with solids [38, 39, 40] and gases [41, 42, 43, 44, 45, 46, 47]. Efficient third harmonic generation from few-cycle NIR/VIS pulses in high pressure noble gases has been demonstrated by Graf et al. [46], yielding a pulse duration below 4 fs. This is possible due to the low dispersion of noble gases in the UV. This is also important for the phase matching, a negligible difference in group velocity of fundamental and the newly generated frequencies. Low ( $q^{th}$ ) order harmonic generation can be understood as a perturbative process, in which the bound electrons in a medium respond to the incident light field  $E$  as a function of the linear and nonlinear optical susceptibility  $\chi^q$  and the resulting polarization  $P$  is

$$P(t) = \epsilon_0 \cdot \sum_1^q \chi^q \cdot E(t)^q \quad (1.9)$$

with  $\epsilon_0$  being the vacuum permittivity and  $\chi^q$  being a tensor of rank  $q+1$ . In a centrosymmetric medium, e.g. an atomic gas, the even order contributions to the nonlinear susceptibility are zero for symmetry reasons. The efficiency of low order harmonic generation decreases with increasing order of the process, as it scales with the probability (or cross-section) of transforming  $q$  photons of the incident field into one higher energetic photon [48].

The nonlinear frequency conversion of few-cycle NIR/VIS pulses in high pressure noble gases poses some practical challenges. First of all, the setup should reside in an evacuated environment, as already propagation over a few tens of centimeters in air would cause a substantial lengthening of the pulse due to dispersion. This also prohibits the use of transmissive optics and windows for the gas cell. The latter would substantially limit the achievable UV pulse duration due to dispersion, therefore a high-pressure gas cell setup with a differential pumping concept has been developed in the course of the author's diploma thesis, which allows a pressure of several bar in the interaction region and a pressure of  $10^{-3}$  mbar region in only a few centimeter distance [49]. Fig. 1.4 **a** shows a third-harmonic spectrum from a sub-5-fs NIR/VIS driving laser pulse in a high pressure neon gas target in this setup and in panel **b** the tuning of the UV pulse energy with gas pressure.

## 1.3 Generation of isolated attosecond pulses with few-cycle laser pulses

While the generation of low-order harmonic radiation relies on the nonlinear polarization response of the bound electrons in the medium, higher order harmonic generation (HHG), which is the core process leading to pulses or pulse trains of sub-femtosecond duration in the extreme ultraviolet, cannot be understood within this perturbative description. Soon after the first observation of higher order harmonic radiation generated with high intensity laser pulses interacting with rare gases [50], it became clear that as the vector potential of the laser electric field approaches the atomic potential, the ionization of valence electrons and the interaction of the emerging electron wave packet with the ion plays an important role, bridging the gap between strong-field and plasma physics [51]. Although the processes involved carry important quantum-mechanical information on the interaction between light and matter [52], the main features can be understood in a very intuitive semi-classical description proposed by Corkum [53], the so-called three-step-model.

### 1.3.1 The three-step model of high harmonic generation

When a linearly polarized laser field with a maximum electric field strength  $E_L$  at the order of the atomic electric field strength  $E_{at}$  interacts with an atom, the potential barrier for the bound valence electrons is significantly reduced near the maxima of the laser electric field. This leads to tunnel ionization (step 1) from these states, releasing electron wave packets into the continuum [53] with a periodicity of twice the laser frequency. The electrons are subsequently accelerated by the laser electric field (step 2), away from the ionic core left behind. When the laser electric field reverses its direction in the following quarter wave cycle, the electron wave packet is accelerated back towards the ion, which can be considered to be at rest at the time-scale of the electron's excursion. With a small probability, the electron can then recombine (step 3) with the ion it originated from and release the ionization energy plus the excess energy it has gained during acceleration in the laser field in form of a high energetic photon. Depending on the moment of release within the wave cycle, the electron reaches the position of the ion either before or after the next zero-crossing of the laser field, as pictured in Fig. 1.5 **a** (following the illustration in [54, 55], which separates the *short* and *long* excursion trajectories, respectively). The photon energy emitted by electrons following the short trajectories increases with time spent in the continuum and therefore those trajectories result in a positive chirp of the emitted light bursts. The photon energy emitted by electrons following the long trajectories decreases with the return time, leading to a negative chirp of the emitted XUV pulses. The periodicity of ionization and recombination with every half-cycle of the laser pulse leads to a modulation in frequency with maxima at the odd order harmonics of the fundamental laser frequency, as can be seen in the left part of the spectrum shown in Fig. 1.5 **b**. The maximum achievable photon energy  $E_c$  at the so-called high energetic cut-off depends on the ionization potential of the gas  $I_p$  and the ponderomotive potential of the electron in the laser field  $U_p = e^2 \cdot E_L^2 / (4m_e \cdot \omega^2)$  with the central laser frequency  $\omega_0$ , the electron charge  $e$  and the electron mass  $m_e$ . A classical

treatment yields for the single atom response a cut-off energy of

$$E_c \sim I_p + 3.17U_p \text{ [53].} \quad (1.10)$$

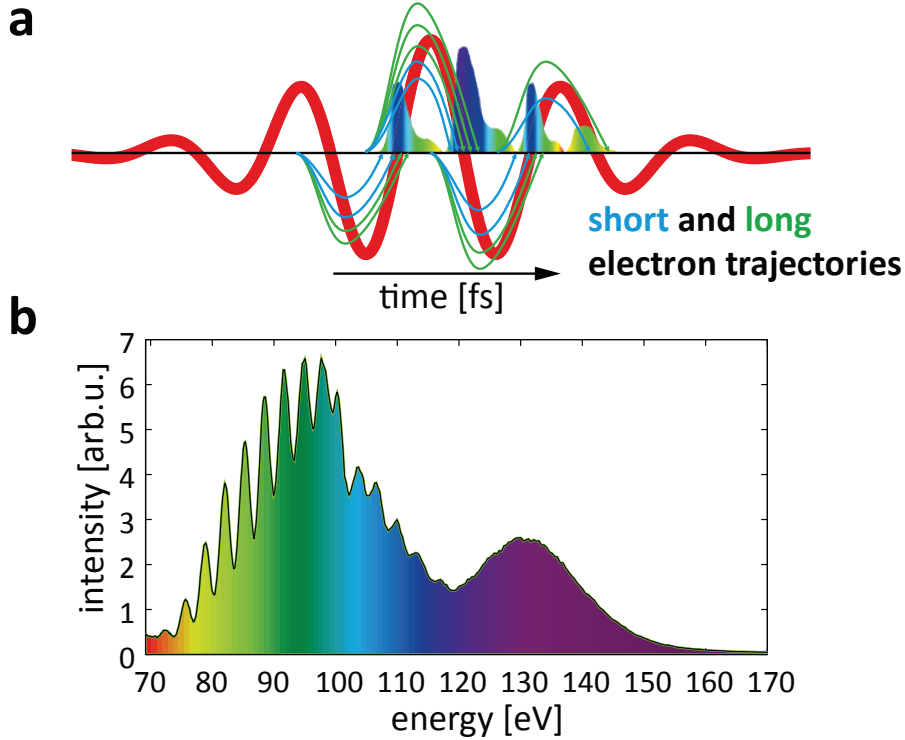


**Figure 1.5:** (a) Color-coded chirp of the harmonic emission for short and long trajectories of the electron in the continuum, adapted from [55]. (b) High harmonic spectrum generated with a  $\sim 450 \mu\text{J}$ , sub-4-fs laser pulse in neon at 300 mbar.

### 1.3.2 Isolated attosecond pulses

Linearly polarized pulses with several tens of femtoseconds duration produce a train of attosecond pulses spaced in time by half the oscillation period of the driving laser pulse, for all the half-cycles for which the three steps for high harmonic generation can be completed. In order to generate isolated attosecond pulses, the emission of high harmonic emission in a certain spectral range has to be restricted to a single half cycle. To this end, several techniques take advantage of the fact that HHG is restricted to a linearly polarized laser field [56], as circular or elliptical polarization prevents the recombination step for geometric reasons. A combination of two CEP-stabilized few-cycle laser pulses with opposite circular polarization and a well-defined relative time-delay at the order of the respective pulse-duration, creates a short time-gate of sub-cycle duration at the temporal overlap [57, 58, 59]. Isolated attosecond pulses with 130 as duration and a central energy of 36 eV could be achieved with this technique [19]. Ionization by the leading pulse sets a rather strict upper limit to the applicable pulse duration, which can be somewhat increased with the generalized double-optical gating approach (GDOG) [60, 61],

where two elliptically polarized fields are combined with a weak second harmonic field to construct an optical gate in time.

Another approach draws on the fact that above a critical ionization density, the phase-matching between the driving laser and the generated harmonics is lost. When the intensity of the driving laser is high enough to reach this critical density within a single cycle, it has been shown that isolated attosecond pulses with 430 as duration and tunable bandwidth can be achieved with this ionization gating technique [62].

For short pulses approaching a single-cycle oscillation, the relative strength of the different half cycles as well as the maximum electric field depends on the relative phase of the carrier wave under the envelope, see Fig. 1.1. When the CEP is close to the phase of a cosine waveform, where the maxima of the carrier wave and the envelope coincide, the highest energetic photons are emitted within a single half cycle of the laser field. This single event in time corresponds to an unmodulated spectrum in the cut-off region shown at the right Fig. 1.5 **b**. Spectral filtering of this high-energetic part of the spectrum yields isolated attosecond pulses which are inherently synchronized with the driving laser pulse. This approach yields pulse durations below 100 as [63, 64] at central energies at 90 eV and higher.



### 1.3.3 Setup for high harmonic generation in atomic gases

A sketch of the setup used for high harmonic generation by the few-cycle linearly polarized NIR/VIS laser pulses from the laser system described in chapter is shown in Fig. 1.6. The NIR/VIS laser pulses with a pulse energy of  $\sim 300\text{-}400 \mu\text{J}$  are focused with a concave silver mirror with 60 cm focal length on a metal tube (nickel or stainless steel), which serves as a quasi static gas cell (HHG gas target). The metal tube with 3 mm diameter and a wall thickness of 0.3 mm is closed at one side and supplied with high purity neon (purity grade 5.0) at  $\approx 250$  mbar from the other side. In propagation direction of the laser beam, the tube has two either laser-or mechanically drilled holes with 200-300  $\mu\text{m}$  diameter. During operation of this window-less quasi-static gas cell a background pressure of  $5 \cdot 10^{-3}$  mbar is maintained in the high harmonic chamber by two turbo-molecular pumps. The laser intensity can be adjusted for optimal HHG with a variable aperture (A). As the laser intensity at the focus (100  $\mu\text{m}$  full-width at half-maximum) of up to  $10^{14} \text{ W/cm}^2$  is sufficient to ablate material from the metal tube, the hole in the gas cell has to be aligned carefully to the beam. It can be moved in both transverse directions with picomotor driven piezo linear actuators (Newport) with sub-micrometer resolution. The position of the gas target over an extended range along the beam path can be adjusted with a linear step motor stage. This allows to optimize the target position within the confocal parameter in order to favor high harmonic generation from short trajectories [65], cf. Fig. 1.5 a. The high harmonic beam has a smaller divergence than the NIR/VIS beam [66], so both spatial and spectral separation of the two beams are possible.

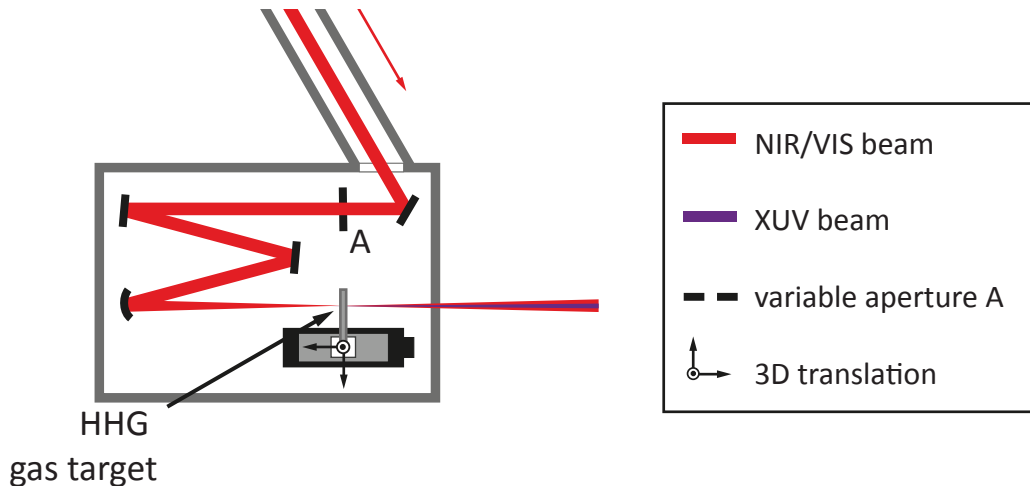


**Figure 1.6:** Sketch of the setup for high harmonic generation from atomic gases with few-cycle NIR pulses inside a vacuum chamber. The NIR/VIS beam, here shown in red, is focused onto a metal tube (HHG gas target) that is supplied with  $\approx 250$  mbar of an appropriate noble gas, e.g. argon, neon or helium. The gas target can be aligned transversely to the beam axis as well as along the focused beam to optimize the high harmonic generation process that is very sensitive to variations in intensity and CEP of the NIR/VIS pulse.

## 1.4 Femtosecond and attosecond pulse metrology

State-of-the art pulse characterization methods for ultrashort pulses build on the measurement of the spectral or temporal amplitude  $E(\omega)$  or  $E(t)$  and the respective phases  $\phi(\omega)$  or  $\phi(t)$  of a light pulse imprinted on a spectrally resolved nonlinear auto- or cross-correlation signal. In contrast to a simple intensity auto-correlation [67], it yields a complete description of the laser pulse either in time or frequency domain including the temporal or spectral phase by using an iterative reconstruction algorithm.

### 1.4.1 Frequency resolved optical gating of few-cycle NIR/VIS pulses

A widely applied method that is applicable for pulse durations down to a few femtoseconds is frequency resolved optical gating (FROG) [67]. The FROG signal is generated via a nonlinear process, e.g. second harmonic generation [68], self-diffraction or in transient grating geometry as a result of three-wave-mixing of two or three replica [69] of a single pulse. One of the replica is delayed with respect to the other(s) and serves as a time-gate for the nonlinear interaction. Taking spectra of the signal as a function of this time delay, the temporal amplitude and phase can be retrieved from the trace using an iterative algorithm to find the best agreement between a simulated spectrogram and the measured correlation trace. Fig. 1.7 shows a transient grating FROG trace and the retrieved pulse in time and frequency of the NIR/VIS pulse after the hollow core fiber and chirped mirror compressor of the laser system described in 1.1.

Such characterization tools rely on the availability of sufficient pulse energy and hence sufficient achievable intensity to induce a nonlinear interaction and the absence of absorption of the nonlinear material in the spectral range of the pulses to be characterized. In addition, due to dispersion in the nonlinear medium, phase matching limitations of the nonlinear interaction become substantial for pulses approaching a bandwidth of one octave.

### 1.4.2 XUV pulse characterization with the attosecond streak camera

In the XUV spectral range of high harmonics, complete pulse characterization via nonlinear processes is in many cases precluded due to the low pulse energy and a lack of appropriate, non-absorbing nonlinear media. Cross-correlation between XUV pulses and laser pulses via the ionization of atoms by the XUV pulse in the presence of an optical laser pulse present an alternative. The observation of the laser-induced side-bands in the photoelectron energy can be used for XUV pulse duration measurement, provided the XUV pulse duration is longer than the half-cycle of the laser field, e.g. [70]. Recently, two-photon-absorption induced Coulomb-explosion has been demonstrated as possible way for an autocorrelation of low-frequency (30 eV) attosecond pulses [71]. The relative phase between adjacent individual high harmonics forming a pulse train can be measured with two-photon two-color ionization [72, 54], as the intensity of the laser-induced sidebands is a function of the spectral amplitude and phase of the adjacent contributing harmonics. As such measurements do provide no or only limited spectral or

temporal phase information, complete characterization of few-cycle NIR/VIS pulse and isolated XUV attosecond pulses generated via HHG in noble gases requires a different approach, the attosecond streak camera.

The basic concept of a conventional streak camera is the idea of mapping the temporal structure of an electron pulse onto an extended screen in space by sweeping an electric potential perpendicular to the direction of propagation. Itatani et al. [73] proposed to apply a similar concept for the temporal characterization of sub-fs XUV pulses whose temporal structure can be transferred to an electron wave packet via ionization [19, 74] assuming that the ionized state carries no temporal phase information itself (which is true only in certain limits [75]) and that

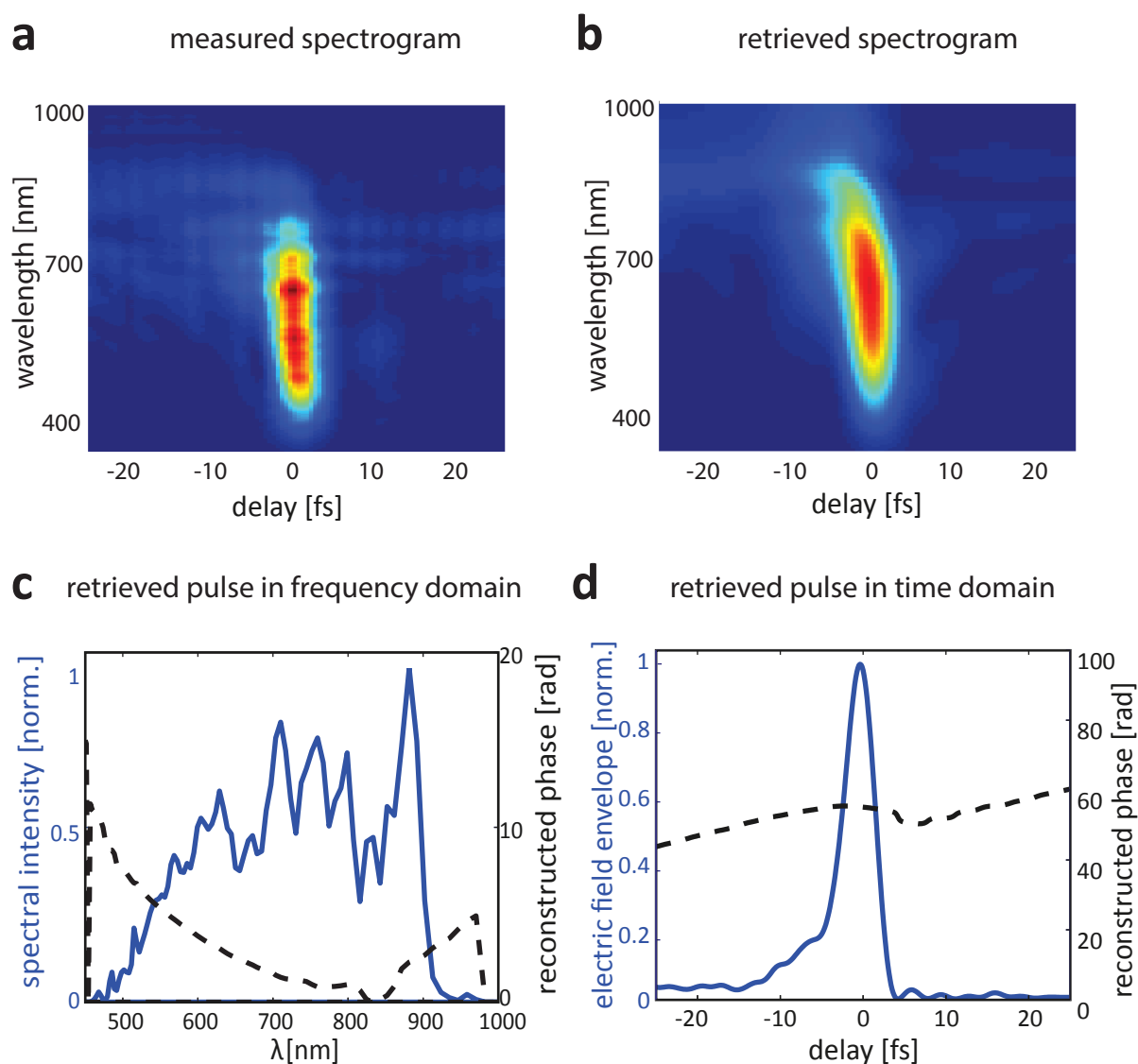


**Figure 1.7:** Measured (a) and retrieved (b) transient grating FROG trace of a 4.5 fs NIR/VIS pulse with the retrieved pulse electric field strength in spectral (c) and temporal (d) domain. Courtesy of A. Sommer.

the ionization cross section is constant over the spectral bandwidth of the XUV pulse. The sweeping electric potential is provided by the synchronized, linearly polarized NIR/VIS laser pulse. Instead of resolving the spatial variation of the electron trajectory, the final kinetic energy in the direction of polarization of the NIR/VIS field is resolved for a sequence of delay times between the XUV and the NIR/VIS pulse. The CEP and with it the temporal evolution of the NIR/VIS electric field relative to the attosecond pulse has to be locked during such a measurement. Such a spectrogram not only carries information on the duration of both pulses but also on their temporal phases. Kienberger et al. [76, 2] were the first to demonstrate this powerful technique for isolated attosecond pulse characterization experimentally and provided a comprehensive description of the concept, as detailed in the following.

An electronic wave packet that is created by direct ionization through an attosecond XUV pulse  $E_{XUV} = |E_{XUV}|e^{i\phi_{XUV}(t-\tau)} + c.c.$  with the central energy  $\hbar\omega_{XUV}$  and a spectral width  $\Delta\omega$  (*c.c.* being the complex conjugate) at an instant  $\tau$  shall be considered in the following. For simplicity, the initial momentum distribution of the electrons  $n_e(p_i, t)$  which is a consequence of the finite spectral width  $\Delta\omega$  of the XUV pulse is approximated by its central momentum  $p_c = \sqrt{\frac{\hbar\omega_{XUV} - I_p}{2m_e}}$ . In the presence of a linearly polarized NIR/VIS laser field  $E_{NIR} = |E_{NIR}|e^{i\phi_{NIR}t} + c.c.$ , the electron wave packet is accelerated and the resulting change in momentum at times  $t$  can be expressed as

$$\Delta p(t) = p_c(t) - p_c(\tau) = -e \int_{\tau}^t E_{NIR}(t') dt'. \quad (1.11)$$

Its final change in momentum, when  $t \rightarrow \infty$ , is then

$$\Delta p(\infty) = -e \int_{\tau}^{\infty} E_{NIR}(t') dt' = -e(A_{NIR}(\infty) - A_{NIR}(\tau)) = eA_{NIR}(\tau). \quad (1.12)$$

with  $A_{NIR}(t)$  being the vector potential of the laser electric field in the Coulomb gauge  $A_{NIR}(t) = \int_t^{\infty} E_{NIR}(t') dt'$  [2]. The final momentum distribution detected in direction of the laser polarization is then

$$\sigma(p_{\infty}, \tau) = \int_{-\infty}^{\infty} n_e(p(\tau) + eA_{NIR}(\tau), t) dt. \quad (1.13)$$

Fig. 1.8 shows a gas streaking spectrogram from the Ne  $2p$  level recorded with XUV pulses with 130 eV central energy and a bandwidth of 7.6 eV. The white line corresponds to the peak fit to the electron distribution at each delay step. The shift in electron momentum at each delay step is proportional to the current vector potential. The red line is the negative time-derivative of the vector potential  $A_{NIR}$ .

Provided that the XUV pulse duration and with it the duration of the electron wave packet is significantly shorter than the half-cycle oscillation of the laser field, a sequence of measurements of the momentum shift at delay times  $\tau_i$  allows direct measurement of the vector potential of the laser field [3]. From that the laser electric field can be easily derived. But such a streaking spectrogram carries far more information on the two pulses. It has been established that this NIR/XUV cross-correlation is very similar to a FROG measurement where the vector potential  $A_{NIR}(t - \tau)$  serves as the gate function [77, 78]. With the attosecond equivalent of a FROG

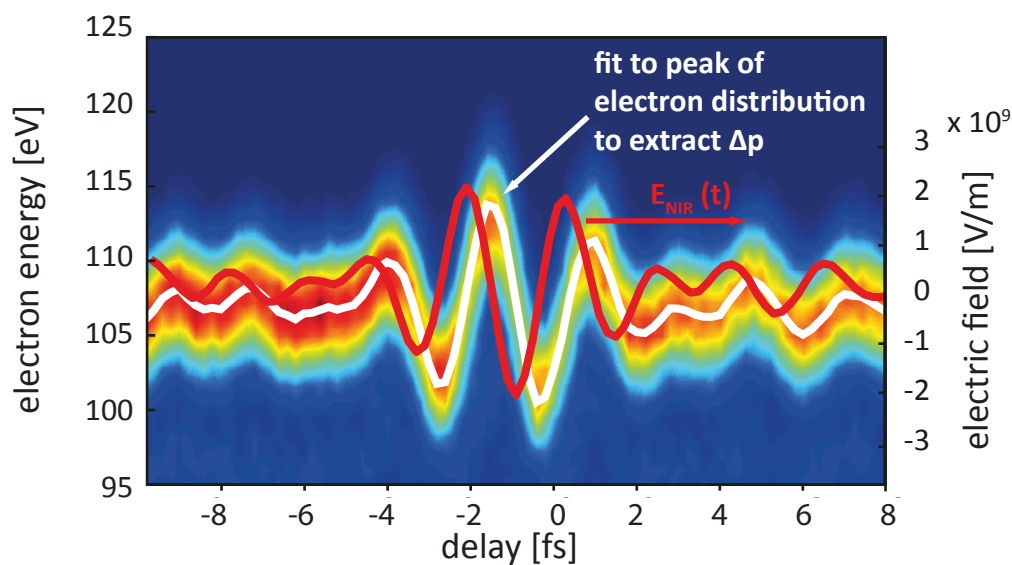


**Figure 1.8:** Streaking spectrogram recorded from the Ne 2p level (gas streaking). The peak of the electron distribution, depicted by the white line, is evaluated for each delay step. From this, the shift in electron momentum is extracted which is proportional to the vector potential  $A_{NIR}$ . The NIR/VIS electric field  $E_L(t)$ , shown as red line, is the negative time-derivative of  $A_{NIR}$ .

retrieval, referred to as FROG-CRAB (FROG-complete reconstruction of attosecond bursts), 130 as pulses have been characterized [19]. Gagnon et al. [74] developed a FROG retrieval algorithm for attosecond streaking spectrograms optimized for the characterization of attosecond XUV pulses. Fig. 1.9 shows the measured (a) and retrieved (b) spectrograms and the corresponding retrieved attosecond pulses and NIR pulses in the time domain (c and d, respectively) achieved with a HHG cut-off energy selection around 130 eV with a bandwidth of 7.6 eV.

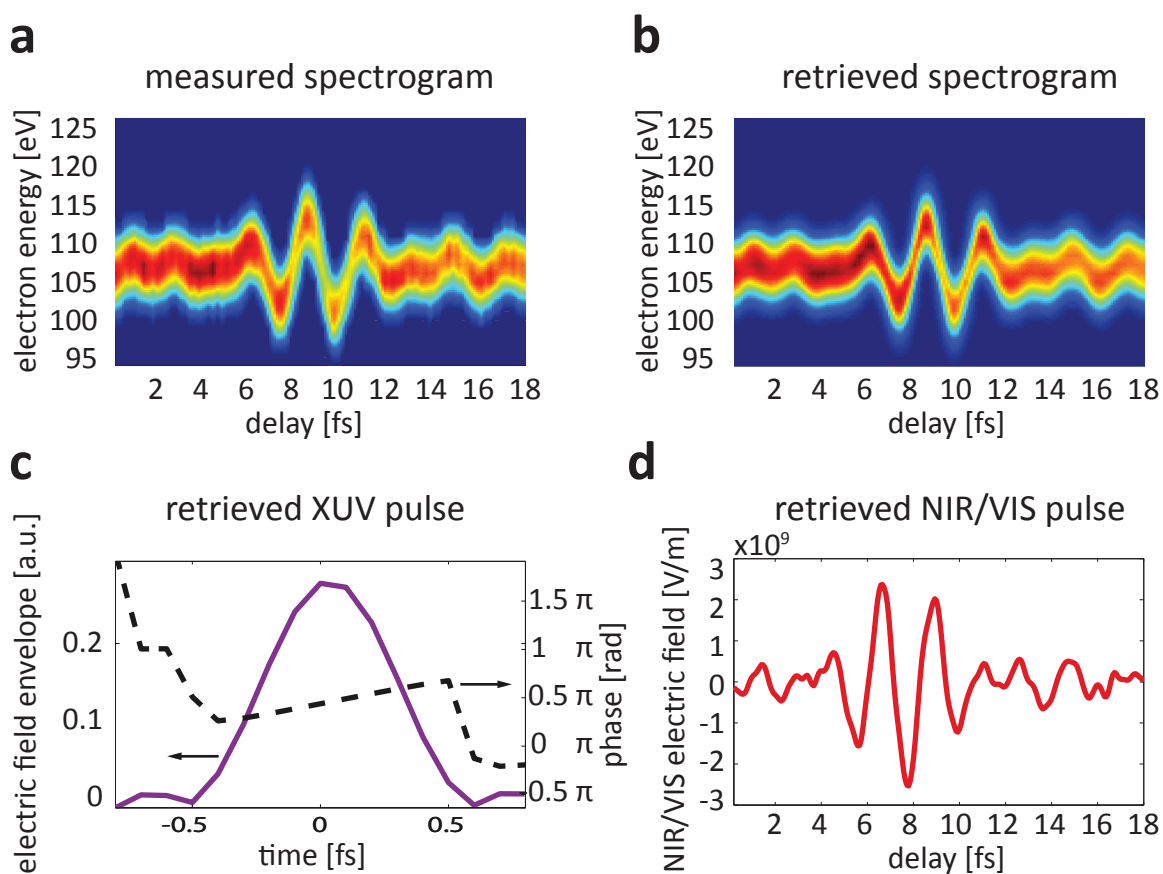


**Figure 1.9:** Measured (a) and retrieved (b) attosecond streaking spectrogram with the XUV FROG retrieval algorithm ATTOgram [74]. The retrieval algorithm allows to extract the the attosecond pulse field envelope and phase in time (c) domain and the NIR/VIS electric field (d).



## Chapter 2

# Light-matter interaction at the femtosecond and attosecond timescale

The fundamental interaction processes of light with condensed matter, and, more specifically for this thesis, with wide band gap semiconductors and dielectrics, depend on various parameters such as the laser wavelength relative to the allowed electronic transitions in the material and the intensity of the light field. At low intensities and light frequencies far from electronic resonances the electron cloud is dressed mainly proportionally to the electric field of light. Just like in a linear oscillator where the maximum displacement is proportional to the driving force, this polarization gives rise to the linear refractive index of the material. When the electric field of light starts to compete with the restoring force from the atom, the polarization needs to be corrected in higher orders of the electric field. In this perturbative regime the nonlinear response can be described as a sum of terms with increasing order in the electric field strength (Eq. 1.9). At an electric field strength that is comparable to the atomic field strength, this perturbative picture is no longer valid and the interaction has to be considered on a quantum-mechanical level.

This chapter summarizes the current understanding and concepts of the interaction of light pulses with solids at the femtosecond and attosecond time scale that are important within the scope of this thesis. The first section therefore deals with the basic idea of coherent phonon generation and detection in condensed matter with picosecond to femtosecond light pulses. In the second section, the wave equation for the propagation of light pulses in a nonlinear transparent medium is derived in a very general form, which serves as a starting point for the analysis of the experimental results in chapter 5.2.3.

The currently available femtosecond laser sources allow to expose materials to fields close to and beyond their damage threshold and to study for example the ionization dynamics in dielectrics under non-perturbative conditions. The last section of this chapter gives an overview on the state-of-the art of the experimental work in this emerging field of research on the few-to sub-femtosecond electron dynamics in dielectrics. With laser pulse durations down to the few-cycle regime in the VIS/NIR region and isolated attosecond pulses with durations below 100 attoseconds, the time-scale of electronic motion and polarization comes within experimental reach.



## 2.1 Coherent phonon generation and detection

The vibrational modes in crystal lattices or molecules, also called phonons, carry a wealth of information on the specific structure and symmetry of the material under investigation. Frequency-resolved optical techniques such as infrared absorption spectroscopy and Raman emission spectroscopy are invaluable tools to identify the optical phonon modes present in a specific crystal. Highly precise spectroscopic methods allow the determination of ground state structural dynamics, while time-resolved Raman spectroscopy using picosecond light pulses allows to study modes that have been excited by off-resonance light scattering [79]. As the observation of Stokes- or Anti-Stokes-shifted spectral components requires a laser spectral bandwidth below the optical phonon frequency which usually lies in the THz range, the temporal resolution of such measurements is limited to the picosecond time scale [80]. This spectral limitation also implies that the pulse duration of the laser pulse exciting the phonon motion is longer than the phonon oscillation period. As a consequence the excited phonons exhibit no clear phase relationship and are therefore *incoherent*, which precludes any phase sensitive detection.

The key to observe *coherent* lattice oscillations is to use excitation pulses with a pulse duration significantly shorter than the oscillation period of the phonon mode under investigation. Within the excited volume, the induced vibrations are then phase locked. This leads to a macroscopic ( $\mu\text{m}$ ), non-propagating lattice distortion in case of optical phonon modes. In contrast to measurements in the frequency domain or time-resolved spectroscopy of incoherently prepared phonon modes, the coherent phonon spectroscopy allows to determine the phonons' initial phase. In the following, the generation mechanisms of coherent optical phonons and possible ways of optical detection are outlined based on the review book chapters of Dekorsy, Cho and Kurz [80] and Ishioka and Misochko [81], which also give more details on recent experiments on coherent phonons in condensed matter. The theoretical considerations on coherence follow the quantum mechanical approach presented by Matsumoto and Watanabe [82].

Within the density matrix formalism, a quantum system of  $n$  eigenstates (e.g. the vibrational modes of a lattice) with energies  $\epsilon_n$  is characterized by its density matrix  $\rho$ , where the diagonal elements  $\rho_{nn}$  describe the population in the  $n$ th state and the off-diagonal elements  $\rho_{nm}$  with  $n \neq m$  describe the coherence between the  $n$ th and the  $m$ th state. Only if the two states are connected by a fixed phase relationship, the element  $\rho_{nm}$  is different from 0. With the Hamiltonian of the system  $H(t)$ , which describes the interaction of the quantum system with e.g. an electromagnetic field or a dynamic charge density, the time-evolution of the density operator can be written as

$$i\hbar \frac{\partial}{\partial t} \rho(t) = [H(t), \rho(t)] \quad (2.1)$$

Energy dissipation and dephasing can be added to the system's Hamiltonian via a phenomenological description in terms of dephasing rates  $\gamma_{nm}$  and population decay rates  $\Gamma$  according to [82] in the following form:

$$\frac{\partial \rho_{nn}}{\partial t} = \frac{-i}{\hbar} [H(t), \rho]_{nn} + \sum_{\epsilon_m > \epsilon_n} \Gamma_{nm} \rho_{mm} - \sum_{\epsilon_m < \epsilon_n} \Gamma_{mn} \rho_{nn} \quad (2.2)$$

$$\frac{\partial \rho_{nm}}{\partial t} = \frac{-i}{\hbar} [H(t), \rho]_{nm} - \gamma_{nm} \rho_{nm} \quad (2.3)$$

where the dephasing term  $\gamma_{nm}$  is a function of the total population decay rate from the state  $k$ ,  $\Gamma_k = \sum_{k^* (\epsilon_{k^*} < \epsilon_k)} \Gamma_{k^*k}$  and the pure dephasing rate  $\gamma_{nm}^*$ . A reduction of the off-diagonal elements is equivalent to dephasing, see Eq. 2.3. In order to relate this to the different excitation mechanisms and the amplitude of the coherent phonons, the Hamiltonian of the vibrational modes can be approximated by the Hamiltonian of a harmonic oscillator [83]. This leads to the equation of motion for the expectation value of the coherent displacement  $Q(t)$  [82]

$$\langle Q(t) \rangle Tr \{ Q \cdot \rho(t) \} = \sum_{nm} \rho_{nm} Q_{mn}, \quad (2.4)$$

which has been also found phenomenologically by assuming a harmonic oscillator of the coordinate  $Q$  with the reduced mass  $\mu$  driven by a force  $F(t)$  [84, 80, 85]

$$\mu \left[ \frac{\partial^2 Q(t)}{\partial t^2} + 2\beta \frac{\partial Q(t)}{\partial t} + \omega_0^2 Q(t) \right] = F(t), \quad (2.5)$$

where  $\beta$  describes phenomenologically the damping with a time constant  $\beta = 1/T$  resulting from pure and population-decay induced dephasing. In a pump-probe experiment using ultrashort laser pulses, the force  $F(t)$  arises from the interaction of the electromagnetic field with the solid. The formal solution to Eq. 2.5 is

$$Q(t) = \frac{1}{\omega^*} \int_{-\infty}^t dt' F(t') e^{-(t-t')/T} \sin \omega^*(t-t') \quad (2.6)$$

with  $\omega^* = \sqrt{\omega_0^2 - 1/T^2}$ . In order to create coherence in the system,  $F(t)$  has to act on a significantly shorter time scale than the oscillation period. While the initial phase of the lattice vibration is obscured by convolution with  $F(t)$  in a measurement involving a force, i.e. a light pulse, with a temporal profile longer than the phonon oscillation, it becomes an observable below that limit. The initial phase will then be determined by the temporal profile and the source of  $F(t)$ . The generation mechanisms can be classified in two main categories. On the one hand, stimulated non-resonant Raman-scattering processes [86] create a  $\delta$ -function-like or *impulsive* driving force (impulsive stimulated Raman scattering, ISRS). The pump pulse with the electric field  $E$  induces a force that is in lowest order proportional to the Raman polarizability  $\partial\alpha/\partial Q$ :

$$F_{ISRS} = \frac{1}{2} \left( \frac{\partial\alpha}{\partial Q} \right)_{kl} E_k E_l \quad (2.7)$$

This creates a coherent vibration in the ground state of the medium, as depicted in Fig. 2.7 **a**, with a sinusoidal initial phase ( $Q(0) \sim 0$ ) analogous to a harmonic oscillator that is pushed away from its equilibrium position Fig. 2.7 **b**.

On the other hand, in the case the laser frequency is resonant with an interband transition, there are real transitions of carriers into the excited state via first-order absorption of photons. This

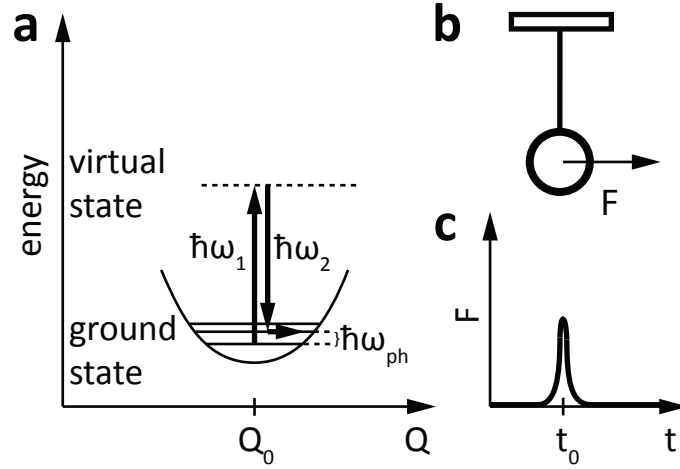


**Figure 2.1:** Non-resonant ISRS (a) induces a  $\delta$ -function-like driving force (c) leading to a sinusoidal oscillation in the ground state, acting just like a "kick" on a harmonic oscillator in its equilibrium position (b) (adapted from [81]).

abrupt change in charge density in real space is equivalent to a sudden shift of the equilibrium position of the lattice. This *displacive* excitation mechanism (displacive excitation of coherent phonons, DECP) induces a cosine-like oscillation ( $Q(0) = Q_{max}$ ) around the new minimum of the potential energy surface (PES), shown in Fig. 2.2.

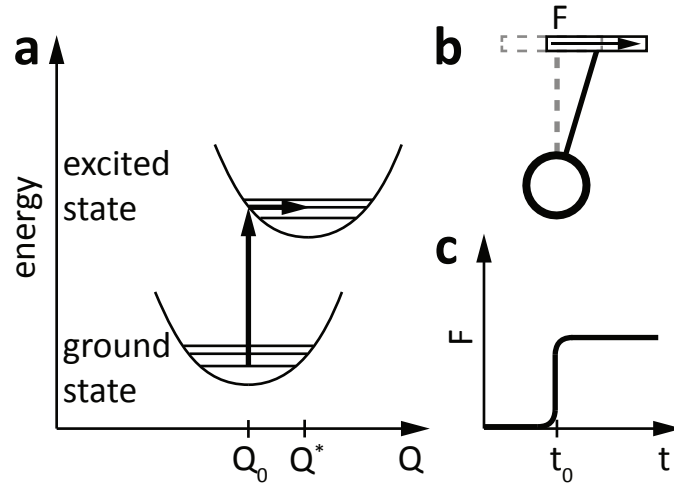


**Figure 2.2:** Resonant excitation (a) corresponds to applying a step-like driving force ((c) leading to a cosine oscillation in the excited state, analogous to a sudden shift of the equilibrium position of a harmonic oscillator (b) (adapted from [81]).

The two models, ISRS and DECP, have recently been combined by Riffe et al.[85] based on previous work by Merlin [86], introducing an extended, but finite life time of excited electronic states populated via resonant ISRS.

While coherent phonon oscillations can be detected via a range of methods like time-resolved x-ray diffraction, e.g. [87], x-ray absorption spectroscopy, e.g.[88], or Terahertz emission spectroscopy, nonlinear optical detection still offers the highest time-resolution combined with usually

high sensitivity. The macroscopically coherent lattice oscillation  $Q(t)$  created within the pump pulse excitation volume leads to a periodic modulation of the optical properties defined by the electron-lattice configuration. This can be detected, for example, as a periodic modulation of the electric susceptibility  $\chi$  projected on the reflectivity  $R$  of the medium [81]:

$$\Delta R(t) = \frac{\partial R}{\partial \chi} \frac{\partial \chi}{\partial Q} Q(t) \quad (2.8)$$

$\Delta R(t)$  is proportional to the amplitude of the lattice oscillation for probe pulse durations significantly shorter than the coherent phonon period. This leads to a modulation of the reflected signal at the phonon frequency and enables the optical detection of coherent lattice motion.

## 2.2 Nonlinear ultrashort pulse propagation in transparent media

An intense, ultrashort laser pulse propagating through a transparent, dispersive and isotropic nonlinear medium such as fused silica gives rise to linear and nonlinear polarization in the material. The bound electrons in the medium respond to the optical field and, far from electronic resonances that would lead to absorption, the response is at the sub-femtosecond timescale and mainly proportional to the incident field. As mentioned before, at high field strengths ( $\geq 10^{12}$  W/cm<sup>2</sup>) the nonlinear contributions to the induced polarization become appreciable and can lead to the generation of new frequency components and to an intensity dependent change in refractive index of the material. The nonlinear propagation is described by the nonlinear wave equation which can be deduced from Maxwell's equations:

$$\begin{aligned}\nabla \cdot D &= \rho \\ \nabla \cdot B &= 0 \\ \nabla \times E &= -\frac{\partial B}{\partial t} \\ \nabla \times H &= -\frac{\partial D}{\partial t} + J\end{aligned}\tag{2.9}$$

In the dielectric, we assume that there are no free charges,  $\rho=0$ , and no free currents,  $J = 0$ , and that the material is non-magnetic, so

$$B = \mu_0 H.\tag{2.10}$$

The wave equation is derived by substituting  $\nabla \times B$  by  $\mu_0 \cdot \frac{\partial D}{\partial t}$  and  $\mu_0$  by  $(\epsilon_0 c^2)^{-1}$  in

$$\begin{aligned}\nabla \times \nabla \times E &= -\nabla \times \frac{\partial B}{\partial t} \\ \nabla \times \nabla \times E &= -\frac{1}{\epsilon_0 c^2} \frac{\partial^2 D}{\partial t^2}\end{aligned}\tag{2.11}$$

### 2.2.1 The nonlinear wave equation

The polarization response of the material described by the electric displacement  $D$  can be separated in a linear part  $D^{(1)}$  and a nonlinear polarization  $P^{NL}$ :

$$D(r, \omega) = D^{(1)}(r, \omega) + P^{NL}(r, \omega) = \epsilon_0 \epsilon_r(\omega) E(r, \omega) + P^{NL}(r, \omega)\tag{2.12}$$

with  $D^{(1)}(r, \omega) = \epsilon_0 \epsilon_r^{(1)}(\omega) E(r, \omega)$ , where  $\epsilon_r^{(1)}(\omega)$  is the linear relative permittivity of the isotropic material. Following the derivation presented in Ref. [17], the field quantities are represented in

terms of their Fourier transforms:

$$\begin{aligned}
 E(r, t) &= \frac{1}{2\pi} \int E(r, \omega) e^{-i\omega t} d\omega \\
 D^{(1)}(r, t) &= \frac{1}{2\pi} \int D^{(1)}(r, \omega) e^{-i\omega t} d\omega \\
 P^{NL}(r, t) &= \frac{1}{2\pi} \int P^{NL}(r, \omega) e^{-i\omega t} d\omega
 \end{aligned} \tag{2.13}$$

The nonlinear wave equation in its most general form is then

$$\nabla \times \nabla \times E + \frac{1}{c^2} \frac{\partial^2}{\partial t^2} E = -\frac{1}{\epsilon_0 c^2} \frac{\partial^2 P^{NL}}{\partial t^2}. \tag{2.14}$$

Using the identity

$$\nabla \times \nabla \times E = \nabla(\nabla \cdot E) - \nabla^2 E \tag{2.15}$$

and neglecting the first term on the right hand side leads to the wave equation in the following form:

$$-\nabla^2 E + \frac{1}{c^2} \frac{\partial^2 D^{(1)}}{\partial t^2} = -\frac{1}{\epsilon_0 c^2} \frac{\partial^2 P^{NL}}{\partial t^2} \tag{2.16}$$

Similar to Eq. 1.4, the electric field  $E(r, t)$  can be described by a (complex) slowly varying field amplitude  $A(r, t)$  at an angular carrier frequency  $\omega_0$  and the wave vector  $k_0 = n_0 \omega_0 / c$  with the linear refractive index  $n_0$ :

$$\begin{aligned}
 E(r, t) &= A(r, t) e^{i(k_0 z - \omega_0 t) + i\Phi} + c.c. \\
 E(r, \omega) &= A(r, \omega - \omega_0) e^{ik_0 z + i\Phi} + c.c.
 \end{aligned} \tag{2.17}$$

It is important to notice that for pulses approaching the single cycle regime, the envelope has to be defined carefully [89] and is only valid if a change of  $\Phi$  does not alter the envelope and thus does also not change the carrier frequency  $\omega_0$ . Brabec and Krausz [89] have shown the validity of this concept for pulses containing at least one carrier wave cycle and derived a first-order equation for nonlinear propagation in the time domain.

With the ansatz in Eq. 2.17 and neglecting higher order dispersion from the term  $k = \sqrt{\epsilon} \omega / c = k_0 + ik_1 \partial_t + \mathcal{O}(k)$ , the wave equation in the time domain can be expressed as

$$\left[ \nabla_{\perp}^2 + \frac{\partial^2}{\partial z^2} + 2ik_0 \left( \frac{\partial}{\partial z} + k_1 \frac{\partial}{\partial t} \right) - k_1^2 \frac{\partial^2}{\partial t^2} \right] A(r, t) = \frac{1}{\epsilon_0 c^2} \frac{\partial^2 P^{NL}}{\partial t^2} \tag{2.18}$$

It is convenient to consider the propagation of the wavepacket in a moving frame of reference that moves with its group velocity  $v_g = k_1^{-1}$  with the coordinate transformation  $z = z'$  and  $\tau = t - k_1 z$ :

$$\left[ \nabla_{\perp}^2 + \frac{\partial^2}{\partial z'^2} - 2k_1 \frac{\partial}{\partial z'} \frac{\partial}{\partial \tau} + k_1^2 \frac{\partial^2}{\partial \tau^2} + 2ik_0 \frac{\partial}{\partial z'} - k_1^2 \frac{\partial^2}{\partial \tau^2} \right] A(r, t) = \frac{1}{\epsilon_0 c^2} \frac{\partial^2 P^{NL}}{\partial \tau^2} \tag{2.19}$$

## 2.2 Nonlinear ultrashort pulse propagation in transparent media

---

For simplicity, we neglect the diffraction term  $\nabla_{\perp}^2 A$  and consider only the one-dimensional propagation in the  $z$ -direction  $A(z, t)$ :

$$\left[ \frac{\partial^2}{\partial z'^2} - 2k_1 \frac{\partial}{\partial z'} \frac{\partial}{\partial \tau} + 2ik_0 \frac{\partial}{\partial z'} \right] A(z, t) = \frac{1}{\epsilon_0 c^2} \frac{\partial^2 P^{NL}}{\partial \tau^2} \quad (2.20)$$

Similar to the electric field, the nonlinear polarization can be expressed in terms of a slowly varying amplitude  $p(z, t)$ :

$$\begin{aligned} P^{NL}(z, t) &= p(z, t)e^{i(k_0 z - \omega_0 t)} + c.c. \\ \frac{\partial^2 P^{NL}}{\partial \tau^2}(z, t) &= -\omega_0^2 \left( 1 + \frac{i}{\omega_0} \frac{\partial}{\partial \tau} \right)^2 p(z, t)e^{i(k_0 z - \omega_0 t)} + c.c. \end{aligned} \quad (2.21)$$

$$\left[ \frac{\partial^2}{\partial z'^2} + 2ik_0 \frac{\partial}{\partial z'} \left( 1 + i \frac{k_1}{k_0} \frac{\partial}{\partial \tau} \right) \right] A(z, t) = -\frac{\omega_0^2}{\epsilon_0 c^2} \left( 1 + \frac{i}{\omega_0} \frac{\partial}{\partial \tau} \right)^2 p(z, t) \quad (2.22)$$

Following [17], we can approximate the term  $\frac{k_1}{k_0}$  as

$$\frac{k_1}{k_0} = \frac{1}{v_g} \frac{c}{n\omega_0} = \frac{n_g}{n\omega_0} \approx \frac{1}{\omega_0} \quad (2.23)$$

when dispersion is neglected. In the frame of the slowly varying amplitude approximation (see Brabec and Krausz [89]) the term  $\partial_z^2$  is neglected and we obtain the so-called generalized nonlinear Schrödinger equation for wave propagation that will be used to interpret the experimental results in chapter 5:

$$\begin{aligned} 2ik_0 \frac{\partial A}{\partial z'} &= -\frac{\omega_0^2}{\epsilon_0 c^2} \left[ 1 + \frac{i}{\omega_0} \frac{\partial}{\partial \tau} \right] p(z, t) \\ \frac{\partial A}{\partial z'} &= \frac{i\omega_0}{2\epsilon_0 c n_0} \left[ 1 + \frac{i}{\omega_0} \frac{\partial}{\partial \tau} \right] p(z, t) \end{aligned} \quad (2.24)$$

In the perturbative regime far from resonances, Eq. 2.24 allows to describe nonlinear polarization as a power series in function of the applied field  $P(t) = \epsilon_0 \cdot \Sigma_q \chi^q \cdot E(t)^q$  (Eq. 1.9), assuming convergence of this series to the nonlinear effect. At high field strengths, when the electric field becomes comparable or larger than the binding potential of the atom or lattice, this assumption is no longer valid. For dielectrics with a valence-to conduction band energy gap of  $\Delta E_g$ , this critical field strength is defined as the the field under which the electron potential energy changes by  $\Delta E_g$  over the distance of the lattice period  $a$ :

$$F_{crit} = \frac{\Delta E_g}{|e|a} \quad (2.25)$$

In this strong-field regime, the nonlinear interaction needs to be described quantum-mechanically. Especially for solids this is an active area of research [90, 91] and more details will be given in chapter 4.3.2.

## 2.3 Strong-field induced electron dynamics in dielectric solids

Attosecond science emerged from the study of the non-perturbative interaction of intense laser fields with atoms in the gas phase [56]. Few-cycle NIR/VIS laser pulses with controlled CEP and their cross-correlation with attosecond pulse trains and isolated attosecond pulses allow to explore the fundamental process of ionization on the sub-femtosecond time-scale [13, 11, 4] in atomic and molecular gases. The single and multi-electron dynamics induced by the interaction with the strong optical field [31, 13, 14] and attosecond pulses in combination with few-cycle NIR/VIS laser pulses have been used for the time-resolved study of relative and even absolute ionization times in atoms [4, 11]. It is highly desirable to extend the investigation of such sub-femtosecond electron dynamics also to solids, where collective electron phenomena and electron-electron-interactions are of great importance due to the high density of the material and the band structure emerging from these interactions. Recently, the relative ionization times of electrons originating from core-level and conduction band states from a metal surface [6, 7] could be measured using the attosecond streaking technique (see chapter 1.4.2).

In order to investigate the behavior of solids in the presence of strong electric fields in the non-perturbative regime, the photon energy of the laser pulse has to be far away from electronic resonances to exclude single and two-photon absorption. Ideally also there are no free carriers in the material before the interaction, preventing strong screening of the incident field. For the few-cycle NIR/VIS laser pulses, fused silica ( $\text{SiO}_2$  or  $\alpha$ -Quartz) is therefore an ideally suited material, as its band gap of  $\sim 9$  eV [92] exceeds the central photon energy of  $\sim 1.6$  eV by more than a factor of five.

In the following, an overview on the electron dynamics of  $\text{SiO}_2$  and other dielectrics in the presence of strong laser fields up to the dielectric breakdown threshold shall be given to put the present work in perspective of recent experimental work in the field.

### 2.3.1 Femtosecond dielectric breakdown in $\text{SiO}_2$

In dielectrics, electric breakdown occurs when an excess number of electrons is excited from the valence band into the conduction band. The material's properties such as absorptivity, refractive index, chemical properties and electrical conductivity change drastically close to and upon breakdown. Dielectric breakdown can be achieved by high static voltages but also by short pulsed laser fields. A permanent modification of the refractive index by laser pulses focused into transparent media allows for example to write three-dimensional waveguides with micrometer precision. The static breakdown voltage [93] is usually much lower than the electric fields that lead to optical breakdown with pulsed laser fields, investigated e.g. in [94, 95, 96, 97, 98, 99, 100], and the shorter the pulse duration, the higher is this breakdown voltage threshold. This is due to the different competing mechanisms that can lead to the excitation of carriers at different timescales. There has been quite some theoretical interest in describing the breakdown mechanisms [101, 102, 103, 104, 105, 90, 106], yet theoretical modeling of solids under the influence of such strong fields is quite demanding. Often phenomenological models based on experimental findings precede the advances in microscopic modeling.

Avalanche ionization is the ionization of electrons by collision with conduction band electrons



that have been heated or accelerated by the interaction with the laser field - a process that transfers energy and momentum and leads to exponential growth of the conduction band electron density. At nano-to picosecond pulse durations the avalanche ionization of electrons starts from thermally excited seed electrons or ionization from mid-gap defect states into the conduction band. It happens at a similar timescale as the energy transfer from the excited conduction band electrons to the lattice through repeated phonon emission. The damage threshold is determined by the relative rates between the energy deposition and the diffusive heat transfer away from the interaction volume. It has been shown [95] that the threshold fluence for optical damage scales with the square root of the pulse duration down to pulse durations of  $\sim 10$ -20 picoseconds. If the bandgap energy is much bigger than the photon energy (by a factor of 3 or more) the dielectric breakdown threshold is reached at intensities well below the threshold for multiphoton or tunneling absorption for such long pulses.

With femtosecond pulses it is possible to generate seed electrons via multiphoton or tunneling ionization. In this regime the heating of the electrons is much faster than the cooling of the carriers via phonon emission so that the carrier excitation is decoupled from the energy transfer to the lattice [107]. For few-hundred femtosecond pulses avalanche ionization leads to high carrier densities that cause an abrupt breakdown of the lattice structure because it does not support high conduction band densities. The damage threshold fluence is higher than the square root of the pulse duration [94, 95].

For few-cycle laser pulses ( $\leq 10$  fs at 800 nm), the direct photoionization via multiphoton absorption or tunneling ionization is believed to dominate over the avalanche process in the free carrier generation [96, 98]. In absence of (or only reduced) avalanche ionization it is possible to expose the dielectric to field strengths above  $1 \text{ V/\AA}$  and to study the interaction of such strong fields with dielectric solids at the few- to sub-femtosecond time scale. Important progress has been made in recent years in this direction, and the main techniques and findings are summarized in the next section.

### 2.3.2 Femtosecond polarization and ionization dynamics

While damage threshold measurements [95, 96, 97, 98, 99, 100, 108] give only indirect indications via scaling laws on the mechanisms that lead to high excitation levels in dielectrics and eventually to dielectric breakdown, optical pump-probe measurements can provide a closer look on the temporal dynamics of the excitation. Optical techniques that use spectral interference of a probe beam transmitted through the sample, that has been excited by a strong pump beam, with a reference replica of the probe beam are very sensitive to nonlinear phase shifts due to the increased free carrier density after excitation. In combination with an imaging spectrometer, this phase shift spectroscopy [109, 110, 111, 107, 112, 113] can even resolve changes in the excitation density in one transverse spatial coordinate. *Quéré* et al. found that the trapping time of the excited free carriers in  $\text{SiO}_2$  into self-trapped exciton states is only 150 fs. With 50 fs probe pulses and a high resolution in phase ( $\leq \lambda/200$ ) and amplitude ( $\sim 1\%$ ), Temnov et al [112, 113] could prove that the free carrier density scales with pump intensity  $I_p$  as  $I_p^\alpha$  with  $\alpha=6\pm 0.1$  up to intensities of  $I_p \sim 20$ -30  $\text{TW/cm}^2$  which indicates that the multiphoton absorption dominates the ionization process. Spatially resolved spectral interferometry is a powerful tool that gives access to the nonlinear change in phase due to the nonlinear change in refractive index and to the change in transmission. From this the ratio of the average free carrier density ( $\rho_{av}$ ) present

in the sample and the effective mass of the carriers ( $m^*$ ) can be obtained as well as the Drude electron-electron collision time  $\tau_c$  [110, 112]. However, this technique of spectral interference also has certain drawbacks when it comes to large phase shifts that tend to reduce the fringe contrast. Also the evolution of the carrier density within the temporal pump-probe-overlap cannot be resolved and only the average phase shift along the propagation axis is accessible.

When the interaction of the probe pulse with the excited medium is analyzed not by spectral interference but by characterization of the probe pulse itself either by quasi-autocorrelation [114] with a reference pulse or with the FROG technique [115], some information about the evolution of the nonlinear changes in refractive index and the role of free carrier excitation *within* the pump-probe-overlap can be obtained. However, the correlation with a pulse of similar temporal pulse width and spectrum at pulse durations much longer than the expected electron collision time of a few to less than a femtosecond [99, 113] masks the possible sub-cycle ionization dynamics.

One way to circumvent this restriction, proposed by Gertsvolf et al. [15], is the analysis of the nonlinear absorption and the ellipse rotation of an elliptically polarized beam where the major axis of the beam acts as the pump and the minor axis as a probe beam, both of which are inherently locked by a fixed delay [116]. This restricts the temporal resolution to one quarter of a wave cycle in case of a single beam. Using a fundamental and its second harmonic beam, further improvements are possible [15], yet not easy to implement. In the experiment presented in [15], the relatively long pulse duration  $\geq 40$  fs with respect to the time-scale of collisional dynamics restricted the clear observation of sub-cycle ionization dynamics.

Another approach to obtain sub-cycle information on the ionization dynamics is to look for radiation emerging from the ionization process itself. Mitrofanov et al. [117] could detect an ionization-induced sideband emission generated from the non-collinear, cross-polarized interaction of a weak probe pulse and a strong few-cycle pump pulse in SiO<sub>2</sub>. The sideband is assumed to be due to the sub-cycle ionization and subsequent change in free-carrier density induced by the pump pulse. The quasi-periodic change in bulk properties is simulated and linked induced side-band generation.

Very recently, Schiffrin et al. [1] could demonstrate that few-cycle NIR/VIS laser pulses can transiently enhance the polarizability in a dielectric on a sub-femtosecond time-scale and enable the generation of a field-dependent current in a metal-dielectric nanojunction for field strengths approaching the critical field strength  $F_{crit}$  (Eq. 2.25).

All these findings and the wealth of open questions concerning the strong field interaction in dielectric solids, and many more that could not be mentioned in the limited scope of this thesis, provide great motivation to apply and further develop state-of-the-art attosecond metrology to investigate electron dynamics in dielectrics and wide band gap semiconductors.



# Chapter 3

## Interplay between electronic and lattice dynamics in a resonantly excited semiconductor

Studying the interaction of femtosecond laser pulses with solids can provide valuable insight into the dynamics and the interaction between the lattice and the electronic subsystem. Electronic excitation and decay dynamics are revealed by pump-probe photoelectron spectroscopy, e.g. [118, 119], while time-resolved diffraction techniques provide information on dynamic lattice changes like coherent phonons and phase transitions, e.g. [120, 121, 122]. Transient changes of optical properties such as the reflectivity or the transmission [123, 124], are often the result of both electronic as well as structural changes. Coherent oscillations of the optical properties of semiconductor crystals at frequencies corresponding to their optical phonon modes can be triggered and observed by femtosecond laser pulses, which led to the generally accepted concept of coherent phonons [84, 86]. Coherent phonons are spatially extended, phase-locked lattice oscillations generated by the brisk interaction of a femtosecond laser pulse with a crystal, coupled via virtual or real electronic excitation. The coupling of the excited electronic states to the lattice potential determines the generation and relaxation dynamics of the phonon. The dynamic evolution of this coupling far from equilibrium is revealed via ultrafast excitation with intense femtosecond laser pulses [125]. The underlying structural changes in the material can be correlated with the optical response using first-principles theoretical models [126].

This chapter deals with the investigation of coherent oscillations in titanium dioxide ( $\text{TiO}_2$ ) that are resonantly excited with femtosecond UV pulses. The first section of the chapter describes the experimental setup for time-resolved reflectance measurements with femtosecond UV pulses that are generated from few-cycle laser pulses in a noble gas. An overview on the electron-phonon correlation in  $\text{TiO}_2$  based on previous works and the motivation for conducting a time-resolved investigation of the material under resonant excitation conditions is given in the second section. The third section contains the experimental results and their interpretation. A careful analysis of the coherent phonon oscillations' initial phase interpreted in the framework of a reasonable model based on density functional theory calculations of the potential energy surface of the crystal lattice reveals clear signatures of the interdependence between electronic excitation and lattice dynamics, where femtosecond response times meet femtometer-scale displacements [127].

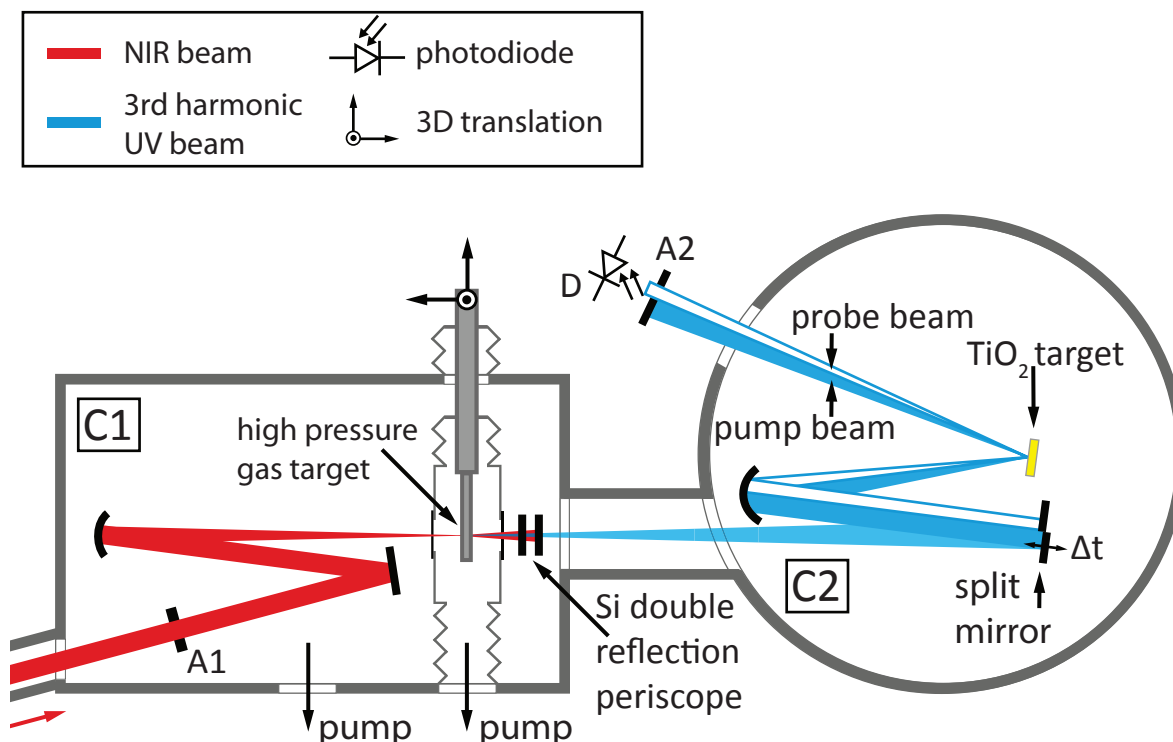


**Figure 3.1:** Experimental setup for the transient reflectance experiment consisting of two vacuum chambers, C1 and C2. The UV pulses are generated via frequency upconversion from few-cycle NIR/VIS pulses in a quasi-static gas cell and the remaining NIR/VIS radiation is suppressed by two reflections of Si surfaces under  $75^\circ$  (Brewster's angle at 800 nm) before the reflectance measurement. The UV beam is separated in a strong pump beam and a weak probe beam and focused on the  $\text{TiO}_2(110)$  surface and the reflected intensity of the probe beam is recorded as a function of the pump-probe delay  $\Delta t$ .

### 3.1 Setup for ultraviolet pump-probe transient reflectance experiments

The femtosecond UV pulses employed in the one-color pump-probe reflectance measurements are generated by third harmonic generation using sub-4-fs NIR/VIS pulses with a central wavelength of 780 nm. Fig. 3.1 shows a sketch of the experimental setup for the transient reflectance experiment with UV pulses generated as the third harmonic from few-cycle driver pulses. In an evacuated beamline setup (chamber C1) developed for high and low harmonic generation [49], the NIR/VIS pulses are focused into an open gas cell. The gas cell consists of a 3 mm thin nickel tube with two laser-drilled entrance and exit holes with a diameter of about 100-150  $\mu\text{m}$  and is supplied with neon at a variable pressure of up to 6 bar. To minimize the dispersion experienced by the UV pulses after generation, differential pumping of a small volume enclosing the gas cell ensures a base pressure of  $10^{-3}$  mbar in the other parts of the beamline despite the high possible gas load.

Direct up-conversion from the few-cycle NIR/VIS driving laser pulses yields near-transform-limited pulses in the deep UV with a bandwidth of up to 40 nm (full width at half maximum) centered around 245 nm [46] corresponding to a Fourier-limit of  $\sim 3$  fs. Fig. 3.2 shows a typical

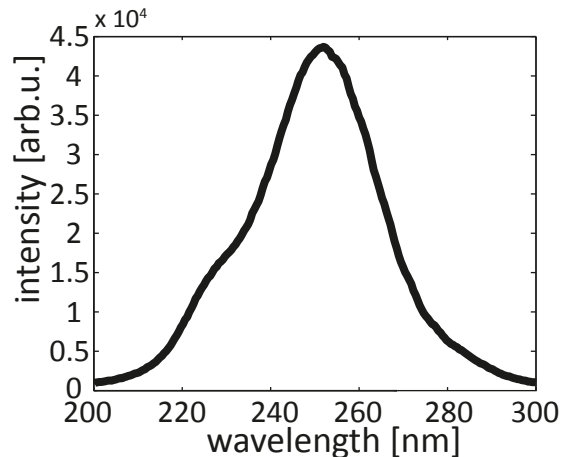


**Figure 3.2:** Spectrum of the third harmonic generated of the sub-4 fs NIR/VIS driving pulse generated in a neon gas target at 6 bar [37].

UV spectrum achieved at a Ne gas pressure of 6 bar in the quasi-static gas cell.

The conversion efficiency from NIR/VIS to the UV under these conditions is at the order of 0.25-0.5%. For the one-color pump-probe experiment, the UV is separated from the NIR/VIS by two reflections from silicon wafer surfaces under the NIR/VIS Brewster's angle, which is an efficient way to suppress the broadband NIR/VIS by about two orders of magnitude per reflection with a reflectivity of about 60% in the UV. The pulse energy available after NIR/VIS suppression can be tuned from  $\sim 75$  nJ to  $\sim 140$  nJ by varying the neon pressure in the gas cell. After suppression of the NIR/VIS radiation, the UV beam is separated in a pump beam and a probe beam with an intensity ratio of  $\sim 3:1$  by a mask and a flat split mirror. Both beams are focused by a spherical mirror (focal length  $f=150$  mm) at  $15^\circ$  angle of incidence on a  $\text{TiO}_2(110)$  surface with the (001) direction parallel to the polarization of the UV light. With a pump beam spot diameter of about  $100 \mu\text{m}$  the available UV pump fluence range is  $0.7 \text{ mJ}/\text{cm}^2$  to  $1.3 \text{ mJ}/\text{cm}^2$ .

One half of the split mirror is mounted on a piezo actuated linear stage. This allows to introduce a relative delay between pump and probe, either in controlled steps with a small range position modulation at a frequency up to 20 Hz for differential detection of the reflected signal or in a larger amplitude oscillatory motion around the temporal overlap position with a lower frequency of 10 Hz. The reflected probe intensity is detected with a UV sensitive silicon-carbide photodiode (sglux) and a fast gated integrator (Stanford Research boxcar).

In case of the method of fast modulation around the single delay steps, the signal acquired with lock-in amplification sensitive to signals at the modulation frequency corresponds essentially to the first delay-time-derivative of the probe intensity [128]. The magnitude of the signal is proportional to the modulation amplitude, but with increasing modulation range, the temporal resolution decreases, so the modulation range of the time-delay was set to 320 nm, corresponding to a delay range of  $\Delta t \sim 2.2$  fs.

The second method, where the whole delay range of interest is scanned repeatedly at frequencies up to 18 Hz, the signal is averaged over several thousand traces on a fast oscilloscope. This method allows to determine the absolute magnitude of changes in reflected intensity and reduces low-frequency noise significantly.

## 3.2 Electron-phonon correlations in TiO<sub>2</sub>

Titanium dioxide (TiO<sub>2</sub>) is a wide band gap semiconductor which found broad application as a photo-protective material in its nanocrystalline form and for photocatalytic purposes as it facilitates oxidation near its surface [129, 130, 131]. Recently it was also found to exhibit useful optoelectronic properties for example in photovoltaic applications [132, 133] in dye-sensitized solar cells. In its most thermodynamically stable form [134], rutile TiO<sub>2</sub>, the optical absorption edge corresponds to an indirect bandgap at 3 eV [135, 136] involving a 2p<sub>xy</sub> exciton state, while the direct transition at this energy is dipole-forbidden. At 4.2 eV there is a dipole-allowed direct transition [137].

As in many transition metal oxides, there is a strong correlation between excited charge states and lattice excitations in form of phonons [84, 138]. The different phonon modes present in rutile TiO<sub>2</sub> [139] can be accessed experimentally with IR and UV Raman spectroscopy [137, 140, 141]. A resonant Raman study [137] observed an enhancement of the scattering efficiency of the Raman-active phonon with A<sub>1g</sub> symmetry at ~18.3 THz at low temperatures and attributed it to an exciton double resonance at 3.03 eV.

Nomoto et al. [142] observed the excitation of seven IR-active coherent phonon modes in the fourth order surface response from a rutile TiO<sub>2</sub>(110) surface with time-resolved second harmonic generation spectroscopy. They used intense (8 mJ/cm<sup>2</sup>) 25 fs pulses centered at 2 eV for off-resonance excitation. Simultaneous transient reflectivity measurements supported ISRS (cf. chapter 2.1) as the excitation mechanism for one of the Raman-active bulk phonons with a frequency of 18.3 THz and A<sub>1g</sub> symmetry. In a more recent study, Ishioka and Petek [143] varied the pump and probe photon energy of 10 fs near-UV pulses centered at 400 nm (3.11 eV) in a small (0.08 eV) range above the fundamental absorption edge of rutile TiO<sub>2</sub> with a pump fluence of ~0.1 mJ/cm<sup>2</sup>. The authors conclude that the absence of the resonant enhancement of the A<sub>1g</sub> mode that has been reported earlier [137] is mainly due to the indirect and the direct-forbidden nature of the gaps in this energy range, while additional enhancement due to the excitonic double resonance is suppressed as a consequence of the detuning of their excitation energy. This also explains the observed non-resonant ISRS generation mechanism. Direct-allowed resonant excitation is mentioned as a possible way to observe the resonant enhancement of the A<sub>1g</sub> phonon scattering efficiency for obtaining further insight into the electron-phonon interaction [143].

In a time-resolved THz conductivity experiment, Hendry et al. [144] established that large electron-phonon scattering rates in single crystal rutile TiO<sub>2</sub> are connected to the formation of intermediate size polarons. This partly explains the low mobility of the electrons within the bulk material at room temperature. The transfer of hot electrons across interfaces involving a TiO<sub>2</sub> surface is limited by fast deexcitation via electron-phonon scattering, shown by Tisdale et al. [145]. Zhukov and Chulkov [146] investigated theoretically the different time scales for electron-phonon energy transfer and hot-carrier cooling. They found a strong dependence of carrier cooling times on the excitation energy within the conduction band ranging from picoseconds for meV-range excitation energies to a few femtoseconds for electrons with several eV excitation energy. A better understanding of the relaxation of hot electron populations in resonantly excited semiconductors might provide ways to tailor efficient electron transfer channels in hot-carrier solar cells.



### 3.3 Ultrafast evolution of the excited-state potential energy surface of TiO<sub>2</sub>

Under resonant excitation of a TiO<sub>2</sub>(110) single crystal surface with sub-4 femtosecond UV pulses (cf. chapter 1.2) centered at 4.5 eV and linearly polarized along the (001) direction, the reflected probe signal in the one-color transient reflectivity experiment described in the previous chapter 3.1 drops by 3.5% at zero delay between pump and probe, see Fig. 3.3 a. This is followed by a periodic modulation of the signal with an amplitude of up to 0.3% with a period of 55 fs, corresponding to a frequency of 18.1 THz or a wavenumber of 603 cm<sup>-1</sup>. The first, step-like decrease in reflectivity is attributed to the resonant excitation of electrons into the conduction band. The subsequent periodic modulation is an indication for the excitation of a coherent phonon (cf. chapter 2.1). Fig. 3.3 a shows the  $\Delta R/R_0$  probe signal obtained by rapid scanning of the delay  $t$  between pump and probe at a rate of 10 Hz in combination with a high number of averages. As the delay-differential method (cf. chapter 3.1) with small-amplitude modulation and lockin-based detection at 18 Hz yields a slightly better signal-to-noise ratio, it shall be used in the following data fitting and interpretation. This signal corresponds to the delay-time-derivative of the reflectivity  $\delta R/\delta t$ , as plotted in Fig. 3.3 b.

In order to extract information on the dynamics of the coherent phonon, an exponentially decaying sine function (Eq. 3.1) with frequency  $\omega$  and phase  $\Phi$  is fitted with a least-squares method to the oscillating derivative signal, with the amplitude  $A$  and an exponential decay time  $\tau \sim 220$  fs. The fit results of  $A$ ,  $\omega/2\pi$  and  $\Phi$  for pump fluences ranging from 0.7 mJ/cm<sup>2</sup> to 1.3 mJ/cm<sup>2</sup> are shown in Fig. 3.4. In the range of applied pump fluences, the initial amplitude of the oscillation increases proportionally, while the frequency and the phase remain constant. The coherent phonon frequency corresponds to the longitudinal optical phonon with symmetry A<sub>1g</sub> and a frequency of  $\sim 18.1$  THz which has been observed before under non-resonant and near-resonant excitation[139, 142, 143]. In contrast to the previous works, this time-resolved study on TiO<sub>2</sub> involves transitions above the direct allowed bandgap at 4.2 eV.

$$\delta R/\delta t \sim A \cdot \exp(-t/\tau) \cdot \sin(\omega t + \Phi) \quad (3.1)$$

Unexpectedly, the phase  $\Phi$  deviates considerably by  $0.2\pi$  from a clear cosine oscillation, which would be expected in case of resonant excitation and the corresponding DECP mechanism. The initial step drop in reflectivity corresponds to the excitation of electrons into the conduction band. The phase shift of the coherent phonon relative to a cosine oscillation with respect to the electronic excitation can be interpreted as a temporal delay of the coherent phonon excitation. It corresponds to  $\sim 5.5$  fs or 10% of the phonon oscillation period. The possible reasons for this significant deviation from the DECP phase are investigated in the following.

First, the possibility of a significant measurement-induced shift between the detected phase and the coherent motion of the phonon coordinate  $Q(t)$  has to be ruled out. In section 3.1 the delay-differential signal has been presented to correspond essentially to the first delay-time derivative of the direct time-resolved signal. Taking into account a damped oscillation as the one observed in the experiment, certain corrections have to be considered. The derivative of a damped signal with a damping constant of  $\gamma_d = 1/\tau$  leads to an additional phase shift (see also



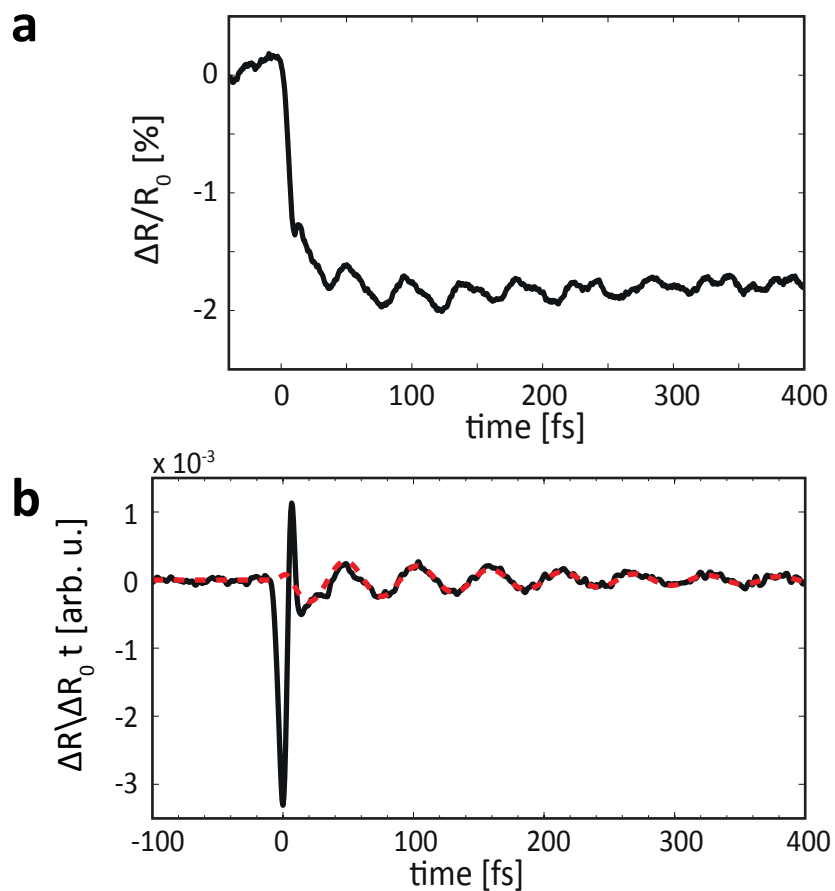


**Figure 3.3:** Transient UV reflectivity of  $\text{TiO}_2$  recorded with the rapid scanning technique  $\Delta R/R_0$  **a**, and delay-differential signal  $\delta R/\delta t$  **b**. The red dashed line shows the fit to the data with Eq. 3.1.

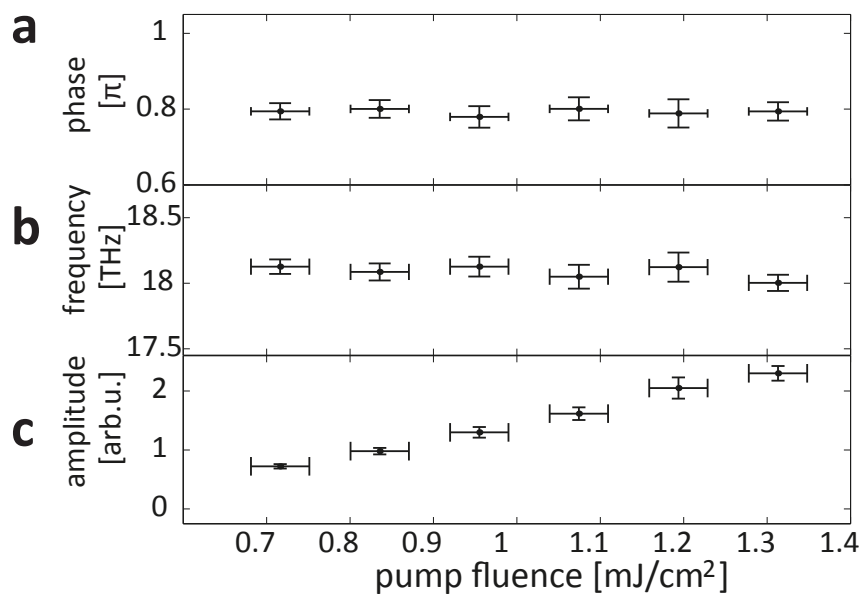


**Figure 3.4:** Fit results of the phonons' phase **a**, frequency **b** and amplitude **c** as a function of the pump fluence.

[127], supplemental material):

$$\begin{aligned}
 \frac{\delta R}{\delta t}(t) &\approx \frac{d}{dt} \left( C \exp\left(-\frac{t}{\tau}\right) \cos(\omega t + \phi) \right) \\
 \frac{\delta R}{\delta t}(t) &= C \exp\left(-\frac{t}{\tau}\right) \left( -\frac{1}{\tau} \cos(\omega t + \phi) - \omega \sin(\omega t + \phi) \right) \\
 \frac{\delta R}{\delta t}(t) &= -C \sqrt{\left(\frac{1}{\tau}\right)^2 + \omega^2} \exp\left(-\frac{t}{\tau}\right) \sin\left(\omega t + \phi + \arctan\left(\frac{1}{\tau\omega}\right)\right) \\
 &\Rightarrow \phi_{exp} = \phi + \arctan\left(\frac{1}{\tau\omega}\right),
 \end{aligned} \tag{3.2}$$

where the experimentally observed phase shift  $\phi_{exp}$  is the phase shift of the coherent phonon with a small correction  $\arctan\left(\frac{1}{\tau\omega}\right)$  originating from the damping constant. In the experiment, the damping constant is  $\gamma_d = 1/200 \text{ fs}^{-1}$  for the oscillation at  $\omega \sim 2\pi \cdot 18.1 \text{ THz}$  which corresponds to a correction term of  $0.014 \pi$  much smaller than the experimentally observed shift of  $0.2\pi$ .

In a second step, the physical mechanisms within the DECP model have to be considered, that could lead to an apparent phase shift in the observed oscillation. On the one hand, electron-hole recombination [85] can be ruled out as it happens on a picosecond time scale [147, 146]. Carrier diffusion away from the pump-probe volume is equally unlikely at the few-femtosecond timescale for a probed depth of several nanometers due to the low room temperature mobilities in TiO<sub>2</sub> [148]. The phonon damping as a consequence of Raman resonances or excitation lifetimes [85] on the other hand can have a contribution to the phase shift. Following the approach by Riffe et al. [85], the motion of the coherent phonon coordinate  $Q(t)$  is modeled by an externally driven harmonic oscillator with a damping constant  $\beta$  and the undamped eigenfrequency  $\omega_0$  of a mass  $\mu$ .

$$\mu \left[ \frac{\partial^2 Q(t)}{\partial t^2} + 2\beta \frac{\partial Q(t)}{\partial t} + \omega_0^2 Q(t) \right] = F(t), \tag{3.3}$$

In case of purely displacive excitation, the driving force  $F(t)$  corresponds to a step-like function usually approximated by the Heaviside-function  $F_0 \cdot \Theta(t - t_0)$  with a magnitude of  $F_0$  proportional to the density of photo-excited carriers or to a temperature difference [84]. In absence of damping ( $\beta = 0$ ), this model describes a cosine motion of  $Q(t)$  without phase shift. The finite life time of the excited electron-hole pairs leads to a decay rate  $\gamma$  of the driving force. In the DECP limit, the phase shift is according to [85] determined as

$$\Delta\phi_{DECP} = \arctan(\bar{\gamma} - \bar{\beta}) \tag{3.4}$$

with  $\bar{\beta} = \beta/\omega$  and  $\bar{\gamma} = \gamma/\omega$ . Given that  $\gamma \ll \omega$  for TiO<sub>2</sub> [146], the contribution to the phase shift is dominated by the damping of the phonon determined by  $\bar{\beta}$ . With the experimental values of  $\tau \sim 200 \text{ fs}$  and  $\omega = 2\pi \cdot 18.1 \text{ THz}$ , this phase shift is also very small, i.e.  $\Delta\phi_{DECP} = \arctan(-\bar{\beta}) \sim -0.014$ . This is much smaller than the experimentally observed phase shift of  $\phi_{exp} = -0.2\pi$ . Besides that, it is noteworthy that this damping-induced phase shift is exactly compensated by the phase shift induced by using the delay-differential technique.

As the experimentally observed phase shift can not be accounted for by the damping, a new model for the temporal evolution of the driving force has been developed in collaboration with

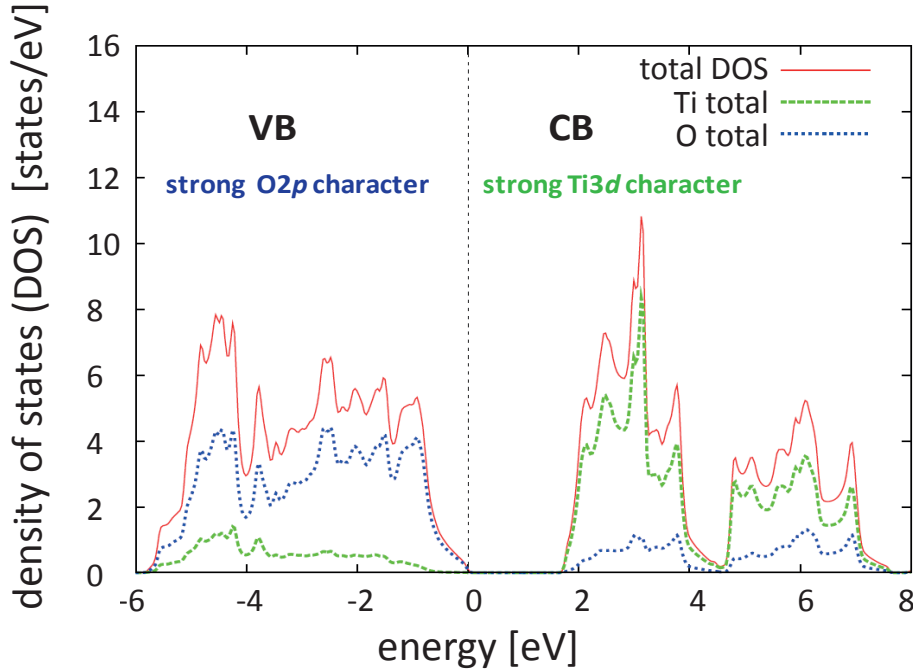


**Figure 3.5:** Density of states in the valence and conduction band in rutile TiO<sub>2</sub> calculated with Wien2k. Courtesy of N. Karpowicz.

Euwe S. Zijlstra and Martin E. Garcia from the University of Kassel. Under the present excitation conditions using a photon energy of  $\sim 5$  eV which exceeds the indirect bandgap of 3 eV and the direct allowed bandgap of 3.9-4.2 eV [149], hot electrons with an electronic temperature of more than one eV are created within the conduction band. The short UV pulse duration leads to a sudden change of the electron distribution upon resonant excitation. While the valence band density of states is dominated by O 2p states, the main proportion of conduction band states exhibits Ti 3d character [150, 151] as shown in Fig. 3.5. Consequently, the resonant interband excitation from the valence band to the conduction band corresponds to a redistribution of charges in real space. The PES of the lattice is expected to be altered correspondingly. It is linked to the charge distribution via a complex functional that can be modeled with density functional theory.

In order to explore the interaction between the electronic and the lattice subsystem, the potential energy surface (PES) of TiO<sub>2</sub> was modeled using the density-functional theory code Wien2k [152]. Methodological details used for this calculation are equivalent to the methodology reported in [153] and the parameters of the calculation of the present experiment can be found in the appendix A.1.

The influence of photo-excitation with the creation of a hot electron population with energies high above the conduction band minimum and subsequent cooling of these hot carriers down to the conduction band minimum is investigated by comparing these two limiting cases with the ground state of the system. The two excited states will be referred to as hot excited state and cool excited state in the following. The respective potential energy surfaces of the oxygen atom position  $u$  along the  $A_{1g}$  phonon coordinate are calculated in units of  $\sqrt{2}a$  with the lattice

parameter  $a=4.593\text{\AA}$ .

First, the ground state of the system is calculated. The minimum of its PES, shown in Fig. 3.6 as black solid line, is at  $u=0.3048$  and from the curvature of the parabolic PES a frequency of 17.9 THz can be deduced, which both agree well with experimentally determined values [139]. The hot excited state is modeled assuming an average excess energy of 1 eV of 0.1 excited electron-hole pairs per unit cell. This energy is insufficient to create additional electron-hole pairs through carrier-carrier scattering processes and the lifetime of the excited state is on the picosecond timescale [146]. Therefore the number of excited carriers remains constant, when the carriers cool down. Through emission of high-frequency (17.9 THz) phonons, the hot electrons in the conduction band relax to room temperature (0.027 eV) within a few tens of femtoseconds. The PES of the hot and the cool excited state are depicted in Fig. 3.6 as red dashed line and as blue dotted line.

Fig. 3.6 clearly shows the shift of the PES minimum along the  $A_{1g}$  coordinate upon excitation,

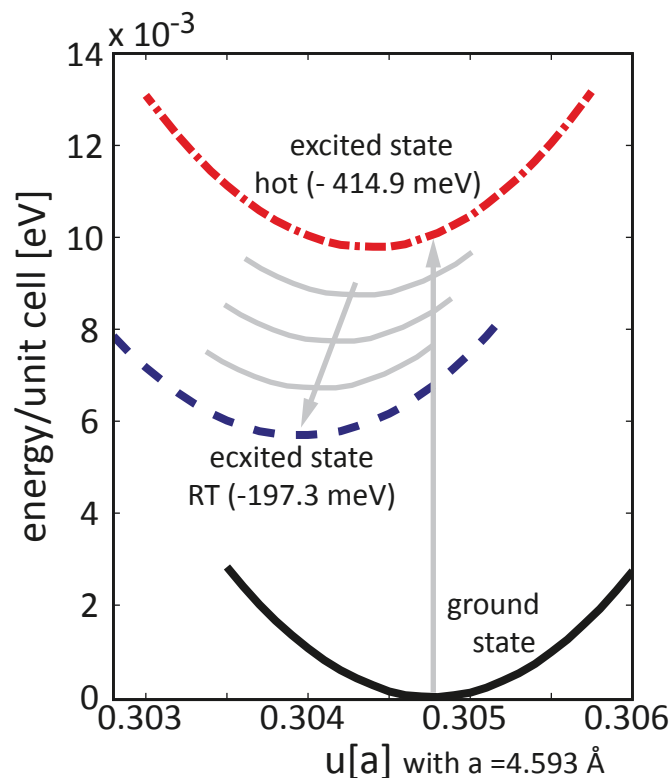


**Figure 3.6:** Potential energy surfaces of the ground state (solid black line) and the hot (dashed red) and cold (dotted blue) excited states projected along the  $A_{1g}$  phonon coordinate. The minimum of the PES is displaced significantly upon excitation and again upon relaxation. In the plot the PES of the hot and the cold excited state have been offset by  $-419.9\text{ meV/unit cell}$  and by  $-197.3\text{ meV/unit cell}$ , respectively.

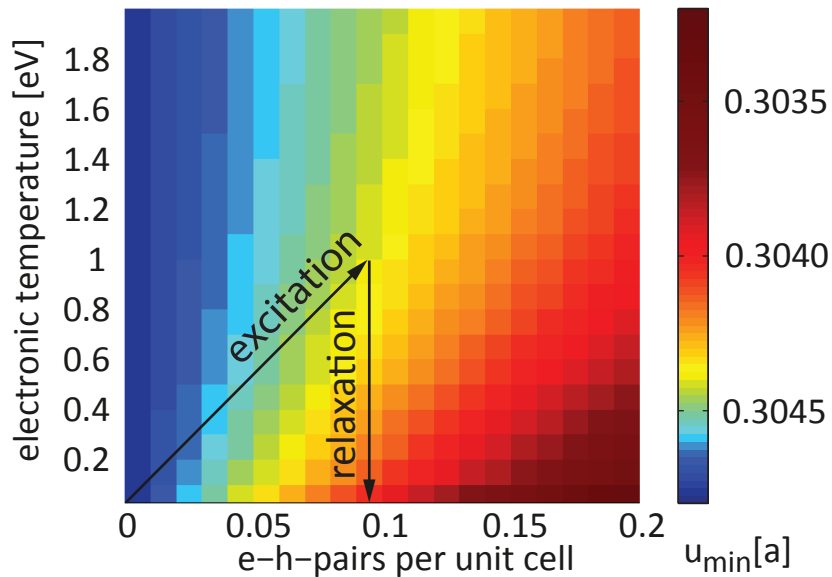
which corroborates the displacive nature of the driving force that creates the coherent phonon oscillation around the new minimum of the PES. What is surprising at first sight is that upon relaxation, the PES minimum is significantly shifted further in the *same* direction as upon excitation, while relaxation generally tends to reverse the system's evolution back towards the ground state. In  $\text{TiO}_2$  the opposite seems to prevail.

Fig. 3.7 shows how the minimum of the PES depends on the number of electron-hole-pairs per

unit cell and on the temperature of the electrons. The two-dimensional plot shows clearly that upon excitation of hot electron-hole-pairs and their subsequent relaxation within the conduction band the PES experiences a unidirectional shift independent of the exact excitation parameters used in the model.

This general behavior of TiO<sub>2</sub> can be intuitively understood by considering the density of states (Fig. 3.5) and the occupation in the ground state and the two excited states. As mentioned above, optical excitation from the valence to the conduction band involves an effective charge transfer from the oxygen atoms to the titanium atoms within the unit cell. While at higher excitation energy above the conduction band minimum for the electrons or below the valence band maximum for the holes also the minority Ti 3*d* and O 2*p* states contribute to the density of states respectively, nearly pure O 2*p* states in the valence band and pure Ti 3*d* states in the conduction band are present at the band edges. The relaxation from higher excited states towards the band edges therefore *increases* the charge transfer within the unit cell. Fig. 3.8 compares the charge redistribution in the hot (a) and cool (b) excited states with respect to the ground state in one half of the unit cell. Positive (red) and negative (blue) changes in valence electron density are depicted as iso-surfaces with  $\pm 0.0005$ ,  $\pm 0.003$  and  $\pm 0.0055$  e/a<sub>0</sub><sup>3</sup> (e is the electron charge, a<sub>0</sub> the Bohr radius). In the hot excited state, a clear increase in electron density around the titanium atoms (green) can be observed, while the electron density around the oxygen atoms (yellow) decreases (Fig. 3.8 a). When the electrons subsequently cool down towards the band edge and eventually reach the cold excited state, the accumulated charge transfer with respect to the ground state is raised again by approximately the same amount (Fig. 3.8 b).

The calculation of the PES for the three limiting cases allows to identify the intra-unit-cell charge transfer and the corresponding shift of the PES minimum as the driving force behind the coherent phonon oscillation. The knowledge on the evolution of the excited state PES minimum in function of the electron temperature allows to interpret the experimentally observed ultrafast



**Figure 3.7:** Position of the PES minimum as a function of the number of excited electron-hole-pairs per unit cell and the electronic temperature. The black arrows indicate the hot and cold excited state parameters used for calculating the PES in the experimentally applied fluence regime.

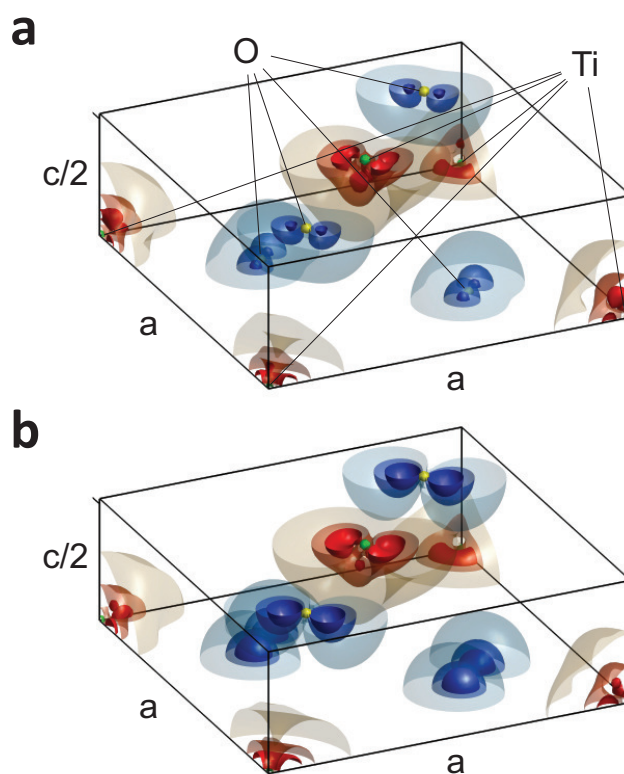


**Figure 3.8:** Isosurfaces of change in valence electron density in the half unit cell of rutile TiO<sub>2</sub> around the oxygen (yellow) and titanium (green) atoms for the hot (**a**) and the cold (**b**) excited state with respect to the ground state. Positive (more charge, red) and negative (less charge, blue) change in electron density are shown for three exemplary isosurfaces with  $\pm 0.0005$ ,  $\pm 0.003$  and  $\pm 0.0055 e/a_0^3$ , [127] Copyright (2013) by the American Physical Society.

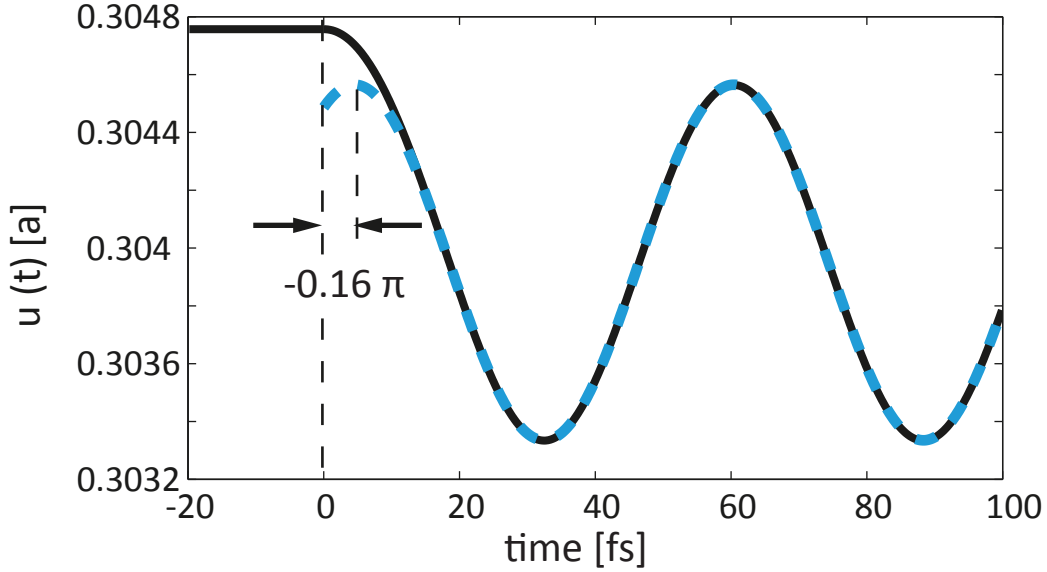


**Figure 3.9:** Motion of the oxygen atom (solid black line) simulated by assuming a linearly evolving potential from the hot to the cold excited state PES for the first 20 fs after excitation at  $t_0=0$  fs and a constant PES thereafter. For comparison the dashed blue line describes a cosine with a phase shift of  $-0.16\pi$ , marked with the dashed vertical lines and black arrows. Both curves coincide after  $t=20$  fs.

phonon dynamics in view of a dynamically evolving driving force. The time scale of  $\sim 2$  fs for the emission of a single phonon by an excited electron has been determined theoretically by Zhukov and Chulkov [146]. It is independent of the initial electron energy, which supports the values obtained in an earlier time-resolved THz transmission experiment [144]. The calculated minima of the PES are combined with the electron relaxation dynamics described in [146] to simulate the atomic motion on the evolving PES. The total relaxation time of hot electrons with 1 eV initial excess energy to room temperature is taken to be  $\sim 20$  fs. The relaxation rate for the holes should be similar to that, although they are not mentioned explicitly in reference [146]. Directly after the excitation, the minimum of the PES is assumed to be shifted linearly between the two limiting cases of the hot and the cold excited state at  $t=0$  fs and  $t=20$  fs, respectively. It is held constant at the value of the cold excited state for  $t \geq 20$  fs. By integrating Newton's equation of motion for the time-dependent potential, the trajectory of the oxygen atoms is calculated along the  $A_{1g}$  coordinate, shown in Fig. 3.9.

For times  $t \geq 20$  fs the motion of the oxygen atom coincides with a cosine motion at 17.9 THz exhibiting a phase shift of  $-0.16\pi$  relative to  $t=0$  fs, which is very close to the experimentally observed value of  $-0.2\pi$ . This agreement between a simulation under reasonable assumptions and the experimental value provides evidence that indeed a dynamically evolving PES minimum is responsible for the deviation from a clear cosine oscillation. Two factors influence the magnitude of this deviation. On the one hand, one can compare the carrier relaxation time scale  $\tau_{rel}$  with the oscillation period of the optical phonon  $T_{ph}$ . If  $\tau_{rel} \gg T_{ph}$ , the phase shift will be negligible. On the other hand, if  $\tau_{rel} < T_{ph}$ , the ratio between the instantaneous shift in PES minimum induced by carrier excitation and the fast dynamic shift due to carrier relaxation might depend

on the excitation level. Experimentally we found a constant phase shift of  $-0.2\pi$  for excitation levels up to 0.1 electron-hole-pair per unit cell with an initial electronic temperature of 1 eV. In this range the ratio between instantaneous and dynamic shift of the PES minimum remains approximately constant, see Fig. 3.6, which supports the experimental findings.

In conclusion, the ultrafast resonant excitation of TiO<sub>2</sub>(110) single crystals with femtosecond UV pulses induces coherent optical phonons through a displacive excitation mechanism. The experimentally observed deviation of the coherent phonon oscillation from a clean cosine oscillation by  $-0.2\pi$  points towards the existence of a second displacive driving mechanism in addition to the resonant generation of electron-hole pairs. A model based on density-functional theory calculations of the structural response to electronic excitation [127, 154] and corresponding simulations of the electron density reveal that ultrafast carrier relaxation contributes to the shift of the PES minimum in equal magnitude as the initial excitation. Such fast relaxation processes of a laser-excited non-equilibrium population of carriers may play an important role in determining the initial structural response to femtosecond laser pulses, e.g. laser-induced phase transitions [138], for a wide range of materials. While in TiO<sub>2</sub> the relaxation contributes positively to the excitation-induced shifts of the PES minimum [127, 154], the relaxation process might partially balance or even reverse the direction of the excitation-induced PES shift in other materials. In addition, it could even influence a different dimension in configuration space. Therefore the electron relaxation mechanisms have to be taken into account in the interpretation of coherent phonon excitation mechanisms under resonant excitation conditions. The presented experiment and its interpretation demonstrate the significance of the equilibration dynamics of a laser-excited carrier population for the initial structural response at the femtosecond time scale.





# Chapter 4

## Strong-field induced electron dynamics in SiO<sub>2</sub>

Fused silica, the amorphous form of SiO<sub>2</sub> has found many applications in modern technology. Fiber-optic communication based on low-loss fused silica fibers allows for data transmission rates at tens of GHz (1 GHz=10<sup>9</sup> s<sup>-1</sup>). In current metal oxide semiconductor field-effect transistors SiO<sub>2</sub> forms the nanometer thin insulating layer in the capacitor between the gate and the p-n-junction. In modern electronics the gate voltage is modulated at GHz rates with low field strengths that permit the reversible formation of a conducting channel in the carrier depleted region of the junction due to migration of delocalized conduction band electrons or valence band holes in semiconductors. The maximum modulation frequency and minimum drive voltages are limited by energy dissipation through recombination and scattering processes. In contrast to semiconductors the charges in a dielectric such as SiO<sub>2</sub> are immobilized as the valence band is completely filled and the large bandgap  $\Delta_{gap}$  prevents thermal excitation of carriers into delocalized states. Thus high field strengths are required to modify its physical properties [155, 156, 157, 158].

For static or narrow-bandwidth pulsed electric fields, the field strength that could possibly induce a reversible conductivity in the material exceeds the dielectric breakdown threshold of the material by orders of magnitude [93]. However, when the electric field is applied in form of a short laser pulse, the optical breakdown threshold field strength is inversely proportional to the square root of the laser pulse duration down to the picosecond regime, e.g. [94, 95, 96]. Even higher below-damage field strengths are possible for femtosecond pulses [96, 98]. Schiffrin et al. [1] could recently demonstrate that the AC-conductivity of SiO<sub>2</sub> embedded in a nanometric-sized capacitor can be increased by 18 orders of magnitude by linearly polarized few-cycle NIR/VIS laser pulses. The induced current could be switched on within times shorter than 1 femtosecond by optical electric field strengths exceeding 1 V/Å and its polarity could be controlled by changing the field asymmetry of a second few-cycle pulse polarized perpendicularly to the electrodes and the pump pulse. The underlying physical phenomena that enable such a rapid increase in polarizability in a dielectric are governed by the modification or *dressing* of the electronic states of the material. Real-time observation of this electronic response to the optical field requires attosecond temporal resolution. At the same time a reasonable spectral resolution needs to be achieved to identify the electronic states involved.

Wirth, Goulielmakis et al. [5, 159] have recently extended the well-established concept of time-resolved or transient absorption spectroscopy of an atomic gas to the attosecond time domain by using few-cycle NIR/VIS pump pulses in combination with attosecond XUV probe pulses. They were able to observe the valence electron motion in excited states of krypton atoms and to identify the coherent motion of these electrons that has been launched by the pump pulse. In the framework of this thesis this concept of attosecond transient absorption spectroscopy (ATAS) [5] has been applied for the first time to investigate electron dynamics *inside* condensed matter. A strong electric field provided by a few-cycle optical pulse modifies the electronic states in a dielectric solid (fused silica) and the unfolding electron dynamics are recorded with attosecond resolution. In combination with simultaneous attosecond streaking, the experiment presented in the following provides real-time insight into condensed matter electron dynamics driven by the electric field of light [64].

## 4.1 Experimental setup for broadband attosecond probe spectroscopy

The experimental setup for broadband attosecond probe spectroscopy (Fig. 4.1) is a modified version of the apparatus designed and set up by Fiess et al. [160, 21], the first of second generation attosecond beamlines at the Max-Planck-Institute of Quantum Optics based on a NIR-XUV-interferometric concept. Few-cycle NIR/VIS driving laser pulses are combined with isolated attosecond pulses with sub-100 as duration for pump-probe-type experiments on sub-micrometer thin films of SiO<sub>2</sub>. In comparison with the widely used collinear NIR-XUV setup [13, 63, 20, 161], the spatial separation after the HHG process allows for a greater flexibility in controlling and modifying the NIR/VIS pulse and the XUV pulse properties, before both beams are recombined at the experimental interaction region. In order to prevent temporal spread of the laser and XUV pulses due to dispersion, the entire setup resides in vacuum chambers with vacuum conditions ranging from  $5 \cdot 10^{-3}$  mbar at the HHG region to  $10^{-6}$  mbar at the experimental interaction region.

The setup consists of three main parts situated in three connected vacuum chambers. It starts with the high harmonic generation of attosecond XUV pulses. This is followed by a chamber that houses a NIR/VIS-XUV interferometer for the independent manipulation of and introduction of a relative delay between the XUV pulses and the NIR/VIS pulses. Before the entrance to the last chamber, the experimental chamber, the NIR/VIS beam and the XUV beam are joined to be collinear again and focused before entering the setup for XUV transient absorption and streaking field characterization.

In the HHG chamber (C1), vertically polarized, few-cycle NIR/VIS laser pulses with a pulse energy of  $\sim 300\text{-}400 \mu\text{J}$  are focused with a concave silver mirror with 60 cm focal length on a metal tube (nickel or stainless steel), which serves as a quasi static gas cell (HHG gas target). The laser intensity can be adjusted for optimal HHG with a variable aperture (A1). For isolated attosecond pulses in the energy range of 90-140 eV, the gas target is supplied with  $\sim 250$  mbar neon. More details on this standard setup for high harmonic generation from atomic gases can be found in chapter 1.3.3 and [21].

### 4.1.1 XUV-NIR Mach-Zehnder interferometer

The XUV radiation from the HHG target exhibits a smaller divergence than the NIR/VIS beam due to its smaller wavelength of  $\sim 12$  nm. The XUV beam can therefore be separated from the NIR/VIS beam by a mirror with a central hole ( $\varnothing$  1mm, perforated mirror PM1), which reflects an annular portion of the NIR/VIS under an angle of incidence of  $45^\circ$  and transmits the XUV and the central part of the NIR/VIS through the hole. The transmitted NIR/VIS radiation is subsequently blocked by a thin metal foil which is transparent for XUV light (150 nm molybdenum for the energy range above  $\sim 80$  eV) mounted on a filter wheel, so that only the XUV radiation propagates in the one arm of the interferometer. The negative group velocity dispersion of the metal in the XUV spectral range also reduces the intrinsic positive chirp of the attosecond pulses originating from short trajectories in the high harmonic generation process [54, 162, 19]. The triangular interferometer geometry, see Fig. 4.1, requires a deflection of the XUV beam by 90 degrees, which is realized by three subsequent reflections from Rhodium-

## 4.1 Experimental setup for broadband attosecond probe spectroscopy

---

coated super-polished silicon substrates (Gooch&Housego), each under an angle of incidence of 75 degrees. This geometry is beneficial both for the attainable XUV flux as well as for the transmitted XUV bandwidth in comparison to the near-normal incidence reflectivity and bandwidth of multilayer mirrors designed for attosecond pulses [21]. This configuration provides a full-width at half-maximum XUV bandwidth of more than 40 eV centered around  $\sim 115$  eV with a combined peak reflectivity above 50% which is ideally suited for broadband attosecond absorption spectroscopy around the Si  $2p$  L-edge absorption in  $\text{SiO}_2$  at 109 eV.

In the XUV arm of the interferometer, the XUV beam profile and spectrum can be deviated from the interferometer beam path for characterization and optimization. Two mirrors consisting of super-polished silicon substrates coated with 80% gold and 20% palladium (Georg Albert physical vapor deposition) are mounted on a linear step motor stage which moves transversely to the beam axis and allows to move either mirror in the beampath for XUV diagnostic purposes. The first mirror (GM1) is mounted under  $\sim 80$  degree angle of incidence and reflects the XUV beam via a second gold-coated mirror directly on a XUV-sensitive charge coupled device camera (XUV CCD1, PIXIS XO, Roper Scientific). Binning over the whole beam profile provides a quantity proportional to the number of XUV photons in the integration time interval. For XUV flux optimization, the dynamic range of detection is extended by inserting metal filters (zirconium, Zr) of different thickness (150 nm, 500 nm, 1500 nm) in the diagnostic beampath with a filter wheel to attenuate the beam. The second mirror on the translation stage (GM2) is laterally offset and mounted under a slightly higher angle of incidence. It redirects the XUV beam onto a flat-field concave grating (grating 001-0255, Hitachi [163]) that disperses the XUV radiation in horizontal direction with approximately linear dispersion in wavelength. Two well-defined absorption edges of aluminum and silicon thin film filters, which can be inserted in the diagnostic beampath with the filter wheel, are used to calibrate the spectrum to energy [21]. This diagnostic allows to optimize the HHG for isolated attosecond pulse generation which results in a smooth, unmodulated spectrum in the energetically relevant cut-off region as described in chapter 1.3.2.

In the other arm of the spectrometer, the annular NIR/VIS beam diameter is reduced by a ratio of  $\sim 4:1$  while the divergence is maintained by a combination of a concave and a convex silver mirror. The focal lengths and distances have to be chosen such that the diagonal arm length matches the length of the XUV arm. Small angles of incidence are required to minimize the astigmatism resulting from the spherical optics. The concave mirror is mounted on a piezo-actuated linear stage (PZT) along the mirror normal with nanometer resolution (piezosystems jena) with 100  $\mu\text{m}$  range to introduce the temporal delay  $\Delta t$  of the NIR/VIS pulses with respect to the XUV pulses required for time-resolved measurements. In addition, the concave mirror and the piezo linear stage sit on on a picomotor actuated linear stage with a range of  $\sim 2.5$  cm, which is used to adjust the NIR/VIS beam path length to the XUV beam path length upon each new alignment of the interferometer. Before recombination with the XUV beam, the intensity of the NIR in the experimental interaction region can be controlled either via a variable aperture (A2) for the experiment or with different neutral density filters mounted on a filter wheel for diagnostic purposes. The NIR/VIS power can be monitored with a calibrated photodiode (D1) via a flip mirror that can be inserted into the beampath after the aperture A2.

Both beams are recombined at a second perforated mirror (PM2) with a 1.5 mm  $\varnothing$  hole through which the XUV beam is transmitted so that the NIR/VIS and the XUV beam are collinear again.

### 4.1.2 Simultaneous attosecond streaking and transient absorption spectroscopy

At the exit of C2, the slightly divergent collinear NIR/VIS and XUV beams are focused with a toroidal mirror (TM) at the position of the experimental interaction region in the experimental chamber C3. The toroidal mirror (Zeiss) is coated with nickel and its curvature is optimized for an angle of incidence of  $86^\circ$  and a NIR/VIS beam diameter of up to 12 mm resulting in an effective focal length of 720 mm [21]. Due to the divergence of the beams the focus is at a distance 980 mm from the toroidal mirror. The beam waist ( $1/e^2$ ) of the NIR/VIS and XUV beam are  $105 \mu\text{m}$  and  $34 \mu\text{m}$ , respectively. Thus the XUV beam probes only close to the optical axis of the NIR/VIS beam to minimize transverse intensity variations in the probe volume.

For alignment of the spatial and temporal overlap between the two arms of the interferometer, the focus is imaged with a magnification of 2:1 onto a charge-coupled-device camera outside of the experimental chamber C3, labeled VIS CCD. At the temporal overlap the constructive interference of the residual NIR/VIS pulses that pass through the XUV arm without metal filters with a small portion of the NIR/VIS through the second arm (reduced in intensity with A2) can be observed. The spatial overlap at the focus is aligned by overlapping the NIR/VIS beam that has been attenuated with appropriate neutral density filters with the residual NIR/VIS pulses through the XUV arm without metal filters.

The streaking gas target is placed close to the focus in the experimental chamber. It consists of a gas nozzle with a  $\sim 50 \mu\text{m}$  opening that has been fabricated from a glass tube by heating and tapering. It produces a dilute gas jet in vacuum when it is supplied with  $\sim 350\text{-}500$  mbar neon from the back. To prevent charging of the glass by unintended photoemission that would disturb the electron detection, it is painted with a conductive layer of carbon. An electron time-of-flight spectrometer (Stefan Kaesdorf, Geräte für Forschung und Industrie, indicated by the black circle in C3) is used to detect photoelectrons emitted from Ne  $2p$  states via direct photoemission by the attosecond XUV pulses along the polarization axis of the NIR/VIS pulses (perpendicular to the sketch plane in Fig. 4.1). Streaking spectrograms (see chapter 1.4.2) can be recorded with the variable time-delay between the attosecond pulse and the NIR/VIS pulse introduced with the PZT.

A thin film transmission sample (e.g.  $125 \text{ nm SiO}_2$ ) can be placed closely behind the gas nozzle. The sample is placed within the confocal parameter of the NIR/VIS beam of several cm. The XUV beam that passes through the sample in the central region of the NIR beam is then transmitted through a  $0.2 \text{ mm}$  wide slit onto a toroidal flat-field diffraction grating (grating 541 00 220, Horiba Scientific). The slit can be adjusted transversely to the beam to optimize the XUV flux. The grating disperses the XUV spectrally on a XUV sensitive charge-coupled-device camera (XUV CCD2, PIXIS XO, Roper Scientific) and provides in this configuration a spectral resolution of  $\sim 0.35 \text{ eV}$  around  $100 \text{ eV}$ . Residual NIR/VIS light is blocked by two  $500 \text{ nm}$  Zr filters (not shown in the figure).

#### 4.1 Experimental setup for broadband attosecond probe spectroscopy

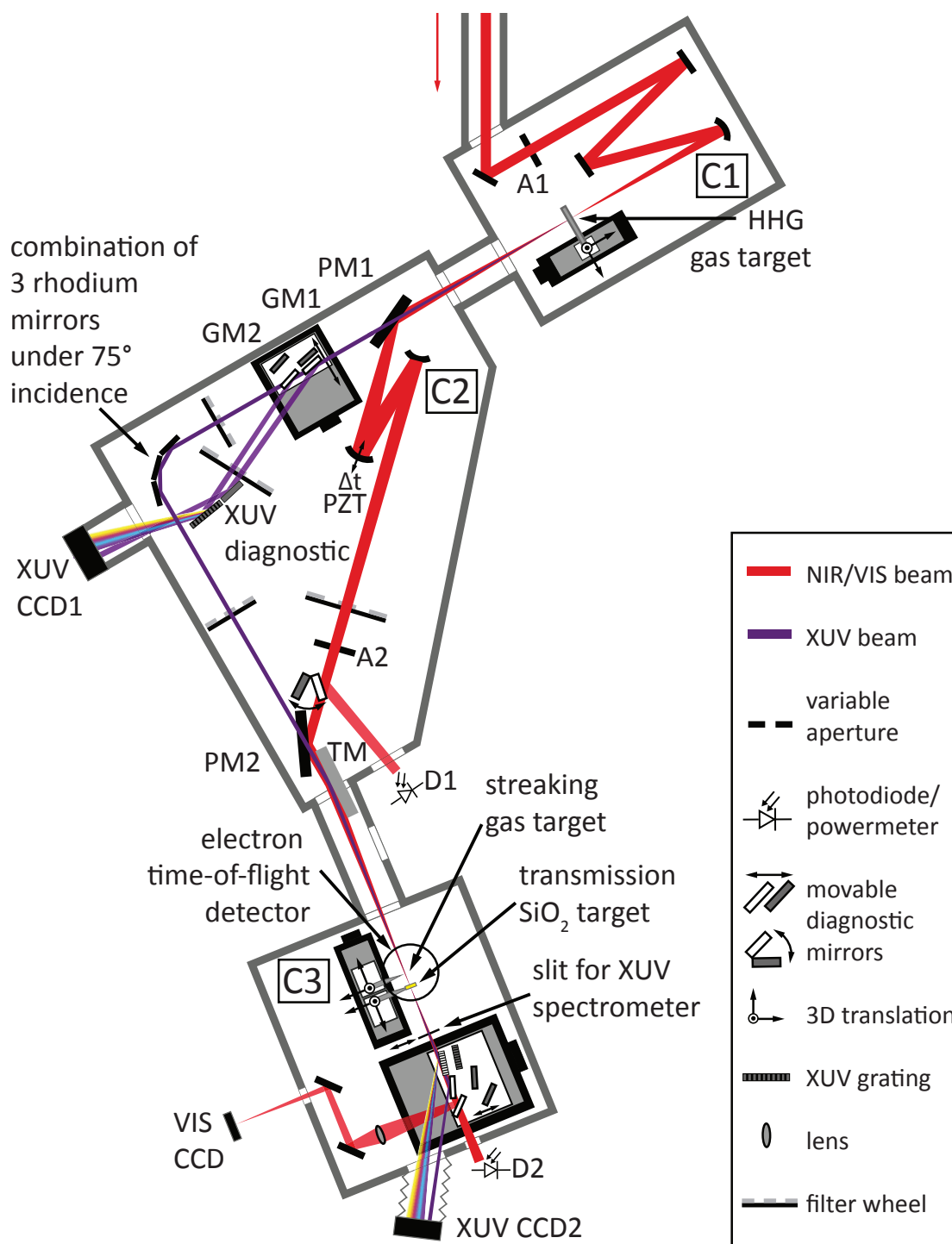


**Figure 4.1:** Experimental setup for broadband attosecond probe spectroscopy, residing in three vacuum chambers C1, C2 and C3. In C1 the XUV attosecond pulses are generated from few-cycle NIR/VIS pulses in a Ne filled gas target. C2 houses the XUV-NIR interferometer, where the NIR/VIS beam is split from and later recombined with the XUV beam by means of two perforated mirrors (PM1 and PM2). The experimental chamber C3 is equipped with an electron time-of-flight spectrometer and a gas nozzle for attosecond streaking spectroscopy and a home-built XUV spectrometer with entrance slit, a XUV flat-field grating and a XUV sensitive charge-coupled device camera (XUV CCD2). For further details refer to the text and the legend.

The data acquisition is computer-controlled with a program developed in Labview (National Instruments) by Markus Fiess and Simon Holzner, that controls the position of the PZT and therefore the temporal delay between the XUV and NIR/VIS pulses in the two arms of the interferometer. As function of this delay, the data from the electron time-of-flight spectrometer in combination with a picosecond counting card (Fast Comtec) and the binned data from the XUV CCD2 are acquired in separate files. For each delay step between the XUV pulse and the NIR/VIS pulse the electron spectrum and the absorption spectrum are recorded. The spectrum transmitted through the sample is divided by a reference spectrum recorded without the sample before each scan. Both spectra are corrected for dark counts by subtraction of a background spectrum. As the HHG spectrum is extremely sensitive to intensity and CEP fluctuations of the NIR/VIS laser pulses, an algorithm compares the recorded transmission spectrum to a reference transmission spectrum recorded before each scan in a region outside of the region of interest for the experiment (e.g. far from the absorption edges). In case the difference exceeds a predefined value that has to be established by several test recordings to minimize erroneous sorting, the data acquisition is repeated for this delay step.

### 4.1.3 Detection of optical breakdown in nanometric SiO<sub>2</sub> films

In the attosecond transient absorption experiment the dielectric breakdown of 125 nm thin SiO<sub>2</sub> films has to be detected in order to adjust the NIR/VIS intensity to the maximum value that can safely be applied. In the setup, two different methods can be used. The first consists of monitoring the NIR/VIS beam transmitted through the sample at the focus via the imaging system used for alignment of the spatial and temporal overlap on the VIS CCD in Fig. 4.1. The magnified image of the focus shows a well resolved beam profile. A sharp image of the frame that holds the thin film as can be seen in Fig. 4.2 **a** ensures proper alignment of the camera to the image plane. Upon breakdown the material transmission changes abruptly and shows clear diffraction rings from the damaged spot that appears in the high intensity region in the center of the beam profile, see Fig. 4.2 **b**.

It is important to note that the optical breakdown is well confined to the high intensity region of the NIR/VIS laser beam which is sampled by the much smaller XUV beam at the waist position of both beams. This fact also ensures that the XUV beam probes the material experiencing the highest field strength. The breakdown field strength for the 125 nm thin SiO<sub>2</sub> films was  $\sim 2.6 \pm 0.5$  V/Å, corresponding to a threshold intensity of  $\sim 10^{14}$  W/cm<sup>2</sup>.

For the second method the characteristic spectral absorption edge of SiO<sub>2</sub> at 109 eV is observed on the XUV CCD2. At dielectric breakdown the (micro-) crystalline order of the material vanishes and so does the band structure responsible for the characteristic absorption. The overall absorption in the XUV decreases and the characteristic absorption edge completely disappears, see Fig. 4.3 where the solid blue line is the optical density of the intact sample and the dashed red line corresponds to a sample spot that has experienced optical breakdown.



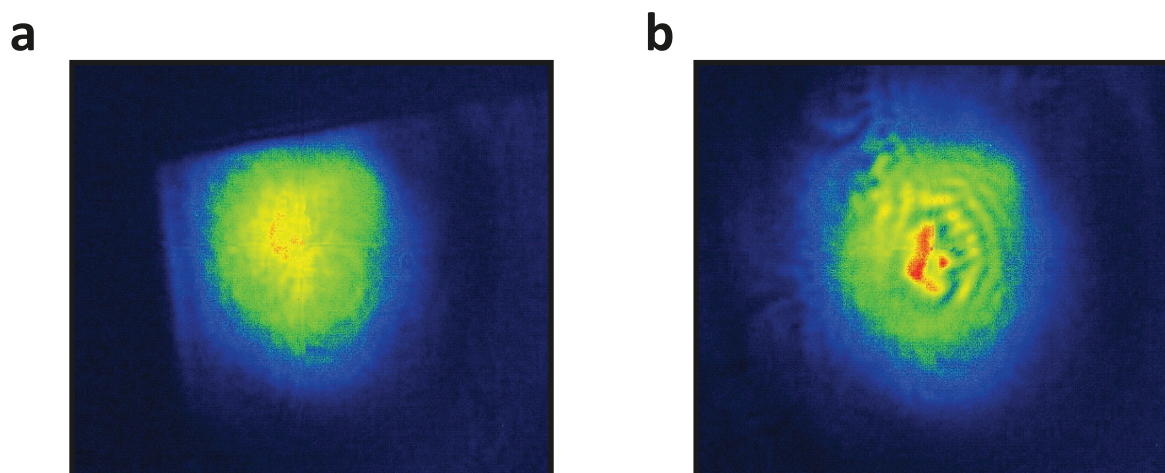


**Figure 4.2:** Optical damage detection via a magnified image of the NIR/VIS focus at the position of the thin SiO<sub>2</sub> film on a CCD camera. (a) At an intact position on the sample, the transmitted beamprofile is clean and structureless. (b) After optical breakdown the transmitted beam profile shows diffraction from the damaged spot.

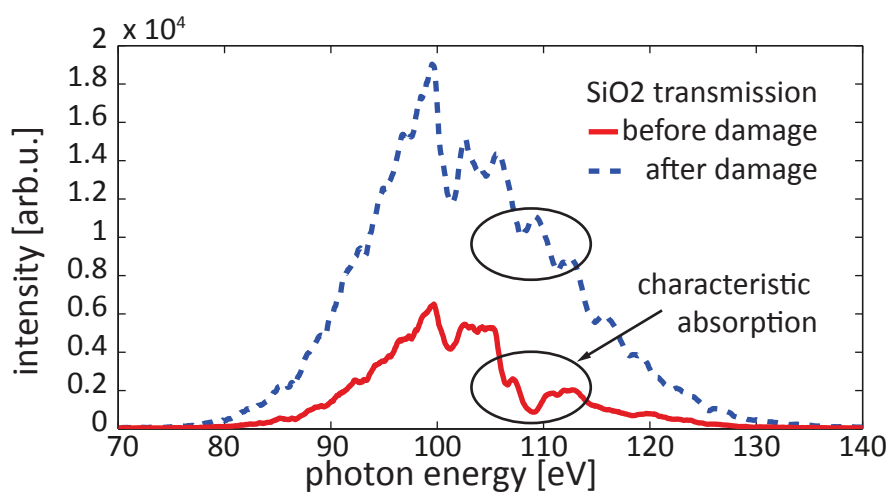


**Figure 4.3:** Damage detection via characteristic XUV absorption. The XUV optical density at the characteristic absorption edge at 109 eV, marked by the black circle, is a clear indicator of optical breakdown. The two spectra depict the SiO<sub>2</sub> transmission before (solid red line) and after (dashed blue line) optical breakdown induced by the intense NIR/VIS pulse. The strong overall increase in transmission is most likely due to the fact that the optical breakdown is accompanied by ablation of material from the nanofilm in the center of the beam.

## 4.2 Attosecond transient absorption of SiO<sub>2</sub> in combination with attosecond streaking

In the attosecond transient absorption experiment few-cycle NIR/VIS pulses allow damage-free exposure of a 125 nm thin film of fused SiO<sub>2</sub> to fields of  $2.3 \pm 0.5$  V/Å. At this timescale and at such high field strengths close or even beyond the critical field strength  $F_{crit}$  the system becomes highly polarizable and responds adiabatically to the incident field. The field-induced polarization modifies the joint density of states of the L-edge transition in SiO<sub>2</sub>, which can be probed with attosecond temporal resolution as presented in the following experiment. With this approach it became possible to probe the polarization dynamics *inside* a bulk dielectric with sub-100 as temporal resolution.

Broadband attosecond absorption spectroscopy can probe the Si *2p* to conduction band transition in the presence of a strong NIR/VIS field. Isolated attosecond XUV pulses of only 72 as duration, corresponding to over 30 eV spectral bandwidth at a central energy of 105 eV are transmitted through 125-nm free-standing chemical vapor-deposited films of fused silica. The characteristic XUV optical density (OD) around the L-absorption edge of the sample is shown in Fig. 4.4 **b**. Three distinctive regions in the absorptivity labeled **A**, **B** and **C** are marked in the figure. At the spectral onset of the Si L<sub>2,3</sub> absorption, the first relative peak (**A**), is attributed to absorption into an excitonic state with an anomalously high binding energy of 3 eV below the conduction band minimum (cf. X-ray near-edge absorption spectroscopy (XANES) [164] and electron energy loss spectra (EELS) in [165, 92]) involving transitions from the Si *2p* core states to Si *3s*-like states.

The unperturbed conduction band, extending from **B** beyond **C** in Fig. 4.4, of fused silica contains a mixture of states originating from the Si *3p* and Si *3d* orbitals [165]. The characteristic above-edge absorption strength reflects the local density of states in the conduction band. The conduction band extends over more than 10 eV spectral bandwidth  $\Delta_{CB}$  which is fully covered by the bandwidth of the employed attosecond pulses. The XUV pulses consequently induce polarization across the full available bandwidth which dephases within its spectral response time defined by  $\tau_{dp} \sim \hbar/\Delta_{CB} \approx 100$  as. This fast decay of coherence between XUV light radiated coherently from the induced polarization in the sample and the transmitted XUV pulses is the key to observe the quantum system under investigation *at the instant of probing* without any influence of the NIR/VIS excitation field at times later than the XUV pulse duration which complicates the interpretation of comparably narrow band atomic excitations during the temporal overlap of pump and probe pulses [166] as for example in the first attosecond transient absorption experiment in krypton [34, 159].

## 4.2 Attosecond transient absorption of SiO<sub>2</sub> in combination with attosecond streaking

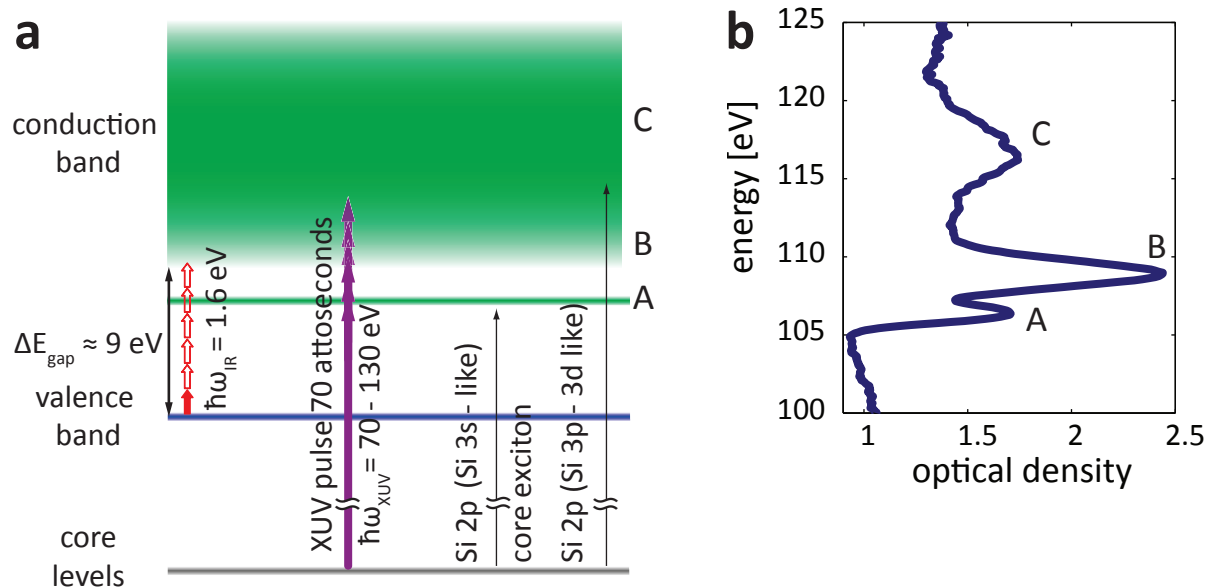


**Figure 4.4:** (a) Schematic energy level diagram of Si 2*p* core states and valence and conduction band states in SiO<sub>2</sub>. Purple arrows indicate resonant core-level absorption of the XUV spectrum of the attosecond pulse. The red arrows indicate the non-resonant photon energy of the NIR/VIS pulses employed as pump pulses. (b) Optical density of a 125 nm thin SiO<sub>2</sub> film near the L-edge transition measured with a broadband attosecond pulse. According to the references [164] and [165, 92] the first peak, labeled **A**, at the spectral onset of the Si L<sub>23</sub> absorption involves transitions from the Si 2*p* core states to Si 3*s*-like states formed by an excitonic resonance evoked by the modification of the conduction band states in the presence of the core-hole. The region **B** marks the absorption into states at the conduction band minimum containing a mixture of Si 3*p* and Si 3*s*-like states and **C** the higher lying states in the conduction band.

### 4.2.1 Attosecond streaking of broadband XUV pulses

The combination of the transmission sample and the streaking gas target within a small fraction of the confocal parameter (see chapter 4.1.2) permits to acquire transient absorption spectra and an attosecond streaking spectrogram in parallel. This important development allows to establish a direct link between the incident NIR/VIS electric field and the dynamics observed in the time-resolved absorption trace. Fig. 4.5 **a** shows the broadband attosecond streaking trace and the XUV pulse envelope and phase (**b**) retrieved with a FROG-algorithm for attosecond streaking spectrograms [74]. The retrieved pulse duration of the attosecond pulse is 72 as. The few-cycle NIR/VIS pulse reaches a maximum field strength of  $2.3 \pm 0.5 \text{ V/\AA}$ . While the attosecond pulse duration and the NIR/VIS waveform can be extracted reliably from such a broadband streaking spectrogram with high NIR/VIS field strength, the maximum field strength is underestimated due to the limited transmission bandwidth of the electrostatic lens of the time-of-flight electron spectrometer. The maximum field strength has been evaluated in a consecutive streaking spectrogram with a slightly less broadband XUV pulse spectrum. The bandwidth can be easily changed by using a 150 nm palladium filter with transmission of the XUV spectrum above  $\sim 115 \text{ eV}$  instead of the 150 nm molybdenum filter that is used for the very broad XUV bandwidth in the absorption experiment.

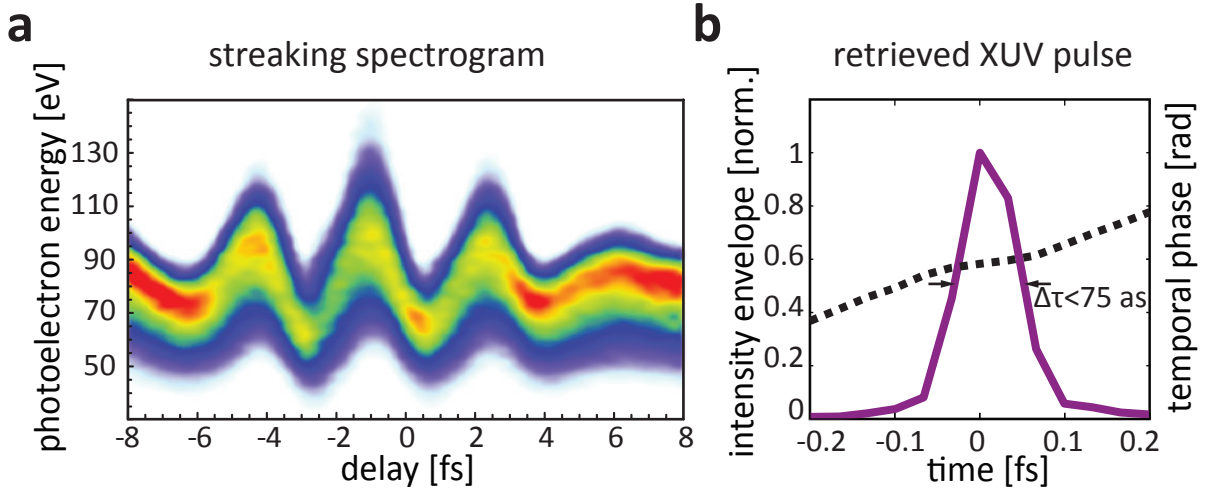


**Figure 4.5:** (a) Attosecond streaking spectrogram of broadband ( $\Delta\hbar\omega_{XUV} > 30$  eV) attosecond pulses. (b) FROG-retrieval of the attosecond pulse intensity envelope and phase, corresponding to a sub-75 as XUV pulse.

### 4.2.2 Transient absorption of nanometric SiO<sub>2</sub> films

Figure 4.6 shows a transient absorption spectrogram of 125 nm SiO<sub>2</sub> in the spectral range of 105 eV to 120 eV recorded in time-delay steps of 100 as. The NIR/VIS field strength, evaluated from the streaking spectrogram, exceeded 2 V/Å. A dynamic modification of the XUV optical density as shown in the figure could only be observed at field strengths close (within  $\sim 10\%$ ) to the experimentally observed damage threshold of  $\sim 2.6 \pm 0.5$  V/Å. At the temporal overlap a decrease in the optical density of the material can be observed in a large spectral range at and above the conduction band minimum.

First, the optical density of the pronounced peak **B** at the conduction band minimum at 109 eV is evaluated as the average of a 1 eV wide window divided in 15 segments. The optical density is shown in Fig. 4.7 **a** together with the electric field of the incident NIR/VIS laser pulse Fig. 4.7 **b** that has been recorded simultaneously by attosecond streaking. The error bars correspond to the standard error of the average value. The optical density is modulated at twice the laser frequency - a clear evidence for a field sensitive effect. Not only the optical density but also the energy of the absorption band changes under the influence of the strong NIR/VIS field. The absorption peak at 109 eV is approximated with a Gaussian function parametrized by its height, width and central position and evaluated with a nonlinear fitting routine. Fig. 4.8 shows an overall shift of the peak position towards lower energies which is also modulated at twice the laser frequency. The modulation depth and strength of both the optical density and the absorption band position at twice the optical frequency are indicative of the fast polarization response of the material to the external field.

## 4.2 Attosecond transient absorption of SiO<sub>2</sub> in combination with attosecond streaking

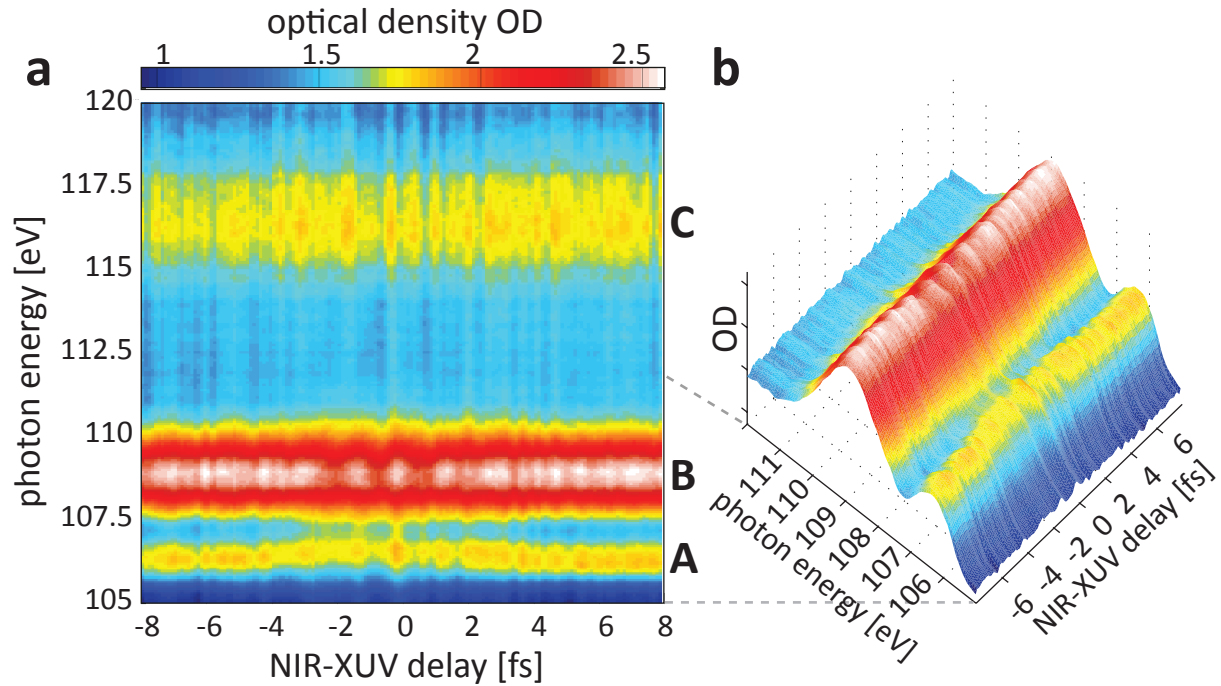


**Figure 4.6:** (a) Sequence of XUV absorption spectra (absorption spectrogram) of a 125 nm thin SiO<sub>2</sub> film in the range of 105 eV to 120 eV recorded in function of the delay of the few-cycle NIR/VIS pulse with respect to the isolated attosecond XUV pulse in delay steps of  $\Delta t_d = 100$  as. The optical density is encoded in false colors. Negative delay times correspond to the XUV probe pulse preceding the NIR/VIS pulse. Panel (b) shows the spectrogram in the range of 105 eV to 112 eV in a three-dimensional view to highlight the delay dependent changes in optical density in the lines labeled **A** and **B** of the excitonic and the conduction band absorption as described in Fig. 4.4.

In addition to the modulation in the conduction band, also the transition from Si  $2p$  states into excitonic states at 106 eV situated below the conduction band minimum is strongly affected by the presence of the NIR/VIS field. Fig. 4.9 shows the strong absorption bleaching of several percent in OD at this energy evaluated similarly to the absorption feature at 109 eV, but in a 0.5 eV bandwidth centered at 106.25 eV. Yet even more remarkable is the spectral shift of the peak absorption towards higher energies. The final state in which the XUV photons are absorbed in this case is situated in the band gap of the material and arises from the formation of a strongly bound core exciton according to [164] and [165, 92]. The absolute shift of the absorption peak amounts to more than 100 meV as shown in Fig. 4.10, indicating a high polarizability of the state as one would expect from a bound electron-hole pair. The binding energy of the excitonic states is reduced in the presence of the strong NIR/VIS field, so a shift towards the CB minimum occurs.

The transient absorption bleaching of the Si  $L_{2,3}$  edge is most pronounced at the minimum of the conduction band, but a weaker decrease of the optical density at the overlap can also be observed for higher photon energies of 112 eV to 115 eV covering almost the whole conduction band width in the region labeled **C**. The modulation is revealed in a difference-spectrogram where the mean of 5 spectra before the temporal overlap of the NIR/VIS and XUV pulse is subtracted from the spectrogram, see Fig. 4.11. This difference-spectrogram also shows regions of increased optical density, mainly at 107 eV, where the excitonic absorption peak is shifted to higher energies. But

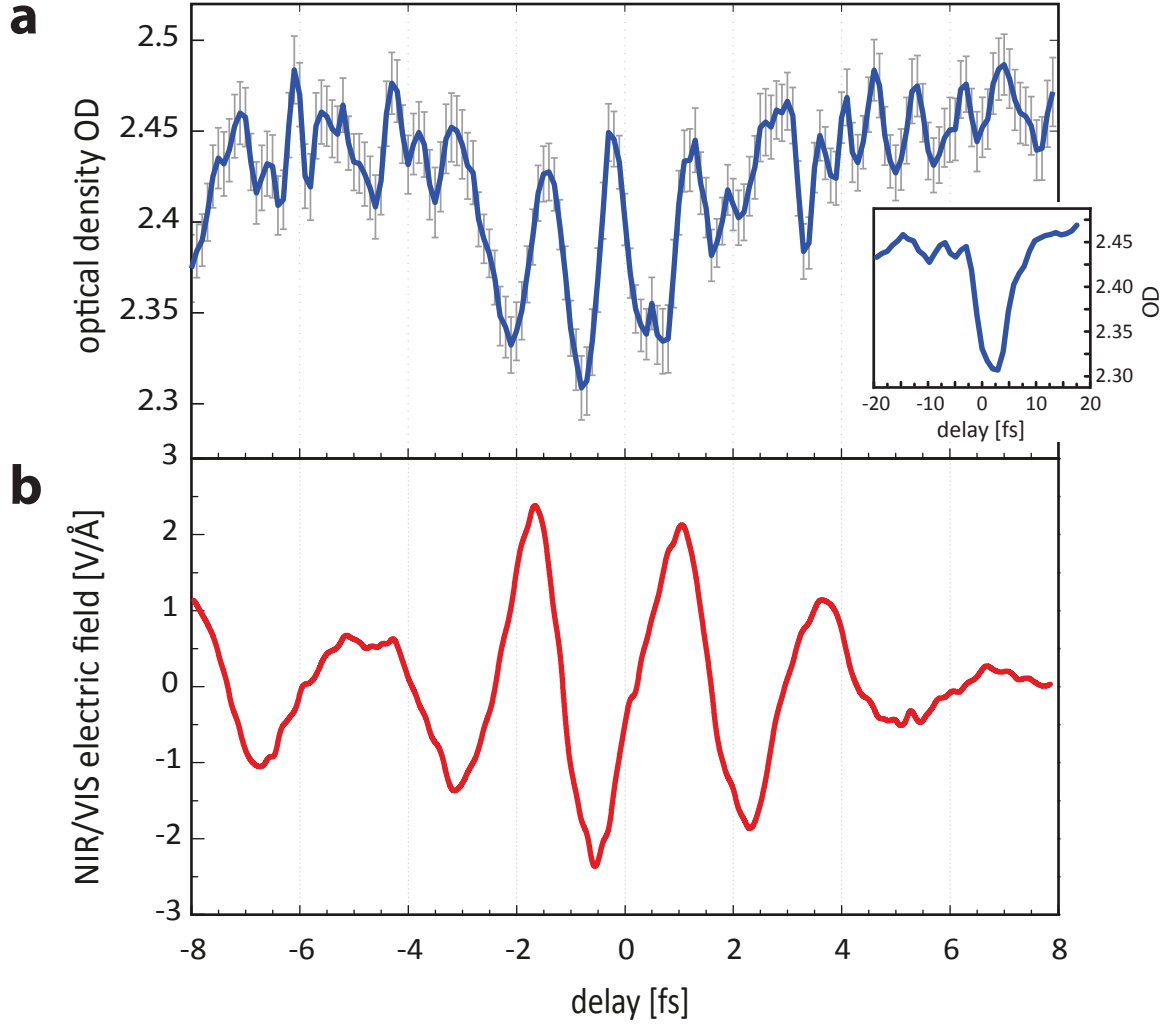


**Figure 4.7:** (a) Time-resolved XUV optical density of the conduction band minimum of fused silica evaluated as average of 15 pixels in a 1 eV wide band centered at 109 eV under the influence of a strong few-cycle NIR/VIS laser field, shown in panel (b). The error bars in panel (a) correspond to the standard error of the average value. The inset in panel a shows the XUV optical density at 109 eV over an extended delay range in coarse delay steps.

also within the CB region above 110 eV a slight increase on optical density is observed. While the dynamics in the individual spectral regions around the Si L-edge transition differ in their complexity and sensitivity to the driving field, they have one important feature in common: The modification of the absorption strength only occurs during the overlap of the attosecond probe pulse with the NIR/VIS laser pulse as can be seen in the inset in Fig. 4.7 a. It shows the evolution of the optical density at 109 eV over an extended delay range in coarse delay steps. Apparently the interaction with the pump pulse does not entail the occurrence of long-lived coherences or population in an excited state of the material that would alter the XUV optical density for times longer than the NIR/VIS pulse duration. This suggests that the effect of the strong field on the dielectric is largely reversible and due to a purely electronic polarization response.



## 4.2 Attosecond transient absorption of SiO<sub>2</sub> in combination with attosecond streaking

---

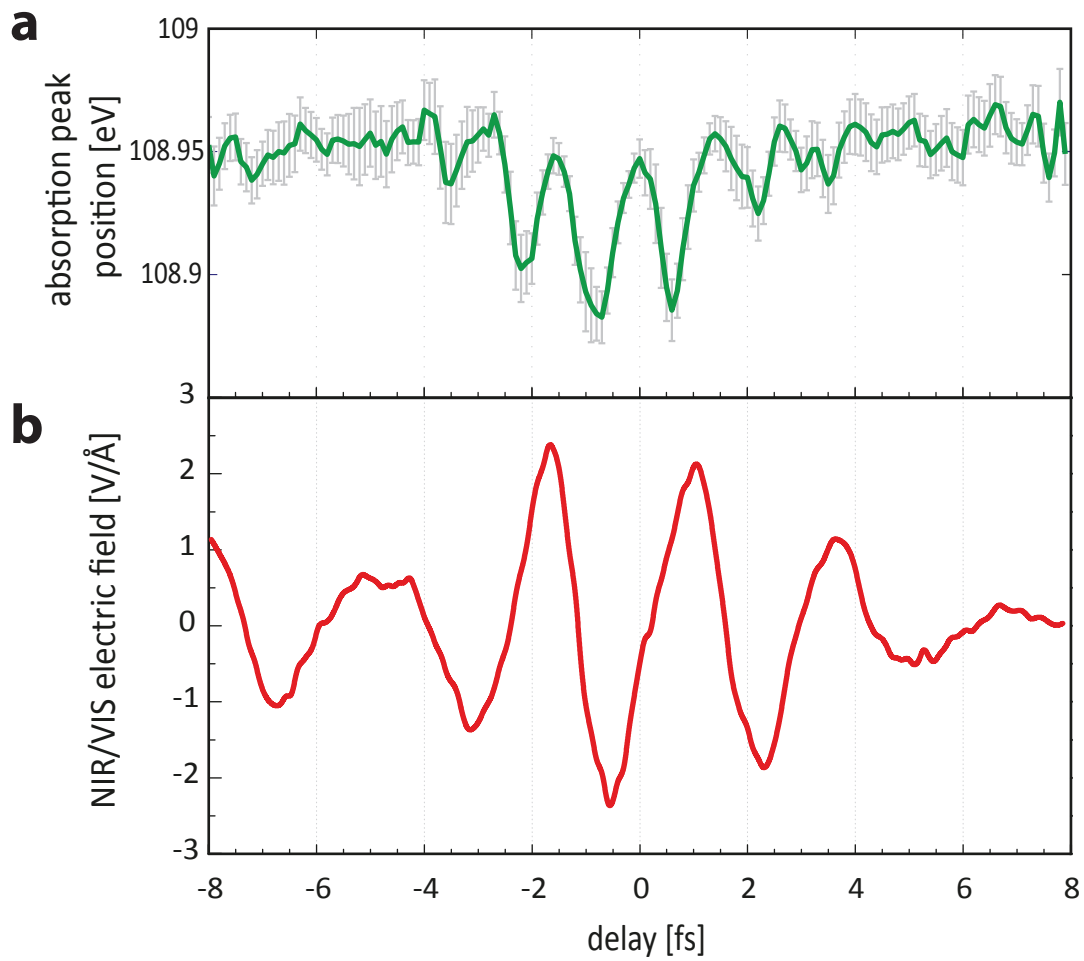


**Figure 4.8:** (a) Time-resolved spectral position of the absorption peak at the conduction band minimum at 109 eV evaluated with a nonlinear fit algorithm. The error bars correspond to the 95% confidence interval of the fit. (b) Electric field of the NIR/VIS laser pulse in function of the XUV-NIR/VIS delay-time recorded simultaneously to the transient absorption spectra.

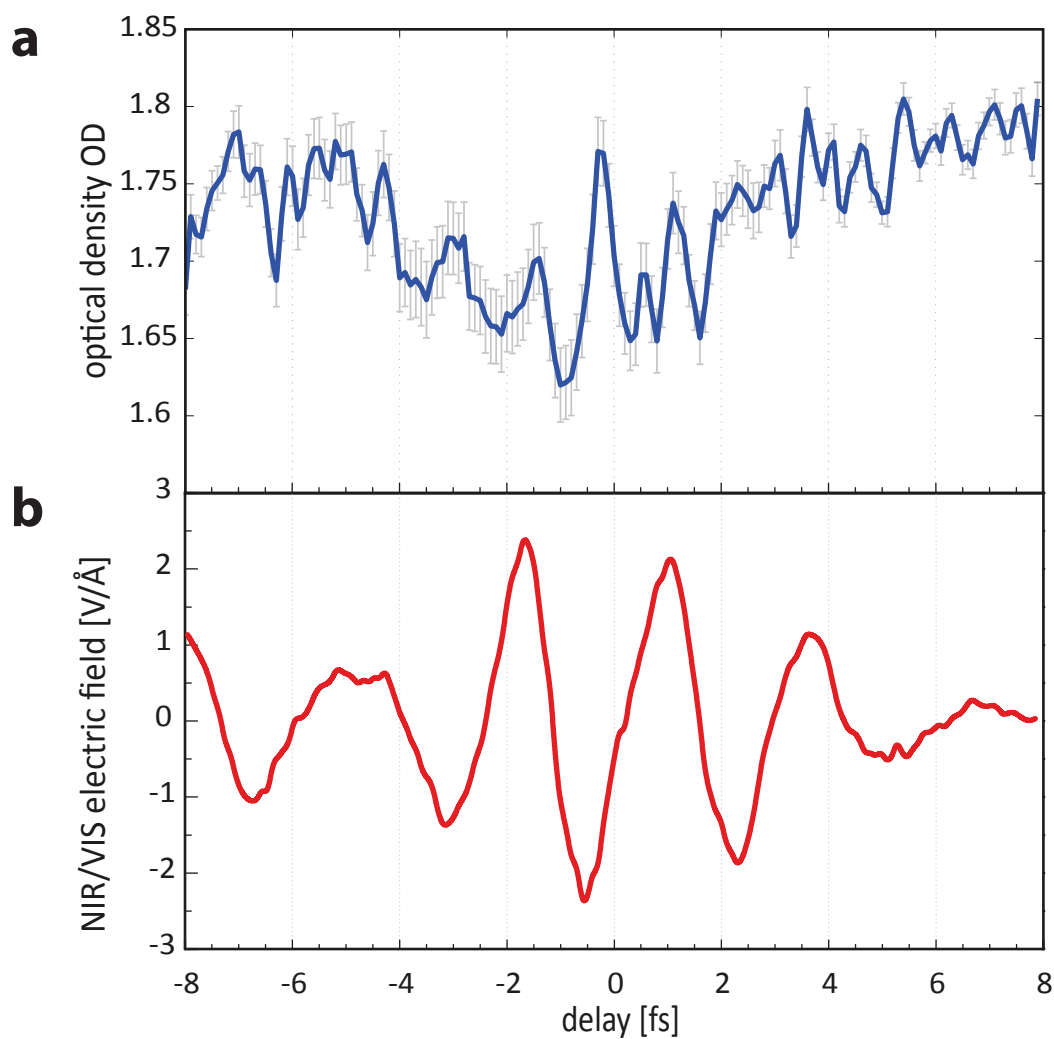


**Figure 4.9:** Time-resolved XUV optical density of the absorption feature which is attributed to the formation of a core-exciton. The optical density is evaluated as average of 15 pixels in a 0.5 eV wide band centered at 106.25 eV (a) under the influence of a strong few-cycle NIR/VIS laser field (b). The error bars in panel a correspond to the standard error of the average value. The origin of this absorption peak and its dynamics are discussed in more detail in chapter 4.3.1.



## 4.2 Attosecond transient absorption of SiO<sub>2</sub> in combination with attosecond streaking

---

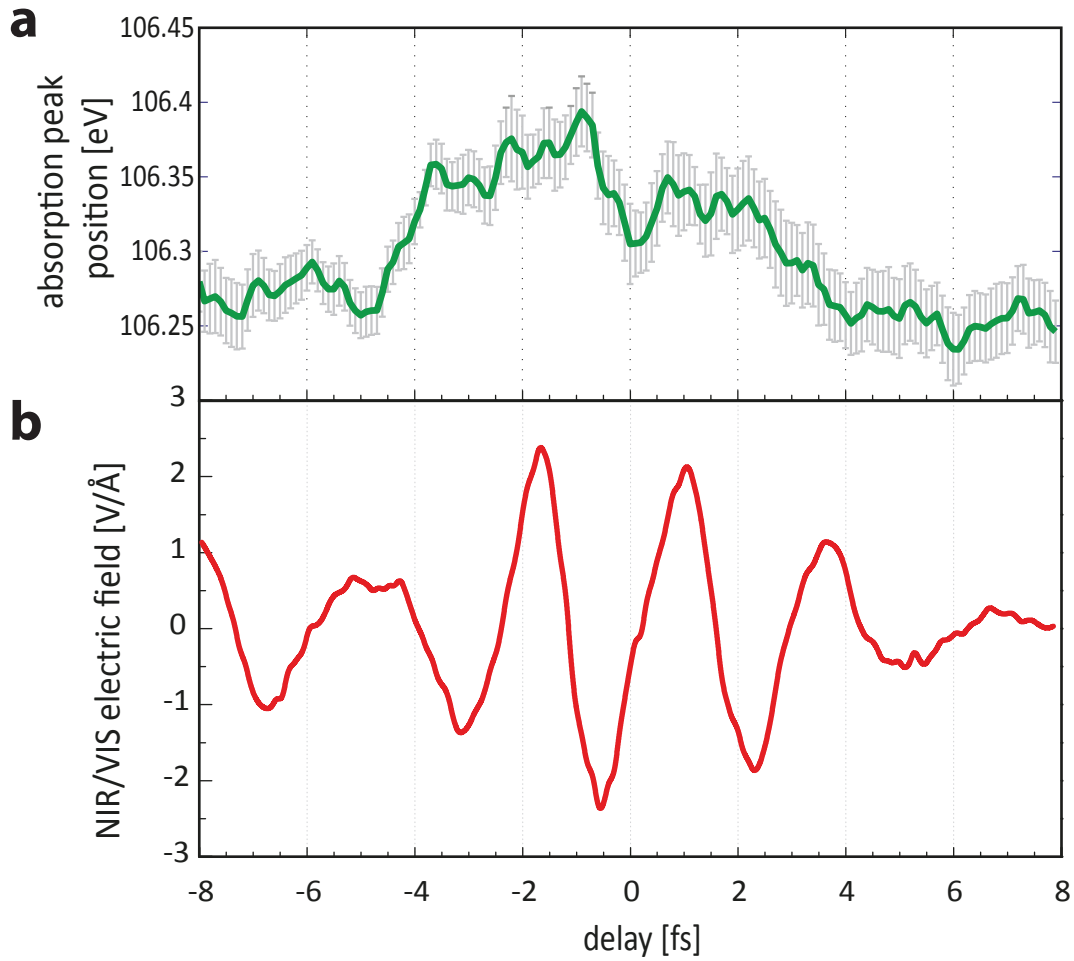


**Figure 4.10:** (a) Time-resolved energy of the excitonic absorption peak at 106.25 eV evaluated by nonlinear peak fitting. The error bars correspond to the 95% confidence interval of the fit. The shift of more than 100 meV under the influence of the strong NIR/VIS field is remarkable and indicates a strong polarizability of the final electronic state, which is situated in the energy band gap of the material. (b) Electric field of the NIR/VIS laser pulse in function of the XUV-NIR/VIS delay-time recorded simultaneously with the transient absorption spectra.

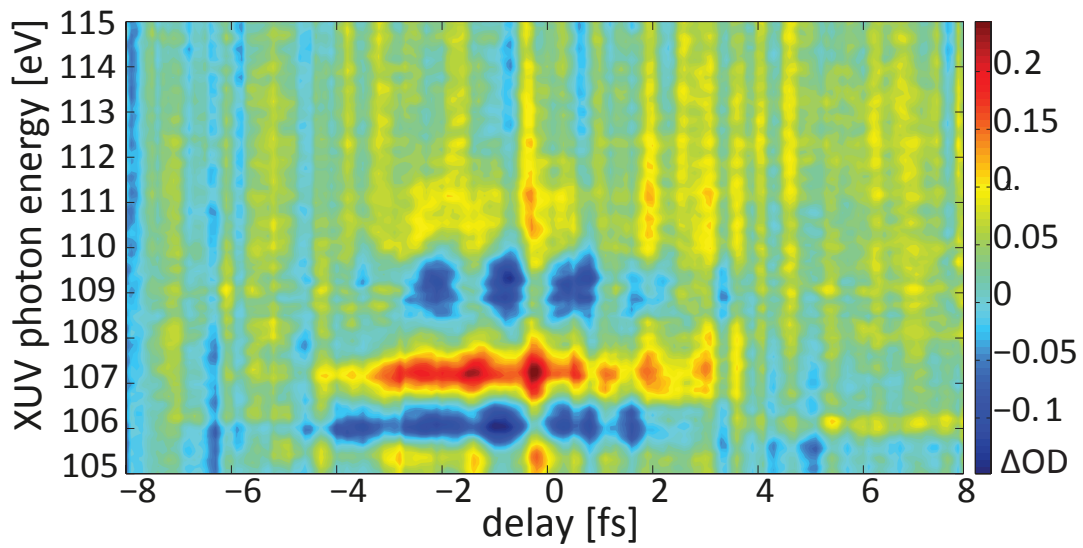


**Figure 4.11:** A broadband modulation of the absorption in the temporal overlap up to energies of 115 eV can be seen in the difference spectrogram, where an average background spectrum before the temporal overlap has been subtracted from each spectrum.

## 4.3 Theory of attosecond transient absorption in SiO<sub>2</sub>

In order to interpret the experimental findings presented in the previous section, the attosecond transient absorption experiment has to be put into a theoretical framework in view of the underlying dynamics of the electronic states in presence of the strong NIR/VIS pump field. Under the present experimental conditions the attosecond XUV pulse is considered as a weak probe that promotes electrons from strongly bound Si 2*p* states into the empty conduction band via a one photon absorption process as indicated by the purple arrows in Fig. 4.4 **a**. Owing to the large spectral bandwidth of the attosecond pulses, transitions covering the large conduction band width  $\Delta_{CB} \sim 10$  eV are possible. The NIR/VIS pump photon spectrum of  $\sim 1.2$ - $2.2$  eV (indicated by the red arrow at the valence band) is non-resonant relative to the smallest direct bandgap of  $\Delta_{gap} \sim 9$  eV of the unperturbed material.

### 4.3.1 Modification of excitonic resonances in the absorption spectrum

Below and near the conduction band minimum the XUV Si-L<sub>2,3</sub>-edge absorption shows a pronounced absorption feature (labeled **A** in Fig. 4.4) attributed to an excitonic resonance that occurs in the presence of a core hole [165]. The XUV absorption strength as well as the spectral position of the peak are modified during the overlap with the NIR/VIS laser pulse, cf. Fig. 4.9 and Fig. 4.10. Considering a perturbative approach to pump-probe nonlinear absorption spectroscopy similar to [166, 17], the NIR/VIS pump field would be able to, for example, couple transitions between this state and higher lying conduction band states [167]. This coupling between final states would lead to a change in the transition matrix elements between the core state and the final states and hence modify the imaginary part of the complex refractive index experienced by the XUV radiation in this spectral range. While this model, proposed by Nicholas Karpowicz in private communication, might partially explain the observed absorption bleaching and spectral shift of the absorption feature **A** and the pronounced conduction band edge absorption **B**, there remain open questions regarding the intensity scaling of the induced absorption as well as the applicability of such a perturbative approach at field strengths of more than  $2 \text{ V/\AA}$  as in the present experiment. Further theoretical developments are under way to establish a non-perturbative description of the effects that lead to the strong AC-Stark-shift and the absorption bleaching in the excitonic absorption line **A**.

### 4.3.2 Quantum-mechanical model of valence band and conduction band dynamics

The experimental field strengths approach the critical field strength  $F_{crit}$  which is defined as the field required to change the potential energy of an electron over the distance of the lattice period  $a \sim 5 \text{ \AA}$  enough to overcome the fundamental bandgap  $\Delta_{gap}$  (Eq. 2.25). In fused silica this

corresponds to a field strength of

$$F_{crit} = \frac{\Delta_{gap}}{|e|a} \sim 2V/\text{\AA}. \quad (4.1)$$

Such high fields require theoretical modeling beyond the realm of well-established perturbative descriptions of light-matter interaction [168]. The theoretical model described in the following was developed by Vadym Apalkov and Mark I. Stockman from Georgia State University. In addition to the transient XUV absorption bleaching presented here, the model could also reproduce the experimental evidence for strong-field-induced conductivity in Schiffrin et al. [1]. More details can be found in the supplementary material of both papers [64, 1] and in a separate publication on the theory [90]. In the scope of this thesis their general approach shall be presented along with their specific findings modeling the conditions of the transient absorption experiment in order to provide further interpretation of the transient bleaching of the absorption from core-level states into conduction band states.

The time-evolution of the quantum states of the system under the influence of a strong electric field  $\mathbf{F}(t)$  is described by the Hamiltonian  $\hat{H}(t)$

$$\hat{H}(t) = \hat{H}_0 + \hat{H}_1(t), \quad (4.2)$$

where  $\hat{H}_0$  is the Hamiltonian of the unperturbed system and  $\hat{H}_1(t)$  describes the interaction with the electric field  $\mathbf{F}(t)$ ,  $\hat{H}_1(t) = -e\hat{\mathbf{r}}\mathbf{F}(t)$ . Considering the time-dependent Schrödinger equation

$$i\hbar \frac{\partial}{\partial t} |n, t\rangle = \hat{H} |n, t\rangle \quad (4.3)$$

in the direction of the linearly-polarized field and a periodicity with a lattice constant  $a=5\text{\AA}$ , the problem is treated in one dimension in the tight-binding approximation. The model incorporates field screening but interactions between electrons such as electron collisions are neglected as well as excitonic effects arising from Coulomb interaction of conduction band electrons with core-holes created by absorption of XUV photons. The model Hamiltonian takes into account  $N_c$  lattice sites numbered by index  $l$  and both the valence band and the conduction band are each composed of two sub-bands,  $n = v1, v2, c1, c2$ . The offset energies  $E_n$  and the respective bandwidths of the bands are chosen to fit the properties of fused silica in the unperturbed case:

sub-band	$E_n$	$\Delta_n$
v2	-12.5 eV	1 eV
v1	-11.25 eV	0.5 eV
c1	0 eV	4 eV
c2	4.4 eV	3.8 eV

The unperturbed Hamiltonian with eigenfunctions that satisfy the Bloch theorem consists of the sum of standard tight-binding Hamiltonians for each band that are taken within the nearest-

neighbor approximation using the creation and annihilation operators for an electron in band  $n$  on the lattice site  $l$   $c_{n,l}$  and  $c_{n,l}^+$ :

$$\hat{H}_0 = \sum_n \sum_{l=1}^{N_c} \left[ E_n c_{n,l}^+ c_{n,l} + \frac{\Delta_n}{4} (c_{n,l}^+ c_{n,l} + c_{n,l} c_{n,l}^+) \right], \quad (4.4)$$

The time-dependent part of the Hamiltonian  $\hat{H}_1(t)$  introduces a k-independent dipole coupling between the different bands which is characterized by coupling constants  $Z_{n,n'}$ :

$$\hat{H}_1(t) = -eF(t) \left( \sum_n \sum_{l=1}^{N_c} l a c_{n,l}^+ c_{n,l} + \sum_{n,n'} Z_{n,n'} \sum_{l=1}^{N_c} c_{n,l}^+ c_{n',l} \right) \quad (4.5)$$

The coupling constants or rather the corresponding dipole matrix elements  $d_{n,n'} = e \cdot Z_{n,n'} = e \cdot 2\text{\AA}$  describing the transitions between either the two conduction bands  $n, n' = c1, c2$  or valence bands  $n, n' = v1, v2$  govern the strength of the nonlinear interaction with the external field. The model reproduced the observations reported here with the same parameters that were used to model the strong-field induced conductivity in SiO<sub>2</sub> reported in [1]. The valence band to conduction band transition was modeled to correctly describe the linear absorption properties with  $Z_{v1,c1} = 3\text{\AA}$ .

The time-dependent Schrödinger equation (Eq. 4.2) is solved numerically within the basis set of the unperturbed eigenfunctions of  $\hat{H}_0$ . V. Apalkov and M. I. Stockman describe the dynamics of the system by its causal one-particle Green's function  $\hat{G}(t, t')$ . Considering the attosecond pulse  $F_p(t - \tau)$  as a weak probe, its absorption spectrum  $A_\omega(\tau)$  at a certain time delay  $\tau$  relative to the optical pulse  $F(t)$  is calculated perturbatively taking the trace of the function that describes the dipole interaction of the probe with the dynamically evolving system. The system is characterized by the retarded ( $\hat{G}^r$ ) and advanced ( $\hat{G}^a$ ) Green's functions as

$$A_\omega(\tau) = \frac{1}{4\pi\hbar^2} \text{Re} \left( \int_{-\infty}^{\infty} dt dt' \text{Tr} \left\{ \hat{G}^r(t, t') \hat{\mathbf{d}} \cdot \mathbf{F}_P(t' - \tau) \hat{G}^a(t', t) \hat{\mathbf{d}} \cdot \mathbf{F}_{P\omega} \right\} \right), \quad (4.6)$$

with  $F_{P\omega} = \int_{-\infty}^{\infty} e^{i\omega t} F_P dt$ . In order to obtain the transient optical density of the material, the Schrödinger equation and the Maxwell equation are solved in parallel by the finite difference time domain method. The two sets of equations are coupled via the dielectric polarization of the system  $P = \text{Tr} \left\{ \hat{\mathbf{d}} \hat{\rho}(t) \right\}$ , where  $\hat{\rho}$  is the density matrix of the system. The experimentally measured NIR/VIS field  $F(t)$  is used as an input for the self-consistent calculation.

## 4.4 Reversible sub-cycle dynamics of dielectric polarizability

The quantum-mechanical model is able to reproduce the main features of the experimental data both in the magnitude of the XUV absorption bleaching and in the AC-Stark-shift of the

absorption maximum. The spectral absorbance and energy position of the absorption peak at 109 eV are depicted in Fig. 4.12 **a** and **b**, respectively, along with the incident measured field, shown in panel **c**. Using the experimentally recorded electric field as an input, the measured and calculated dynamic modulation of the optical density agrees well in magnitude and also in its respective phase relative to the incident NIR/VIS field.

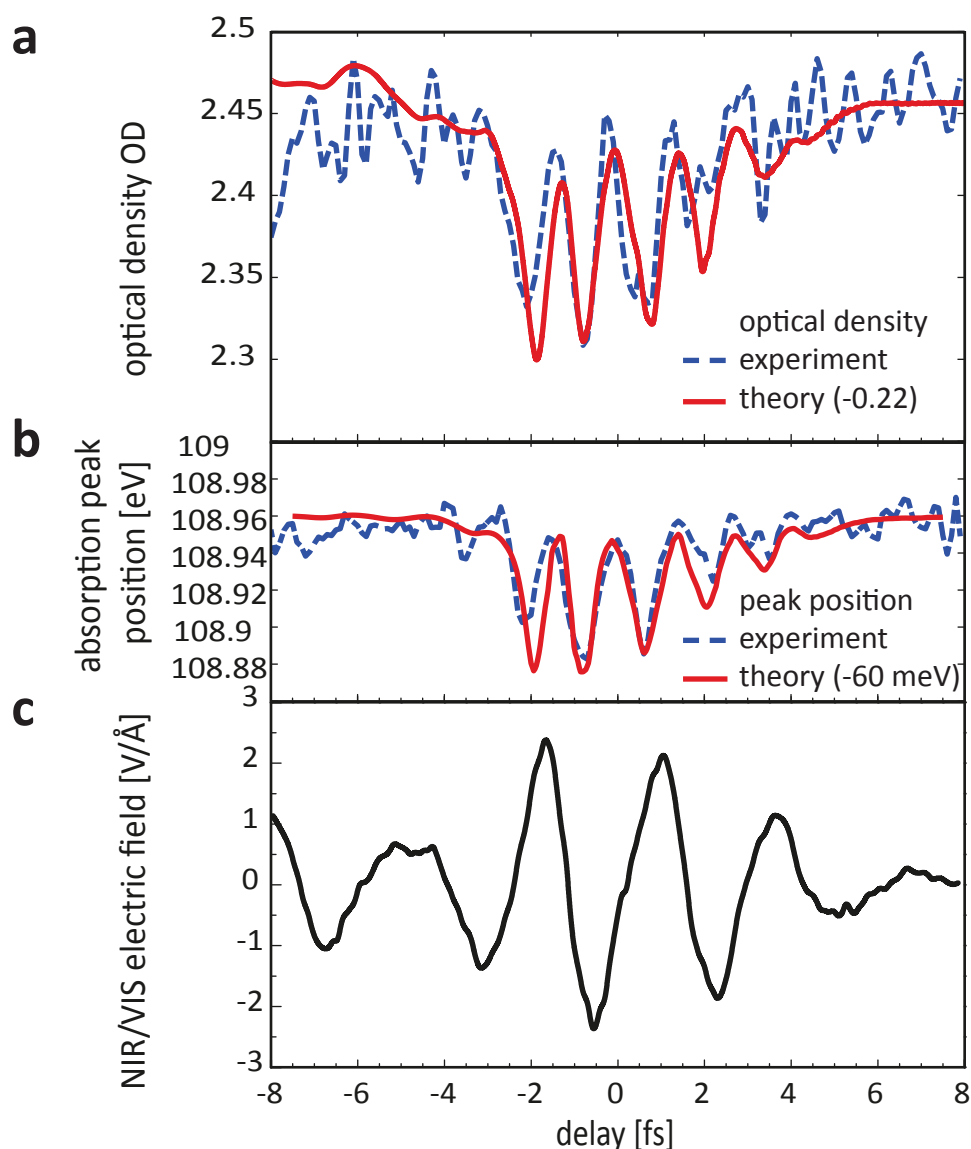


**Figure 4.12:** Panels **a** and **b** show the experimental (dashed blue line) and calculated (solid red line) optical density at 109 eV and the spectral shift of the absorption maximum, respectively. The theoretical results have been obtained by V. Apalkov and M. I. Stockman, using the experimental streaking field, shown in panel **c** as input. The qualitative agreement in modulation depth and relative phase to the incident field agree very well with the experiment. The theoretical results have been offset in the plot as stated in the legend to account for a small offset from the experimental results.

This global agreement supports the assumption that the instantaneous field inside the mate-

rial, which is the superposition of the incident field and the induced polarization, drives the underlying electron dynamics. The quantum-mechanical model permits to take a closer look at this. Fig. 4.13 shows how the local density of states (panel **a**), i.e. the density of conduction band states accessible at the position of the Si atom in the unit cell, and the conduction band population (panel **b**) are changed by the optical field (red solid line in panel **c**). This reduction in states available for the core-level excitation is responsible for the transient bleaching of the XUV optical density. The transient population of the conduction band is a sign of increased polarizability of the system [90], that is reversible at the sub-femtosecond time-scale, turned on and off within a fraction of the optical cycle. Panel **c** shows the calculated internal field inside the material (dashed line), which is the superposition of the external field  $F_L(t)$  and the induced nonlinear polarization  $P_{nl}$ . The induced nonlinear polarization  $P_{nl}$  of the system is increased considerably and restricted to the central part of the pulse, where the internal field differs from the incident laser field. Investigating the nonlinear relation between the incident field and the induced polarizability will offer valuable clues on the underlying electron dynamics. How this increased polarizability and its reversibility can possibly be probed in the optical domain is therefore subject of the next chapter.

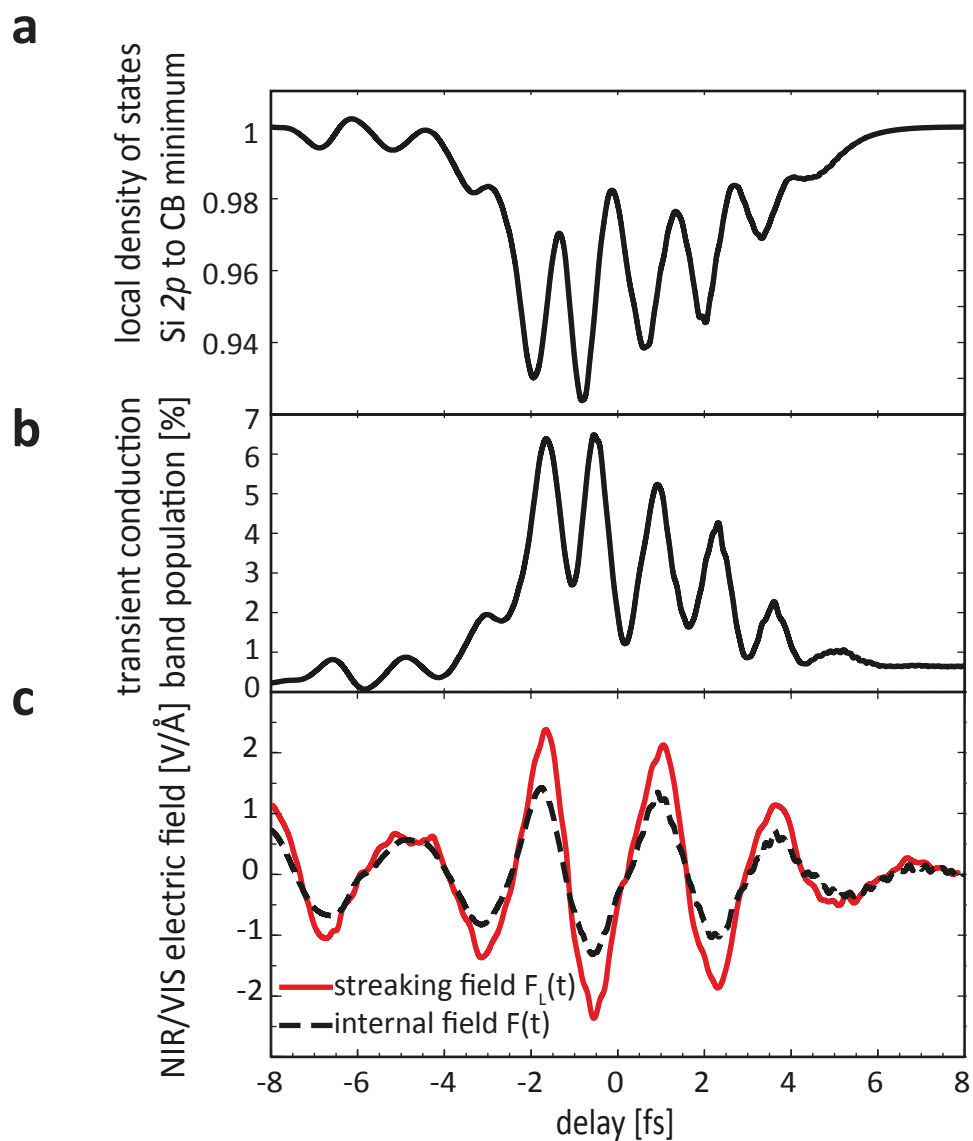


**Figure 4.13:** The simulated evolution of the local density of states at the position of the Si atom in the unit cell shown in panel **a** is reduced at high field strengths. Panel **b** shows the calculated transient and largely reversible population of the conduction band induced by the measured optical field shown as a solid line in panel **c**. The dashed line in panel **c** depicts the calculated internal field in the material, which is the superposition of the external field  $F_L(t)$  and the induced nonlinear polarization  $P_{nl}$ .





## Chapter 5

# Nonlinear polarization spectroscopy of SiO<sub>2</sub>

The optical properties of a material are governed by its microscopic ability to respond to an electromagnetic wave at a certain frequency  $\omega$ , the polarizability or optical susceptibility. At low optical intensity and in the absence of resonant absorption, the material will respond linearly to the incident field on a microscopic scale, with its electron charges oscillating at the same frequency only with different phase than the incident field. The reflected or transmitted wave then consists of a superposition of the fundamental wave and the radiation from the sample, leading to a change in phase and group velocity of the transmitted wave relative to vacuum, which is commonly described macroscopically as the index of refraction  $n$  and the linear susceptibility  $\chi^{(1)}$ . When the intensity of the electromagnetic wave and therefore the force on the electrons exceeds the level where the charge motion can respond linearly to the incident field, the induced polarization response of the material will be a function of higher orders of the incident field. This nonlinear polarization response is the basis for a wealth of nonlinear optical effects.

Nonlinear effects are for example used to generate new frequency components by nonlinear wave mixing such as low-order harmonic generation, sum- or difference frequency generation or optical parametric amplification, just to name a few. Also the material properties itself, i.e. the refractive index, can depend on the strength of the incident field. The nonlinear dependence on the field strength of such effects implies that the electric field itself can serve as a very sensitive and fine control knob for the interaction. While the principles of nonlinear optics in the perturbative regime are well-understood and nonlinear effects are routinely applied and used in lasers and communication technology, the effects resulting from the reversible and nonresonant electronic polarization response have never been time-resolved at the optical wave cycle. The experiments described in the following aim at investigating the nonlinear polarization response of SiO<sub>2</sub> to intense few-cycle NIR/VIS pulses. First, the reversibility of the nonlinear polarization response is tested in a time-resolved optical reflectance experiment. Then, the concept of attosecond transient polarization spectroscopy is introduced. This novel technique allows the real-time observation of the interaction of an intense few-cycle laser field with a transparent dielectric material. To provide a first proof-of-principle of the method, the intensity dependent change of the refractive index of SiO<sub>2</sub> (fused silica) and its effects on the transmitted pulse shape is resolved with sub-cycle resolution.

## 5.1 Time-resolved optical reflectance

In the previous chapter the reversible change in XUV absorptivity of thin SiO<sub>2</sub> films was explained by changes in the valence and conduction band states which also lead to an increased transient polarizability of the material. Such a transient change in polarizability should also lead to a significant change in the optical properties of the material that should be reversible at the time-scale of the pulse duration of the NIR/VIS pulse. A NIR/VIS pump-probe reflectance measurement is conducted in order to examine this prediction and to test the level of reversibility of the induced polarizability.

### 5.1.1 Experimental setup

In order to preserve the ultrashort pulse duration and to avoid detrimental effects of ionization when focusing the femtosecond pulses which easily leads to intensities well above  $10^{14}$  W/cm<sup>2</sup>, the pulse characterization and the pump-probe experiment are conducted in vacuum.

The linearly polarized IR/VIS pump and probe beams are derived from a single NIR/VIS beam of sub-4-fs pulses centered at 760 nm with  $\sim 300$   $\mu$ J pulse energy by means of a concentric double mirror setup similar to the one used for collinear attosecond streaking experiments [3, 4]. The concentric mirror setup consists of an inner core mirror which is partially reflective (reflectance  $\sim 10\%$ ) and a silver-coated outer mirror with a central hole (reflectance  $\geq 99\%$ ). The inner mirror is mounted on a high-precision piezo-actuated linear translation stage movable along the beam axis. This allows to introduce a relative delay between the weak probe pulse, reflected from the inner mirror, and the strong pump pulse that is reflected from the outer mirror. The power of the pump pulse can be adjusted by a variable aperture in front of the double mirror. The collinear pump and probe beam are subsequently focused by a concave mirror with a focal length of 30 cm onto the target.

For pulse characterization and optimization, a wedged glass substrate can be mechanically flipped into the beam before the focus to attenuate and redirect the two focused beams onto a 20  $\mu$ m thick beta-barium-borate (BBO) crystal, see Fig. 5.1 a. With the pump power reduced to match the probe power, the second harmonic signal generated in the the crystal, filtered with a high-pass filter from the fundamental radiation is recorded as a function of the relative delay between the two pulses. This fringe-resolved autocorrelation, shown in Fig. 5.2, confirms the sub-4-fs pulse duration of the pump-and probe pulses.

Fig. 5.2 b and c show the concentric interference pattern that can be observed with a CCD camera at the focus by varying the relative time-delay between pump and probe pulses. Due to the geometry of the collinear setup, the size of the pump spot is smaller than the probe spot. In case of high pump intensity and therefore a significantly higher numerical aperture of the pump beam with respect to the probe beam, the full-width at half-maximum beam diameter of the pump beam is only  $\sim 30\%$  of that of the probe spot. The measurement of the time-resolved reflectance therefore does not allow a quantitative assessment of the induced nonlinear increase of reflectance, but it reveals quite clearly the temporal dynamics of the effect.

For the time-resolved reflectance measurement from a SiO<sub>2</sub> surface, a thin wedged SiO<sub>2</sub> substrate is placed at the focus of the two p-polarized beams incident under Brewster's angle. The

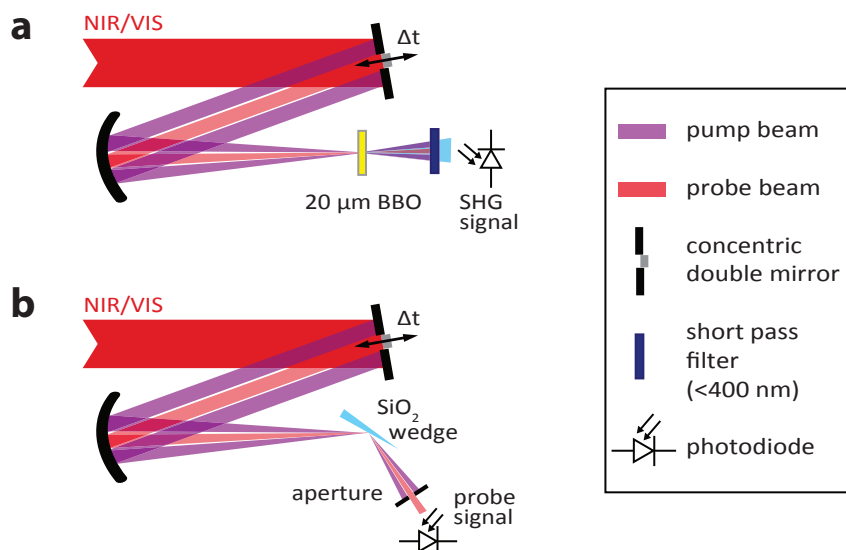


**Figure 5.1:** Sketch of the experimental setup for NIR/VIS pump-probe reflectance including the 2<sup>nd</sup> harmonic auto-correlation pulse characterization. The p-polarized strong (red) pump beam and the weak (violet) probe beam are derived from a single beam by a concentric double mirror. The inner mirror is mounted on a linear piezo stage, which allows to introduce a temporal delay  $\Delta t$  between the pump and probe pulses. Both beams are focused by a concave silver mirror either onto a 20  $\mu\text{m}$  thick BBO for second order autocorrelation or onto a thin SiO<sub>2</sub> wedged substrate under Brewster's angle (panel b). The reflected signal of the probe from the wedged surface is separated from the pump signal by an aperture and recorded with a fast photodiode and a boxcar integrator (Stanford Research) as function of delay time  $\tau$  between pump and probe.

reflected signal from the weak probe beam is recorded with a fast photodiode connected to a box-car integrator (Stanford Research) and a fast-sampling oscilloscope. As the laser pulses carry a small fraction of s-polarized light due to the modification of the polarization state of higher-order modes at the stage of supercontinuum generation in the neon-filled hollow-core fiber, a Glan-Thompson polarizer was used in front of the photodiode to reject any s-polarized component. This improves the contrast of the nonlinear reflectance measurement. A linear reflectance of  $10^{-4}$  could be achieved, which is close to the theoretical value for perfect surfaces at Brewster's angle. The residual reflectance originates from the variation of the refractive index and therefore the Brewster's angle within the large bandwidth of the NIR/VIS supercontinuum. To overcome low-frequency noise in the reflected signal, the time-delay between the pulses is scanned at a rate of 8 Hz over a delay range of  $\pm 30$  fs.

### 5.1.2 NIR/VIS pump-probe study of reversible polarization

One challenge of the time-resolved reflectance measurement is the nonlinearity of the effect. An increased reflectance of the sample could only be observed within 10-15% below the damage threshold intensity [64]. Therefore it was necessary to increase the pump power in small steps up to the damage threshold and reduce it from there by 2-5% to perform the time-resolved measurement. The quality of the reflected beam profile was observed as an indicator for optically induced damage as it shows strong structuring upon damage. In contrast to the fast intensity

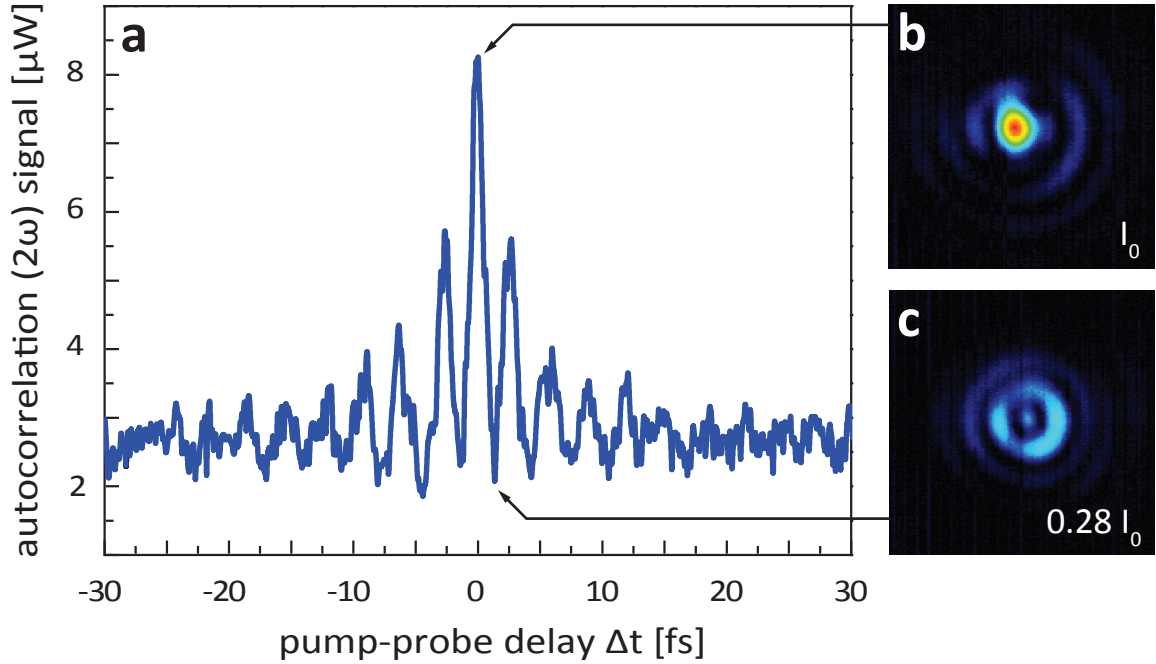
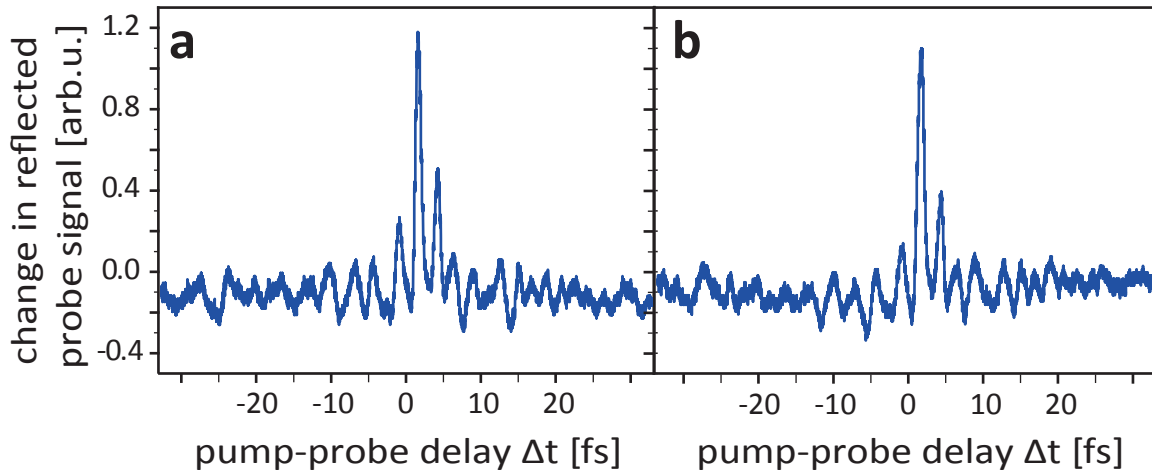


**Figure 5.2:** Second-harmonic autocorrelation signal with equally intense NIR/VIS pump and probe beams. Constructive (**b**) and destructive (**c**) concentric interference of the pump and the probe beam at the focus acquired with a CCD camera.

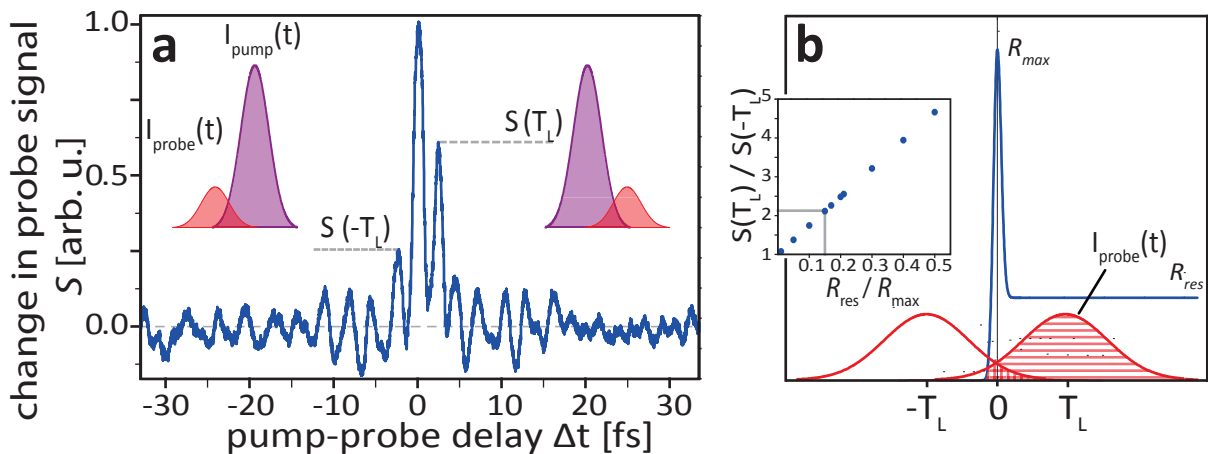
dependent optical breakdown, slow, presumably self-trapped exciton-related or defect-related cumulative thermal damage can be observed already for illumination below optical breakdown intensities. This slow damage component can be prevented by blocking the laser for several seconds between recording of the single time-traces.

Fig. 5.4 **a** shows the average of 10 individual scans selected from a set of 32 subsequent scans. The subset of the 10 scans was selected based on their peak signal strength at zero delay ( $\Delta\tau=0$  fs), which was within 25% of the most intense trace. Fig. 5.3 **a** and **b** show two representative individual scans from this subset. The peak signal strength of the individual traces is found to be extremely sensitive to laser intensity fluctuations in the percent range. This is corroborated by control measurements at a pump intensity reduced by 8%, shown in Fig. 5.5, where the induced enhanced reflectance disappears almost completely.

The time-resolved reflectance (Fig. 5.4 **a**) shows an asymmetry only in the fringes directly adjacent to the central maximum at  $\Delta\tau=\pm T_L$  with  $T_L$  being the laser oscillation period, while the fringes further apart from the maximum at  $\Delta\tau=\pm nT_L$  with  $n > 1$  show no appreciable asymmetry. The reflected intensity  $S$  at positive  $\Delta\tau=+T_L$ , where the pump pulse precedes the probe pulse at the target, is about  $2.1\pm 0.2$  times greater than at the opposite negative delay. For analysis of this asymmetric residual induced reflectance, we model the interaction in a simple heuristic approach, illustrated in Fig. 5.4 **b**. We assume that the induced reflectance consists of two components. The first component, denoted by  $R_{max}$ , is field-dependent and fully reversible, the second component,  $R_{res}$  builds up during the central peak of the field but is long-lived and



**Figure 5.3:** **a** and **b** show two representative scans of the reflected NIR/VIS probe intensity in function of the pump-probe delay. At negative delay times the probe pulse precedes the pump pulse. Only at the temporal overlap the reflectance is increased. Only at the adjacent maxima to the main peak, a slight asymmetry can be observed.



**Figure 5.4:** **(a)** Reflected power on axis of the probe pulse (represented by the red beam in Fig. 5.2 **(b)**); intensity envelope  $I_{probe}(t)$  as a function of the delay with respect to the strong pump pulse (illustrated by the violet intensity envelope  $I_{pump}(t)$ ). The curve is the result of an average of ten scans. **(b)** Illustration of the model of the reflected signal strength in dependence of the ratio between a fully reversible ( $R_{max}$ ) and a residual component ( $R_{res}$ ) of the reflectance induced by the pump pulse. The inset shows the ratio of the reflected probe signal at  $\pm T_L$  (corresponding to the maxima adjacent to the central peak) as a function of the ratio of  $R_{res}$  to  $R_{max}$ .

assumed to be constant after the pulse for the considered delay time up to 30 fs. The asymmetry or ratio between in the probe signal at  $\pm T_L$  depends on the ratio  $R_{res}/R_{max}$ , depicted in the inset in Fig. 5.4 **b**. For  $R_{res}/R_{max} \rightarrow 0$ , the trace would be fully symmetric. In contrast, a residual reflectance comparable to the peak value,  $R_{res}/R_{max} \rightarrow 1$  would lead to a very big asymmetry due to the short probe pulse duration. With this simple model, we can therefore deduce an upper limit of the ratio between the maximum and the residual reflectance of 0.15

## 5.1 Time-resolved optical reflectance

---

which provides compelling evidence for the substantial reversibility of the strong-field-induced increase in polarizability on the timescale of the optical wave cycle.

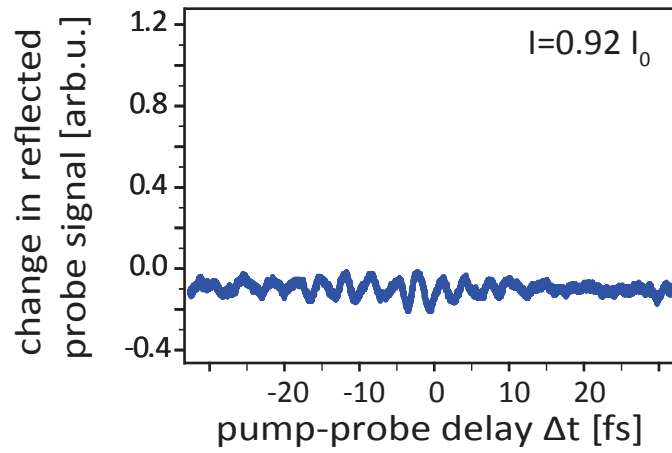


**Figure 5.5:** Time-resolved reflectance control measurement with 92% pump intensity compared to Fig. 5.4 a. The absence of a detectable reflectance autocorrelation signal shows the strong intensity dependence of the pump-induced increased reflectance.

## 5.2 Attosecond nonlinear polarization spectroscopy

In the previous section, the time-resolved reflectance of few-cycle NIR/VIS pulses from a SiO<sub>2</sub> surface witnessed the reversibility of the strong-field induced polarizability on the time-scale of an optical wave-cycle. Yet the subtleties of the interaction of the optical field with the induced polarization could not be resolved due to the limitation by the NIR/VIS pulse duration. In order to advance the temporal resolution of such an experiment, a novel measurement concept that extends the state-of-the-art of attosecond technology was developed in the course of this thesis. Attosecond nonlinear polarization spectroscopy allows the real-time observation of the interaction of an intense few-cycle laser field with a transparent dielectric material. To this end, the electric field of an intense CEP-controlled few-cycle NIR/VIS laser pulse that is transmitted through a thin transparent dielectric sample is characterized with the attosecond streaking technique, first with the sample being exposed to the NIR/VIS pulse at low intensity and second to the pulse at high intensity. Comparison of the two waveforms and the induced nonlinear phase and amplitude variations yields information on the induced polarization at the attosecond time-scale. The interpretation of such measurements requires modeling of the nonlinear pulse propagation and leads to new insights of ultrashort pulse propagation in nonlinear media. As first proof-of-principle of the method, the nonlinear change in refractive index in SiO<sub>2</sub> (fused silica) and group velocity leading to self-steepening are observed directly via the changes in the transmitted field and envelope.

### 5.2.1 Experimental setup

For the attosecond transient polarization experiment, the setup presented in section 4.1 was adapted to the requirements of the measurement, as shown in Fig. 5.6. While the high harmonic generation setup remains unchanged, the NIR/VIS-XUV interferometer situated in C2 has to incur additional functionalities. Before the first perforated mirror (PM1) that separates the NIR/VIS beam and the high harmonic XUV beam in the two arms of the interferometer, a variable motorized aperture (A2) is introduced to control the NIR/VIS power after the high harmonic generation chamber. In the NIR/VIS arm of the interferometer, an additional focus is created by a combination of a short focal length concave mirror with a shorter convex mirror such that the focal point is approximately at the center of the diagonal between the two perforated mirrors (PM1/PM2).

The beam transmitted in the NIR/VIS arm of the interferometer can be redirected by a motorized flip mirror and sent through a window onto a calibrated powermeter (D1). The transmission of the system and thus the power incident on the sample can be easily determined. This incident power is measured before each time-resolved scan. The Rayleigh length of this intermediate focus is calculated and characterized experimentally with a CCD camera to be  $\sim 5\text{-}10$  mm with a focal spot of  $w_0 \sim 35\text{-}50\mu\text{m}$ , controlled by the setting of the aperture A2. For the setting of A2 used in the experiment and each position of the sample, the focal spot is recorded with a CCD camera.



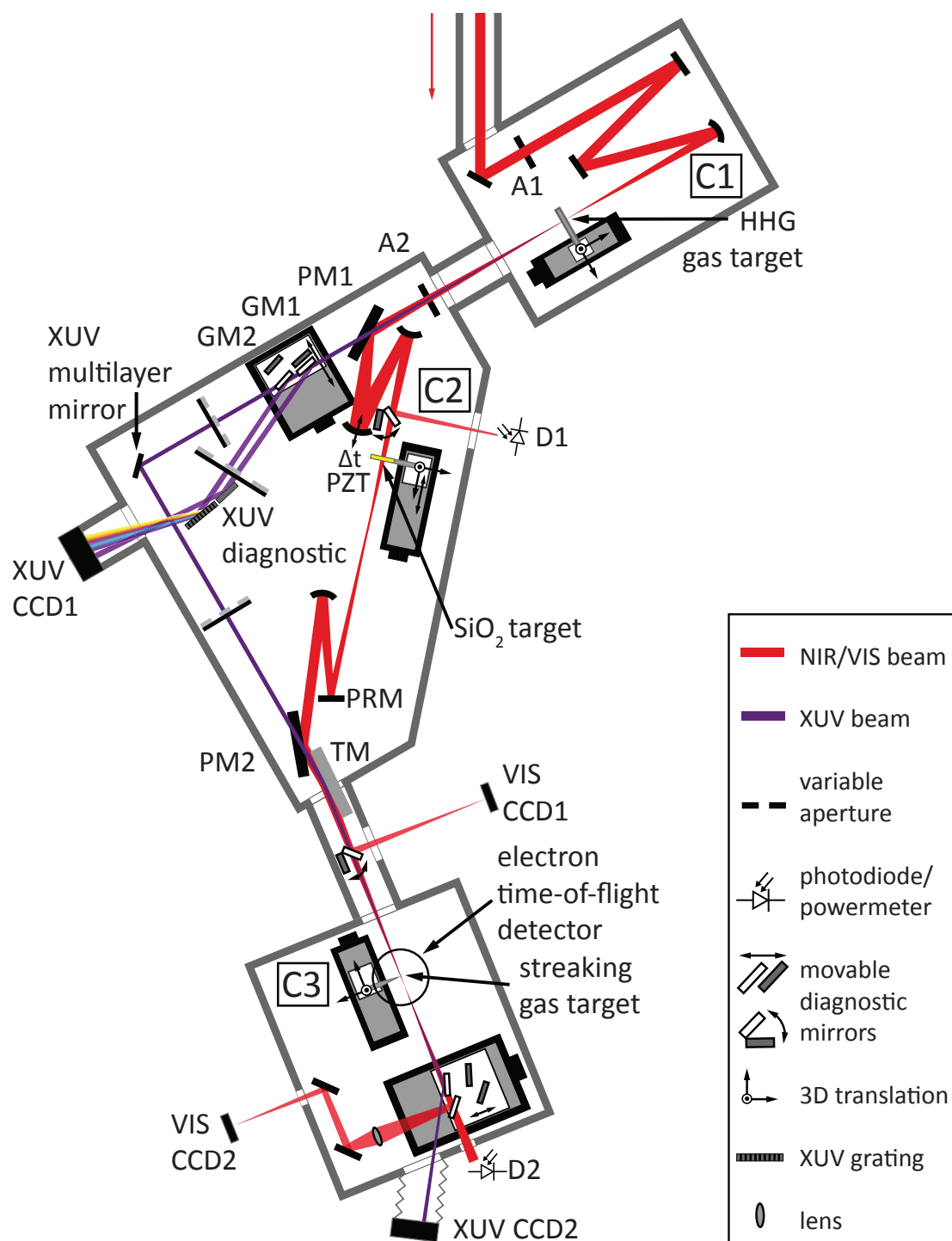


**Figure 5.6:** Experimental setup for attosecond polarization spectroscopy, adapted from the setup for transient absorption spectroscopy shown in chapter 4.1, Fig. 4.1. The main modifications are made in the interferometer chamber (C2). In the XUV arm of the interferometer, the XUV pulses are transported via a  $45^\circ$  multilayer mirror designed for 7.6 eV bandwidth centered at 130 eV. In the NIR/VIS arm of the Mach-Zehnder interferometer there is an additional focus in which the few micron thin  $\text{SiO}_2$  sample can be placed and translated along the optical path to expose the target to different intensities. The transmitted NIR/VIS waveforms are recorded with attosecond streaking in a dilute jet of Ne gas in the experimental chamber. Further details are given in the text and the legend.

A few micrometer thin  $\text{SiO}_2$  sample is placed under Brewster's angle in the NIR/VIS beam close to the intermediate focus. It is mounted on a 15 cm range step-motor translation stage that allows to move the sample along the beam path with its main part before the focus such that the sample can be exposed either to very high intensities close to the focus for nonlinear transmission as well as to low intensities far away from the focus, where the nonlinear phenomena affecting the transmission are negligible.

After the sample and the intermediate focus, the diverging beam is redirected to the second perforated mirror (PM2) and its divergence is adjusted by a plane mirror and a concave mirror to match the divergence of the XUV beam. No additional aperture is used to control the NIR/VIS streaking field strength, but instead the plane mirror is a partially reflective mirror with a reflectivity of either 4% (uncoated fused silica substrate) or 10% (custom broadband boron carbide (B4C) coating), depending on the desired streaking field strength. As the information on the nonlinear transmission is carried by the whole transmitted beam and nonlinear self-action such as self-focusing will modify the beam divergence, omitting the aperture is of paramount importance to transmit the maximum of information of the nonlinear interaction towards the experimental chamber where the waveform of the transmitted NIR/VIS pulses is characterized. In the XUV arm a multilayer mirror with aperiodic multilayer thicknesses optimized for flat spectral phase, which has been designed and produced by Alexander Guggenmos, selects a 7.6 eV bandwidth (full-width at half-maximum) centered at 130 eV from the unmodulated cut-off region of the XUV spectrum. Additionally, a 150 nm thin free-standing palladium filter suppresses the residual NIR/VIS radiation before the XUV multilayer mirror and, due to its negative dispersion in the XUV, helps to reduce the intrinsic harmonic generation chirp and to compress the XUV pulses. The resulting XUV pulse duration retrieved with ATTOgram [74] is about 400 as. The NIR/VIS pulses are recombined with the XUV pulses at the second perforated mirror (PM2) and focused by a toroidal mirror (TM) into the experimental chamber. Before the focus, the NIR/VIS beam can be redirected by a flip mirror installed in a small intermediate chamber between the interferometer chamber and the experimental chamber and sent through a window onto a CCD camera that is mounted on a motorized translation stage. This permits to characterize the beam profile along the converging beam path without the need for breaking the vacuum. This is important for detection of changes in the focusing behavior imparted on the beam by nonlinear self-focusing in the transmission target.

In the experimental chamber, a gas nozzle emitting a dilute stream of neon gas is placed close to but about 20 mm in front of the focus of the NIR/VIS and XUV focus for attosecond streaking. The time-of-flight or energy spectrum of the electrons liberated by the XUV pulse from Ne  $2p$  states is recorded with a time-of-flight spectrometer oriented parallel to the NIR/VIS linear polarization, which is perpendicular to the sketch plane in Fig. 5.6.

The NIR/VIS beam is transmitted through a window at the back side of the experimental chamber. Here, the power is recorded for each individual streaking scan with a second calibrated powermeter (D2).

The streaking target was placed in front of the actual focus at the edge of the Rayleigh range because the nonlinear self-focusing in the transmission sample moves the focal point in the experimental chamber further downstream in the beam path. By placing the streaking target in front of the actual focus at the edge of the Rayleigh range, the induced Gouy phase shift (the phase shift of  $\pi$  that a Gaussian beam undergoes when passing through a focus in an arctan-like manner) is minimized. As it became clear only after careful analysis and modeling of the

nonlinear propagation, this choice was unfavorable as it impeded the precise quantitative measurement of induced polarization changes in the transmitted beam. However, this configuration still permitted to clearly see effects of the induced nonlinear polarization. A new, optimized setup is currently devised based on the findings from this first proof-of-principle study.

### 5.2.2 Sample requirements

Observing nonlinear polarization with few-cycle NIR/VIS pulses in a dielectric requires samples that are thick enough to imprint a measurable change on the waveform (typically several times the wavelength in the material) but thin enough to prevent the detrimental effects of linear dispersion on the short pulse. A significant change in chirp due to group velocity dispersion would lead to a broadening of the pulse in time and hence the peak intensity would change during propagation through the medium. With a group velocity dispersion of  $\sim 36 \text{ fs}^2/\text{mm}$ ,  $100 \mu\text{m}$  of fused silica would stretch a 5 fs pulse to about 5.5 fs. But not only the pulse duration but also the carrier-envelope phase can change already over a small propagation length: propagation through  $\sim 23 \mu\text{m}$  for example leads to a change in CEP of  $\pi$  [28].

The desired fused silica sample thickness is therefore on the order of 5 to 25  $\mu\text{m}$ .  $\text{SiO}_2$  plates down to 20 micrometer thickness are commercially available with good surface quality (Valley-Design Inc.), thinner samples are only produced on best-effort basis and had to be prepared and characterized. The preparation and characterization of these thin samples is described in the appendix A.2.

### 5.2.3 Time-resolved manifestation of self-steepening and Kerr effect

Attosecond streaking allows to characterize the NIR/VIS waveform that is transmitted through the thin  $\text{SiO}_2$  samples placed in the NIR/VIS arm of the XUV-NIR/VIS interferometer. The changes to the waveform due to nonlinear propagation can be evaluated by streaking spectrograms of waveforms that have been transmitted through the sample at different high-intensity settings in comparison with a reference waveform transmitted through the sample at low intensity. In order to exclude long-term drifts of power as well as delay within the interferometer with respect to a reference waveform for linear transmission at low intensity, a reference waveform is recorded either after each or each second scan at high intensity. This kind of measurement makes high demands on the stability of the optical setup as well as on the CEP-stabilization. With each scan taking between 6 and 10 minutes, intensity dependent scan series over several hours are possible.

For this study, it is crucial to accurately determine the maximum intensity on the  $\text{SiO}_2$  sample in the intermediate focus. For few-cycle NIR/VIS pulses, the maximum intensity is very sensitive to the actual waveform of the electric field under the envelope. Fortunately, the attosecond streaking trace of the reference waveform provides a reliable measurement of the peak electric field strength at the streaking focus  $E_{str}$ . In combination with the pulse energy at the streaking focus  $W_{str}$  (measured with D2) and the intermediate focus  $W_{\text{SiO}_2}$  (measured with D1), the focus size at the position of the streaking target  $A_{str}$  (measured with a CCD camera (VIS CCD1))

and the focus size at the position of the sample  $A_{SiO_2}$  (also measured with a CCD camera and appropriate reflective filters at the positions of the sample used in the experiment each day after completion of the experiment), the maximum intensity on target can then be determined as:

$$I_{SiO_2} = \frac{1}{2} \epsilon_0 c \cdot E_{str}^2 \cdot \frac{A_{str}}{A_{SiO_2}} \frac{W_{SiO_2}}{W_{str}}. \quad (5.1)$$

It is clear that such measurements bear some experimental error, where the dominant contribution to the error is the accuracy by which the maximum streaking field strength can be determined, which is subject to fluctuations of the laser pulse energy between individual streaking scans. This accuracy is about 1%, determined from the deviation of reference measurements recorded under nominally identical conditions, translating into an error of  $\sim 5 \cdot 10^{11} \text{ W/cm}^2$  in intensity.

Fig. 5.7 shows an exemplary triplet of waveforms recorded in a sequence with the blue and the black line representing the reference waveforms transmitted at low intensity of  $\sim 0.1 \pm 0.05 \cdot 10^{13} \text{ W/cm}^2$  through  $15.1 \pm 0.3 \mu\text{m}$   $\text{SiO}_2$  and the red line corresponds to a waveform transmitted at an intensity of  $\sim 2.8 \pm 0.05 \cdot 10^{13} \text{ W/cm}^2$ . Negative delays represent the attosecond pulse preceding the NIR/VIS pulse, so that the NIR/VIS pulse front appears in the plot at the left hand side. The positive phase shift of the waveform depicted in red results from the optical Kerr-effect that causes an intensity dependent increase of the refractive index [17]. This results in a delay (shift towards the right in Fig. 5.7) the central part of the pulse with respect to the reference waveform.

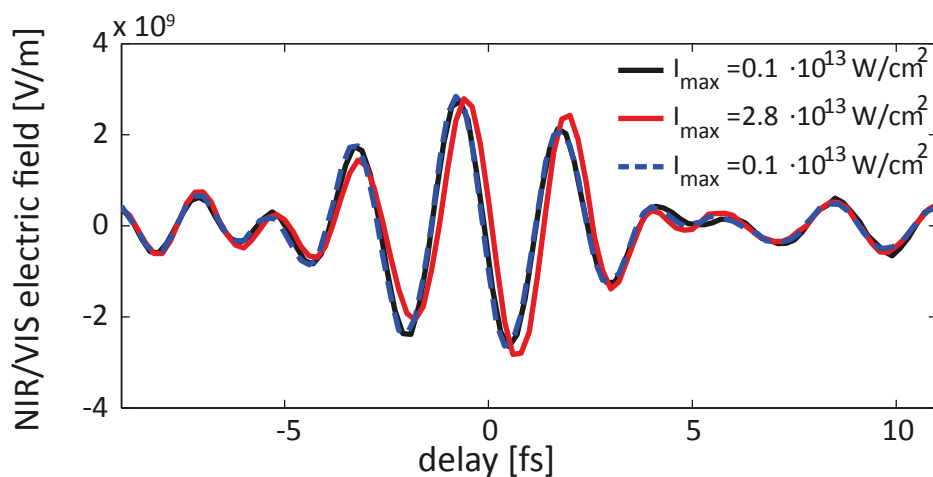


**Figure 5.7:** Attosecond nonlinear polarization spectra: Waveforms transmitted through a  $12.4 \pm 0.2 \mu\text{m}$   $\text{SiO}_2$  sample placed under Brewster's angle at low (blue dashed and black solid lines) intensity and high (solid red line) intensity of  $2.8 \cdot 10^{13} \text{ W/cm}^2$ . The increasing phase shift and the self-steepening leading to a change of the envelope towards the pulse end (positive delay time) with a reduced field amplitude at the pulse front and an increased amplitude towards the end are clearly visible.

Fig. 5.8 shows the waveforms transmitted through a  $12.4 \mu\text{m}$   $\text{SiO}_2$  sample under Brewster's angle (optical path length is  $15.1 \mu\text{m}$   $\text{SiO}_2$ ) at increasing intensity from  $0.1 \cdot 10^{13} \text{ W/cm}^2$  up to  $3 \cdot 10^{13} \text{ W/cm}^2$ . The phase shift in the central part of the pulse is due to the Kerr-effect is

clearly visible for the highest intensity (solid red line), while at the pulse front (negative delays) and pulse end the waveforms coincide. Also the relative strength of the electric field is reduced at the pulse front and enhanced at the pulse end, a clear sign of self-steepening that is here for the first time resolved at the wave-cycle.

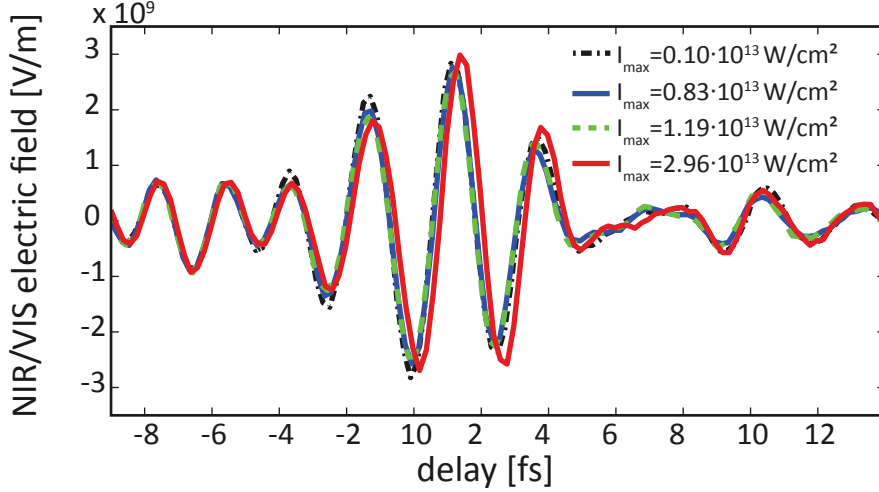


**Figure 5.8:** Waveforms transmitted through a 12.4  $\mu\text{m}$   $\text{SiO}_2$  sample at increasing intensity from  $0.1 \cdot 10^{13} \text{W/cm}^2$  up to  $3 \cdot 10^{13} \text{W/cm}^2$ , showing clearly the nonlinear phase shift in the central part of the pulse as well as the amplitude changes due to self-steepening.

At an intensity in the range of up to  $3 \cdot 10^{13} \text{W/cm}^2$ , the third order nonlinearity dominates the observable effects. The effects of nonlinear propagation observed in the experiment can be deduced from the nonlinear wave equation (Eq. 2.24) in the moving frame of reference following [89] that has been derived in section 2.2:

$$\frac{\partial A}{\partial z'} = \frac{i\omega_0}{2\epsilon_0 c n_0} \left[ 1 + \frac{i}{\omega_0} \frac{\partial}{\partial \tau} \right] p(z, t) \quad (5.2)$$

Assuming a material exhibiting an instantaneous third order nonlinearity  $p = 3\epsilon_0 \chi^{(3)} |A|^2 A = 3\epsilon_0 \chi^{(3)} A^* \cdot A \cdot A$ , the change in the nonlinear wave equation can be written as

$$\begin{aligned} \frac{\partial A}{\partial z'} &= \frac{i3\omega_0 \chi^{(3)}}{2cn_0} \left[ 1 + \frac{i}{\omega_0} \frac{\partial}{\partial \tau} \right] |A|^2 A \\ \frac{\partial A}{\partial z'} &= \frac{i3\omega_0 \chi^{(3)}}{2cn_0} |A|^2 A - \frac{3\chi^{(3)}}{2cn_0} \left[ A^2 \frac{\partial A^*}{\partial \tau} + 2|A|^2 \frac{\partial A}{\partial \tau} \right]. \end{aligned} \quad (5.3)$$

The last term can be reformulated in the form of an intensity dependent and therefore also

time-dependent change in group velocity  $\Delta n_g(t)$  with the intensity  $I = 2n_0\epsilon_0c|A|^2$

$$\begin{aligned}\frac{\Delta n_g(t)}{c} \frac{\partial A}{\partial \tau} &= \frac{1}{c} \frac{3\chi^{(3)}}{n_0} |A|^2 \frac{\partial A}{\partial \tau} \\ &= \frac{1}{c} \frac{3\chi^{(3)}}{n_0} |A|^2 \frac{\partial A}{\partial \tau} \\ &= \frac{1}{c} \frac{3\chi^{(3)}}{2cn_0^2\epsilon_0} I \frac{\partial A}{\partial \tau}\end{aligned}\quad (5.4)$$

where the intensity dependent group velocity index is connected to the nonlinear index of refraction  $n_2I$

$$\Delta n_g(t) = \frac{3\chi^{(3)}}{2cn_0^2\epsilon_0} I(t) = 2n_2I(t) \quad (5.5)$$

Using this we can deduce the time-averaged change in refractive index from the shift of the first moment of the envelope  $A(t)$  due to this time-dependent group velocity, which has been proposed by Nicholas Karpowicz. Assuming a Gaussian pulse of the form

$$I(t) = I_0 e^{-\frac{t^2}{\tau^2}} \quad (5.6)$$

the time-averaged value of the group index change  $\langle \Delta n_g \rangle$  can be written as

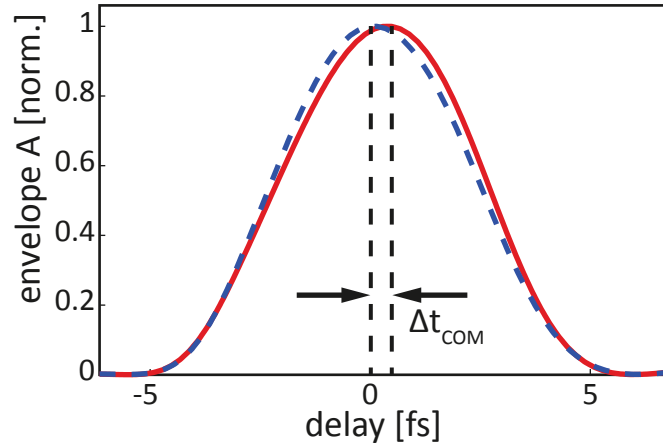
$$\begin{aligned}\langle \Delta n_g \rangle &= \frac{\int_{-\infty}^{+\infty} dt I(t) \Delta n_{group}(t)}{\int_{-\infty}^{+\infty} dt I(t)} \\ &= 4n_2I_0 \frac{\int_{-\infty}^{+\infty} dt e^{-\frac{2 \cdot t^2}{\tau^2}}}{\int_{-\infty}^{+\infty} dt e^{-\frac{t^2}{\tau^2}}} \\ &= 2\sqrt{2}n_2I_0,\end{aligned}\quad (5.7)$$

which results in a relative shift of the first moment  $\langle \Delta t_{COM} \rangle$  of the envelope upon propagation through the nonlinear medium over a distance  $\Delta z$  of

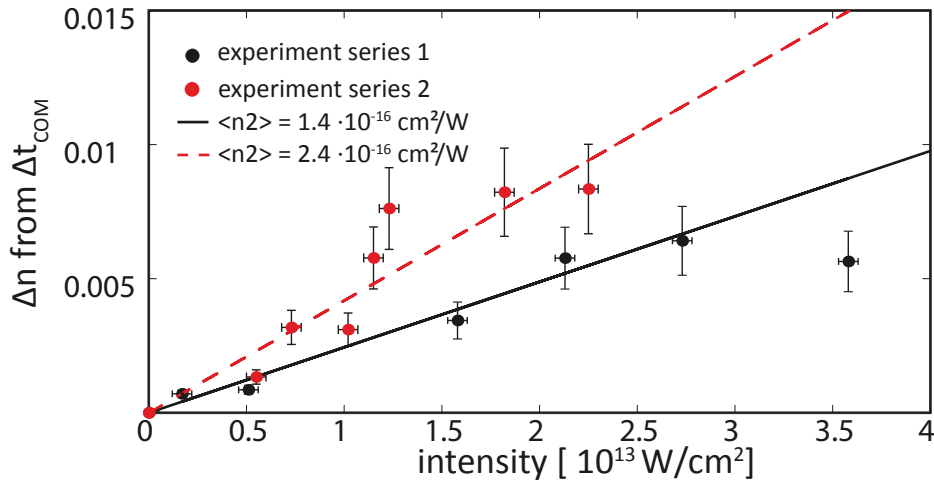
$$\langle \Delta t_{COM} \rangle = 2\sqrt{2}n_2I_0 \frac{\Delta z}{c} \quad (5.8)$$

Fig. 5.9 shows how the envelope of a few-cycle NIR/VIS pulse changes between linear transmission through a sub-20  $\mu\text{m}$  thin  $\text{SiO}_2$  sample at low intensity and nonlinear transmission showing the effects of the third-order nonlinearity.

Fig. 5.10 shows the change in refractive index  $\Delta n = n_2 \cdot I$  evaluated for two series of intensity scans for a 12.4  $\mu\text{m}$   $\text{SiO}_2$  sample. The maximum change in  $n$  that could be measured amounts



**Figure 5.9:** Envelope of a few-cycle NIR/VIS pulse that has propagated through a nonlinear medium with third order nonlinearity. The dashed blue line shows the envelope in case of transmission of the few-cycle pulse at low intensity, where the nonlinear propagation is negligible. The solid red line shows the envelope after propagation through the medium high intensity, where the third order nonlinearity leads to an intensity dependent group velocity and self-steepening of the envelope towards the trailing edge. The intensity dependent group index results in a change in the first moment of the envelope,  $\Delta t_{COM}$ .



**Figure 5.10:** The change in refractive index  $\Delta n = n_2 \cdot I$  evaluated for two series of intensity scans for a  $12.6 \mu\text{m}$   $\text{SiO}_2$  sample. The two series of measurements (black and red) were evaluated independently because they were recorded on different days with slightly different waveforms. The error in intensity is quantified by the deviation of intensities between reference measurements recorded under nominally identical conditions  $\sim 5 \cdot 10^{11} \text{ W/cm}^2$ . Due to the influence of self-focusing in the sample at high intensities, that increases with intensity but is difficult to quantify, the relative error in the change in refractive index under the current experimental conditions is estimated to be at the order of 20% of the experimental value.

to up to 0.08. The change in refractive index scales linearly with intensity and, assuming that 3<sup>rd</sup> order effects are at the origin of the observed delay of the envelope, the nonlinear index of refraction  $n_2$  can be determined as the slope of the linear fit to the data. The values for  $n_2$  of  $1.4\text{-}2.4 \cdot 10^{16} \text{ cm}^2/\text{W}$  are slightly below the value estimated in literature [169] for the purely electronic contribution to the nonlinear refractive index without the Raman contribution to the

third order susceptibility, that is present in measurements (for example with the z-scan-technique [170]) with longer pulses. The two series of measurements (black and red) were evaluated independently because they were recorded on different days with slightly different waveforms. Since the influence of self-focusing in the sample on the measurements led to a translation of the streaking focus along the beam axis for different sample positions, the quantitative information from these first measurements has to be regarded with caution. The possible error due to the self-focusing increases with intensity but it is difficult to quantify, so the relative error in the change in refractive index under the current experimental conditions is estimated to be at the order of 20% of the experimental value of  $\Delta n$ .

With  $\sim 4\text{-}5 \cdot 10^{13}$  W/cm<sup>2</sup> the damage threshold of the sub-20  $\mu\text{m}$  samples used in this first experiment was lower than the damage threshold of up to  $3 \cdot 10^{14}$  W/cm<sup>2</sup> reported in literature for thick substrates [95, 96], so the non-perturbative regime could not yet be investigated. It is possible that stress induced in the material by the polishing process or other extrinsic factors such as surface contamination might play a role and will be subject to further investigations. A new setup is currently under development, where the sample will remain fixed in the intermediate focus and the intensity on the sample will be changed by rotating a mirror with several segments with different reflectivity values, as sketched in Fig. 5.11.

In conclusion, this proof-of-method experiment shows that nonlinear polarization in a dielectric can be resolved at the wave-cycle with the technique of attosecond nonlinear polarization spectroscopy. The technique promises to yield insight into the higher order perturbative polarization dynamics. As the only limitation to the applicable intensity is the damage threshold of the material, the ultimate goal is to access the non-perturbative regime of polarization in dielectrics by few-cycle laser with this technique.

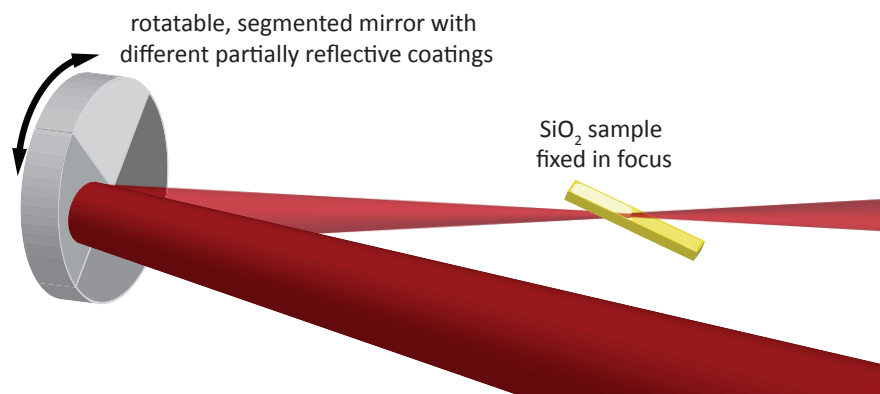


**Figure 5.11:** Sketch of the rotatable, segmented mirror with different reflectivity at each segment that will be used in the new setup for attosecond polarization spectroscopy.





# Chapter 6

## Conclusions and Outlook

In the framework of this thesis, established concepts of time-resolved femtosecond and attosecond spectroscopy have been employed and developed further with the aim of gaining new insight into the electron dynamics in wide band gap solids. The dynamics of resonant and off-resonant electronic excitation processes in semiconductors and dielectrics driven by intense ultrashort light pulses have been investigated experimentally on the sub-femtosecond time scale.

One key aspect of this work is the investigation of the influence of resonant excitation of electronic states in titanium-dioxide ( $\text{TiO}_2$ ) on the vibrational modes of the lattice. The resonant excitation with an ultrashort ultraviolet laser pulse causes a change in the lattice's potential energy surface that leads to a macroscopic coherent phonon oscillation in the excited volume. This coherent phonon oscillation can be detected via a time-resolved reflectance measurement using an equally short ultraviolet probe pulse, as the optical properties are connected to the lattice properties. The initial phase of this oscillation relative to the moment of excitation indicates a strong correlation between the evolution of the electronic excitation and the potential energy surface of the lattice. Using density-functional-theory calculations of the potential energy surface in dependence of the excitation state, a model has been developed that shows, that not only the excitation into states above the conduction band minimum but also the relaxation dynamics of these states has a pronounced effect on the lattice properties. This finding contributes to a better understanding of the dynamics of carrier excitation and relaxation in semiconductors.

The other key aspect of this thesis is the influence of intense, few-cycle near-infrared laser pulses on the in electronic states and the induced nonlinear polarization in fused silica (amorphous silicon dioxide,  $\text{SiO}_2$ ).

Time-resolved absorption measurements on sub-micrometer thin  $\text{SiO}_2$  films employing sub-100 as extreme-ultraviolet pulses that cover the characteristic absorption of  $\text{SiO}_2$  from core-level to conduction band states yield information on the evolution of electronic states in presence of intense, few-cycle NIR pulses. This measurement has been combined with the wave-cycle resolved characterization of the near-infrared electric field with attosecond streaking and employed simultaneously in one experiment for the first time. At the temporal overlap of both pulses and at an near-infrared electric field strength at the order of  $2\text{V}/\text{\AA}$ , the absorption of the extreme-ultraviolet spectrum at the core-level-to-conduction band transition frequency shows a significant reduction in optical density that oscillates periodically with twice the laser frequency, hence the modulus of the optical field. At the same time, the states at the conduction band minimum ex-

perience a Stark-shift towards lower energies that is also driven by the optical field. The changes in optical density are present, albeit with smaller amplitude, over an extended energy range of several electron volts in the conduction band. Due to the large bandwidth in which polarization is induced by the attosecond pulses, it exhibits a fast dephasing at the time scale of the attosecond pulse duration, which provides real time insight into the dynamics of the electronic states. The change in optical density is only present during the pulse duration and overlap with the near-infrared laser pulse, and it starts and ends abruptly within a sub-femtosecond time window. The correlation with the simultaneously recorded near infrared wave cycles allows a direct comparison with quantum-mechanical modeling of the experiment, that uses the experimental field as input parameter. The simulation describes the interaction of the few-cycle field with the dielectric in the non-perturbative regime. A considerable agreement between the experimental results and the simulation corroborates the interpretation that, in principle, the properties of dielectrics such as the nonlinear polarization can be modified significantly and reversibly with the electric field of intense ultrashort light pulses.

The reversibility of the near-infrared-pulse-induced polarization has been investigated in another experiment on SiO<sub>2</sub> surfaces using time-resolved reflectance measurements. The reflectance of a SiO<sub>2</sub> surface is increased with an intense few-cycle near-infrared pulse and probed by a weak probe pulse of equal pulse duration and frequency. This increase in reflectance shows only little asymmetry with respect to the temporal overlap of both pulses and it returned to its initial value at the time scale of the pulse duration. This result provides additional, model-independent evidence for the reversibility of the induced polarization.

In order to investigate the interaction of the light field and the induced polarization with higher temporal accuracy, the new experimental concept of attosecond polarization spectroscopy has been developed. The electric field of a near-infrared pulse that has been transmitted through a few micrometer thin SiO<sub>2</sub> sample is characterized with attosecond streaking. The electric field is modified by the nonlinear propagation through the dielectric medium that depends on the maximum electric field strength. The intensity and with it the maximum electric field strength in the sample is varied by positioning the sample at different positions along the beam path of the focused near-infrared beam. A comparison of the waveform with a reference waveform that has been transmitted through the sample at significantly lower maximum field strength yields information on the induced nonlinear polarization. With this technique, the effects of nonlinear polarization from the third order susceptibility, that leads to an intensity dependent refractive index, could be resolved at the time-scale of the wave cycle.

Attosecond metrology applied to solid states systems to explore the electron dynamics inside the bulk is still at a very early stage, but the first results obtained using isolated attosecond pulses provide a promising perspective. Attosecond transient absorption spectroscopy and simultaneous attosecond streaking spectroscopy allows to study light field induced electron dynamics with exact timing to the light field. In combination with ultrashort ultraviolet pulses as probe pulses, transitions from valence band states to conduction band states could be probed more directly. The non-perturbative effects that become significant at field strengths of 1.5-2 V/Å induced in dielectrics by intense few-cycle laser pulses will be the focus of attosecond polarization spectroscopy in the near future.

# Appendix A

## A.1 Wien2k modeling parameters

As described in the supplemental material of [127], the details on modeling parameters are given here:

The muffin-tin radii of Ti and O were 2.0 and 1.6  $a_0$ , with  $a_0$  being the Bohr radius. The cutoff energy of the plane-wave basis set was set to 260 eV, which largely exceeds the minimum requirements for the present calculations. For the sampling of the Brillouin zone a  $12 \times 12 \times 20$   $\mathbf{k}$  grid including the  $\Gamma$  point was used. The local density approximation was used to describe the exchange and correlation potential and energy. All self-consistent calculations were done for the electronic ground state. Excited state properties were obtained by equating

$$\Delta E_{tot} = \Delta E_{band}, \tag{A.1}$$

from which changes in the band energy can be obtained using the Kohn-Sham levels. Eeuwe Zijlstra and Martin Garcia et al. have already shown in a previous publication that for Bi this is a very good approximation [153].

In the case of  $\text{TiO}_2$  this approach was checked by comparing laser-excited PES at an electronic temperature of 0.408 eV, which we calculated both self-consistently and using Eq. A.1. Here, the number of electron-hole pairs was variable, because only one Fermi function was used for the occupancies of all electron states. As only minor differences in the computed PES minimum and  $A_{1g}$  frequency were detectable, we considered this to be a very reasonable approach.

## A.2 SiO<sub>2</sub> samples

### A.2.1 Sub-micrometer thin SiO<sub>2</sub> samples for XUV transmission

The 125 nm thin samples used for the experiment in chapter 4 were produced by TEMwindows.com. The samples are evaporated on a silicon substrate that is etched away to form 2.5 mm x 1.5 mm sized, free-standing 125 nm ( $\pm 5\%$ ) windows on a silicon support frame as depicted in Fig. A.2.

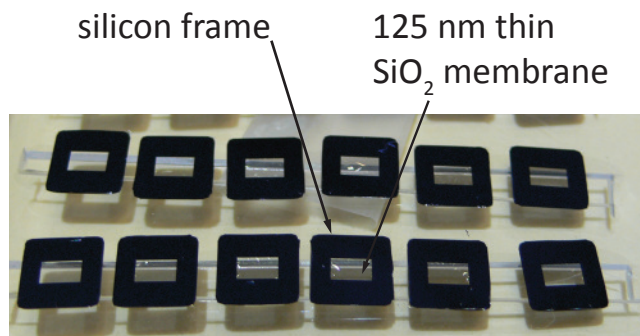


**Figure A.2:** 125 nm thin, free-standing SiO<sub>2</sub> windows on a silicon support frame used in the XUV transmission experiment in chapter 4.

### A.2.2 Sub-50 micrometer thin SiO<sub>2</sub> samples for NIR transmission

The samples used for the nonlinear transmission experiments in chapter 5 have been produced by ValleyDesign Inc., german sales partner: Hebo Spezialglas.

In principle, SiO<sub>2</sub> can be polished down to a thickness of  $\sim 5$  micrometers, when the material resides on a thick glass carrier to which the sample is attached by a thin film of mounting wax. But through the increased strain such thin polished samples are very brittle and have to be shipped on the glass carrier. The removal of the samples from the glass carrier is the most critical step in the sample preparation.

In order to remove the sample from the glass carrier, the viscosity of the mounting wax has to be reduced by heating the glass carrier to  $\sim 200^\circ$ . Once the mounting wax gets warm, the thin samples can be slid from the glass carrier by carefully pushing it with a sharp metal blade towards the edges of the glass carrier.

The residual mounting wax has to be removed with subsequent immersion in iso-propanol on an optical tissue. Despite the brittleness of the material, handling with flat tweezers is possible. For the experiment, the sample has to be mounted covering a suitably sized aperture for transmission of the NIR/VIS beam. As such thin samples cannot be clamped or glued because this would distort the surface, the sample was fixed on a metal ring with viscous ultrahigh vacuum grease applied on two opposite edges from the top as shown in Fig. A.3. This method is sufficient to fix the lightweight samples to the metal ring without additional strain and has been tested successfully for samples up to the size of 10x10x0.05 mm.

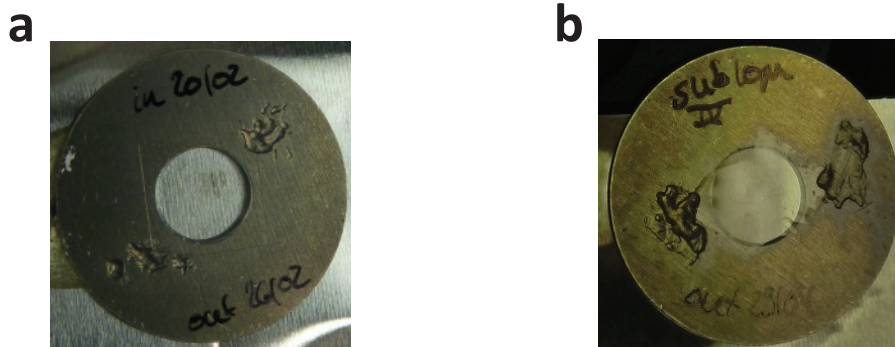


**Figure A.3:** 20  $\mu\text{m}$  (a) and sub-20 $\mu\text{m}$  (b) samples fixed on a metal support with ultrahigh-vacuum grease.

The thickness of the individual samples was determined by white-light interference using a calibration lamp. The white light spectrum is recorded in transmission through the thin SiO<sub>2</sub> sample under normal incidence. The spectral positions of the observed interference maxima or minima depend on the thickness. For  $N$  maxima separated by the difference in wavelength  $(\lambda_2 - \lambda_1)$ , as shown in Fig. A.4, the thickness  $d$  of the sample is

$$d = \frac{N\lambda_1 \cdot \lambda_2}{2n \cdot (\lambda_2 - \lambda_1)} \quad (\text{A.2})$$

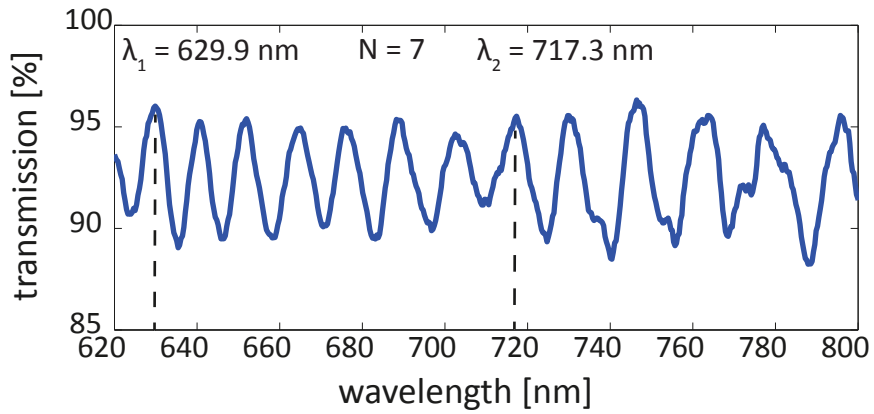


**Figure A.4:** White light interference spectrum of a  $12.4 \pm 0.2$  micron thin SiO<sub>2</sub> sample used in the experiments in chapter 5.

With  $\lambda_1 = 629.9 \pm 0.5 \text{ nm}$ ,  $\lambda_2 = 717.3 \pm 0.5 \text{ nm}$  and the refractive index of fused silica  $n = 1.46$ , the thickness of the sample is  $12.4 \pm 0.2 \text{ }\mu\text{m}$ .



## A.3 Storage of raw data and analysis programs

The original data as well as the analysis programs developed for the data evaluation are stored on the Data Archive Computer (DAC) of the Division for Attosecond Physics at the Max Planck Institute of Quantum Optics. The source files (raw data) and all Matlab, Mathematica and Origin routines used for obtaining the figures included in this thesis are stored in one folder for each figure separately.

# Bibliography

- [1] A. Schiffrin, T. Paasch-Colberg, N. Karpowicz, V. Apalkov, D. Gerster, S. Mühlbrandt, M. Korbman, J. Reichert, M. Schultze, S. Holzner, J. V. Barth, R. Kienberger, R. Ernstorfer, V. S. Yakovlev, M. I. Stockman, and F. Krausz, “Optical-field-induced current in dielectrics.,” *Nature*, vol. 493, pp. 70–74, Jan. 2013.
- [2] R. Kienberger, E. Goulielmakis, M. Uiberacker, A. Baltuška, V. S. Yakovlev, F. Bammer, A. Scrinzi, T. Westerwalbesloh, U. Kleineberg, U. Heinzmann, M. Drescher, and F. Krausz, “Atomic transient recorder,” *Nature*, vol. 427, no. 6977, pp. 817–821, 2004.
- [3] E. Goulielmakis, M. Uiberacker, R. Kienberger, A. Baltuška, V. S. Yakovlev, A. Scrinzi, T. Westerwalbesloh, U. Kleineberg, U. Heinzmann, M. Drescher, and F. Krausz, “Direct measurement of light waves,” *Science*, vol. 305, no. 5688, pp. 1267–1269, 2004.
- [4] M. Schultze, M. Fiess, N. Karpowicz, J. Gagnon, M. Korbman, M. Hofstetter, S. Neppl, A. L. Cavalieri, Y. Komninos, T. Mercouris, C. A. Nicolaides, R. Pazourek, S. Nagele, J. Feist, J. Burgdörfer, A. M. Azzeer, R. Ernstorfer, R. Kienberger, U. Kleineberg, E. Goulielmakis, F. Krausz, and V. S. Yakovlev, “Delay in photoemission.,” *Science*, vol. 328, pp. 1658–1662, June 2010.
- [5] A. Wirth, M. T. Hassan, I. Grguraš, J. Gagnon, A. Moulet, T. T. Luu, S. Pabst, R. Santra, Z. A. Alahmed, A. M. Azzeer, V. S. Yakovlev, V. Pervak, F. Krausz, and E. Goulielmakis, “Synthesized Light Transients.,” *Science*, vol. 334, pp. 195–200, Sept. 2011.
- [6] A. L. Cavalieri, N. Müller, T. Uphues, V. S. Yakovlev, A. Baltuška, B. Horvath, B. Schmidt, L. Blümel, R. Holzwarth, S. Hendel, M. Drescher, U. Kleineberg, P. M. Echenique, R. Kienberger, F. Krausz, and U. Heinzmann, “Attosecond spectroscopy in condensed matter.,” *Nature*, vol. 449, pp. 1029–32, Oct. 2007.
- [7] S. Neppl, R. Ernstorfer, E. M. Bothschafter, A. L. Cavalieri, D. Menzel, J. V. Barth, F. Krausz, R. Kienberger, and P. Feulner, “Attosecond Time-Resolved Photoemission from Core and Valence States of Magnesium,” *Physical Review Letters*, vol. 109, p. 087401, Aug. 2012.
- [8] S. Neppl, *Attosecond Time-Resolved Photoemission from Surfaces and Interfaces*. PhD thesis, Technische Universität München, 2012.
- [9] J. Itatani, J. Levesque, D. Zeidler, H. Niikura, H. Pépin, J. C. Kieffer, P. B. Corkum, and D. M. Villeneuve, “Tomographic imaging of molecular orbitals.,” *Nature*, vol. 432, pp. 867–71, Dec. 2004.

- [10] H. Niikura, H. J. Wörner, D. M. Villeneuve, and P. B. Corkum, “Probing the Spatial Structure of a Molecular Attosecond Electron Wave Packet Using Shaped Recollision Trajectories,” *Physical Review Letters*, vol. 107, p. 093004, Aug. 2011.
- [11] P. Eckle, A. N. Pfeiffer, C. Cirelli, A. Staudte, R. Dörner, H. G. Muller, M. Büttiker, and U. Keller, “Attosecond Ionization and Tunneling Delay Time Measurements in Helium,” *Science*, vol. 322, pp. 1525–1529, Dec. 2008.
- [12] J. Mauritsson, T. Remetter, M. Swoboda, K. Klünder, A. LHuillier, K. J. Schafer, O. Ghafur, F. Kelkensberg, W. Siu, P. Johnsson, M. Vrakking, I. Znakovskaya, T. Uphues, S. Zherebtsov, M. Kling, F. Lépine, E. Benedetti, F. Ferrari, G. Sansone, and M. Nisoli, “Attosecond Electron Spectroscopy Using a Novel Interferometric Pump-Probe Technique,” *Physical Review Letters*, vol. 105, p. 053001, July 2010.
- [13] M. Uiberacker, T. Uphues, M. Schultze, A. J. Verhoef, V. Yakovlev, M. F. Kling, J. Rauschenberger, M. Lezius, K. L. Kompa, H. Muller, M. J. J. Vrakking, and S. Hendel, “Attosecond real-time observation of electron tunnelling in atoms,” *Nature*, vol. 446, no. 7136, pp. 627–632, 2007.
- [14] L. Belshaw, F. Calegari, M. J. Duffy, A. Trabatttoni, L. Poletto, M. Nisoli, and J. B. Greenwood, “Observation of Ultrafast Charge Migration in an Amino Acid,” *The Journal of Physical Chemistry Letters*, vol. 3, pp. 3751–3754, 2012.
- [15] M. Gertsvolf, M. Spanner, D. M. Rayner, and P. B. Corkum, “Demonstration of attosecond ionization dynamics inside transparent solids,” *Journal of Physics B: Atomic, Molecular and Optical Physics*, vol. 43, p. 131002, July 2010.
- [16] T. H. Maiman, “Stimulated Optical Radiation in Ruby,” *Nature*, vol. 187, no. 4736, pp. 493 – 494, 1960.
- [17] R. W. Boyd, *Nonlinear Optics*. Academic Press, Elsevier, 3rd ed., 2008.
- [18] J. C. Diels and W. Rudolph, *Ultrashort Laser Pulse Phenomena*. Academic Press, Elsevier, 2nd ed., 2006.
- [19] G. Sansone, E. Benedetti, F. Calegari, C. Vozzi, L. Avaldi, R. Flammini, L. Poletto, P. Villoresi, C. Altucci, R. Velotta, S. Stagira, S. De Silvestri, and M. Nisoli, “Isolated single-cycle attosecond pulses,” *Science*, vol. 314, pp. 443–446, Oct. 2006.
- [20] A. L. Cavalieri, E. Goulielmakis, B. Horvath, W. Helml, M. Schultze, M. Fiess, V. Pervak, L. Veisz, V. S. Yakovlev, M. Uiberacker, A. Apolonski, F. Krausz, and R. Kienberger, “Intense 1.5-cycle near infrared laser waveforms and their use for the generation of ultra-broadband soft-x-ray harmonic continua,” *New Journal of Physics*, vol. 9, pp. 1–12, July 2007.
- [21] M. Fiess, *Advancing attosecond metrology*. PhD thesis, Ludwig-Maximilians Universität München, 2010.
- [22] W. Schweinberger, A. Sommer, E. M. Bothschafter, J. Li, F. Krausz, R. Kienberger, and M. Schultze, “Waveform-controlled near-single-cycle milli-joule laser pulses generate sub-10 nm extreme ultraviolet continua,” *Optics Letters*, vol. 37, no. 17, pp. 3573–3575, 2012.

- 
- [23] T. Fuji, J. Rauschenberger, C. Gohle, A. Apolonski, T. Udem, V. S. Yakovlev, G. Tempea, T. W. Hänsch, and F. Krausz, “Attosecond control of optical waveforms,” *New Journal of Physics*, vol. 7, pp. 116–116, May 2005.
- [24] T. Fuji, J. Rauschenberger, A. Apolonski, V. S. Yakovlev, G. Tempea, T. Udem, C. Gohle, T. W. Hänsch, W. Lehnert, M. Scherer, and F. Krausz, “Monolithic carrier-envelope phase-stabilization scheme,” *Optics Letters*, vol. 30, pp. 332–334, Feb. 2005.
- [25] D. Strickland and G. Mourou, “Compression of amplified chirped optical pulses,” *Optics Communications*, vol. 56, no. 3, pp. 219–221, 1985.
- [26] V. Pervak, A. V. Tikhonravov, M. K. Trubetskov, S. Naumov, F. Krausz, and A. Apolonski, “1.5-octave chirped mirror for pulse compression down to sub-3 fs,” *Applied Physics B*, vol. 87, pp. 5–12, Oct. 2007.
- [27] T. Udem, R. Holzwarth, and T. W. Hänsch, “Optical frequency metrology,” *Nature*, vol. 416, pp. 233–7, Mar. 2002.
- [28] L. Xu, C. Spielmann, A. Poppe, T. Brabec, F. Krausz, and T. W. Hänsch, “Route to phase control of ultrashort light pulses,” *Optics Letters*, vol. 21, pp. 2008–2010, Dec. 1996.
- [29] A. Apolonski, A. Poppe, G. Tempea, C. Spielmann, T. Udem, R. Holzwarth, T. W. Hänsch, and F. Krausz, “Controlling the phase evolution of few-cycle light pulses,” *Physical Review Letters*, vol. 85, pp. 740–743, July 2000.
- [30] J. Rauschenberger, T. Fuji, M. Hentschel, A. J. Verhoef, T. Udem, C. Gohle, T. W. Hänsch, and F. Krausz, “Carrier-envelope phase-stabilized amplifier system,” *Laser Physics Letters*, vol. 3, pp. 37–42, Jan. 2006.
- [31] A. Baltuška, M. Uiberacker, E. Goulielmakis, R. Kienberger, V. Yakovlev, T. Udem, T. W. Hänsch, and F. Krausz, “Phase-controlled amplification of few-cycle laser pulses,” *Selected Topics in . . .*, vol. 9, no. 4, pp. 972–989, 2003.
- [32] M. Takeda, H. Ina, and S. Kobayashi, “Fourier-transform method of fringe-pattern analysis for computer-based topography and interferometry,” *Journal of the Optical Society of America*, vol. 72, pp. 156–160, Jan. 1982.
- [33] T. Wittmann, B. Horvath, W. Helml, M. G. Schätzel, X. Gu, A. L. Cavalieri, G. G. Paulus, and R. Kienberger, “Single-shot carrier-envelope phase measurement of few-cycle laser pulses,” *Nature Physics*, vol. 5, pp. 357–362, Apr. 2009.
- [34] A. Wirth, *Attosecond Transient Absorption Spectroscopy*. PhD thesis, Ludwig-Maximilians Universität München, 2011.
- [35] M. T. Hassan, A. Wirth, I. Grguraš, A. Moulet, T. T. Luu, J. Gagnon, V. Pervak, and E. Goulielmakis, “Invited article: attosecond photonics: synthesis and control of light transients,” *The Review of Scientific Instruments*, vol. 83, p. 111301, Nov. 2012.
- [36] S. Kahra, G. Leschhorn, M. Kowalewski, A. Schiffrin, E. M. Bothschafter, W. Fuß, R. de Vivie-Riedle, R. Ernstorfer, F. Krausz, R. Kienberger, and T. Schaeetz, “A molecular conveyor belt by controlled delivery of single molecules into ultrashort laser pulses,” *Nature Physics*, vol. 8, pp. 238–242, Feb. 2012.

- [37] E. M. Bothschafter, “Collinear Generation and Characterization of Ultrashort UV and XUV Laser Pulses.” , Diploma thesis, Universität Stuttgart, 2009.
- [38] I. Kozma, P. Baum, S. Lochbrunner, and E. Riedle, “Widely tunable sub-30 fs ultraviolet pulses by chirped sum frequency mixing,” *Optics Express*, vol. 11, pp. 3110–3115, Nov. 2003.
- [39] P. Baum, S. Lochbrunner, and E. Riedle, “Tunable sub-10-fs ultraviolet pulses generated by achromatic frequency doubling,” *Optics Letters*, vol. 29, pp. 1686–1688, July 2004.
- [40] J. Darginavičius, G. Tamošauskas, G. Valiulis, and a. Dubietis, “Broadband four-wave optical parametric amplification in bulk isotropic media in the ultraviolet,” *Optics Communications*, vol. 282, pp. 2995–2999, July 2009.
- [41] S. Backus, J. Peatross, Z. Zeek, A. R. Rundquist, G. Taft, M. M. Murnane, and H. C. Kapteyn, “16-fs, 1-microJ ultraviolet pulses generated by third-harmonic conversion in air.,” *Optics Letters*, vol. 21, pp. 665–667, May 1996.
- [42] C. Durfee III, A. R. Rundquist, S. Backus, C. Herne, M. M. Murnane, and H. C. Kapteyn, “Phase matching of high-order harmonics in hollow waveguides,” *Physical Review Letters*, vol. 83, no. 11, pp. 2187–2190, 1999.
- [43] N. Aközbek, A. Iwasaki, A. Becker, M. Scalora, S. Chin, and C. Bowden, “Third-Harmonic Generation and Self-Channeling in Air Using High-Power Femtosecond Laser Pulses,” *Physical Review Letters*, vol. 89, p. 143901, Sept. 2002.
- [44] T. Fuji, T. Horio, and T. Suzuki, “Generation of 12 fs deep-ultraviolet pulses by four-wave mixing through filamentation in neon gas.,” *Optics Letters*, vol. 32, pp. 2481–2483, Sept. 2007.
- [45] K. Kosma, S. A. Trushin, W. E. Schmid, and W. Fuss, “Vacuum ultraviolet pulses of 11 fs from fifth-harmonic generation of a Ti:sapphire laser.,” *Optics Letters*, vol. 33, pp. 723–725, Apr. 2008.
- [46] U. Graf, M. Fiess, M. Schultze, R. Kienberger, F. Krausz, and E. Goulielmakis, “Intense few-cycle light pulses in the deep ultraviolet,” *Optics Express*, vol. 16, pp. 18956–18963, Nov. 2008.
- [47] F. Reiter, U. Graf, M. Schultze, W. Schweinberger, H. Schröder, N. Karpowicz, A. M. Azzeer, R. Kienberger, F. Krausz, and E. Goulielmakis, “Generation of sub-3 fs pulses in the deep ultraviolet.,” *Optics Letters*, vol. 35, pp. 2248–2250, July 2010.
- [48] J. A. Armstrong, N. Bloembergen, J. Ducuing, and P. S. Pershan, “Interactions between Light Waves in a Nonlinear Dielectric,” *Physical Review*, vol. 127, no. 6, pp. 1918–1939, 1962.
- [49] E. M. Bothschafter, A. Schiffrin, V. S. Yakovlev, A. M. Azzeer, F. Krausz, R. Ernstorfer, and R. Kienberger, “Collinear generation of ultrashort UV and XUV pulses.,” *Optics Express*, vol. 18, pp. 9173–80, Apr. 2010.

- 
- [50] A. McPherson, G. Gibson, H. Jara, U. Johann, T. S. Luk, I. A. McIntyre, K. Boyer, and C. K. Rhodes, “Studies of multiphoton production of vacuum-ultraviolet,” *Journal of the Optical Society of America B*, vol. 4, no. 4, pp. 595–601, 1987.
- [51] K. C. Kulander, K. J. Schafer, and J. L. Krause, “Theoretical Model for Intense Field High-Order Harmonic Generation in Rare Gases,” *Laser Physics*, vol. 3, no. 2, pp. 359–364, 1993.
- [52] M. Lewenstein, P. Balcou, M. Y. Ivanov, A. L’Huillier, and P. B. Corkum, “Theory of high-harmonic generation by low-frequency laser fields,” *Physical Review A*, vol. 49, no. 3, pp. 2117–2132, 1994.
- [53] P. B. Corkum, “Plasma perspective on strong field multiphoton ionization,” *Physical Review Letters*, vol. 71, no. 13, pp. 1994–1997, 1993.
- [54] Y. Mairesse, A. de Bohan, L. J. Frasinski, H. Merdji, L. C. Dinu, P. Monchicourt, P. Breger, M. Kovacev, R. Taïeb, B. Carré, H. G. Muller, P. Agostini, and P. Salières, “Attosecond synchronization of high-harmonic soft x-rays,” *Science*, vol. 302, pp. 1540–3, Nov. 2003.
- [55] K. Varju, P. Johnsson, J. Mauritsson, A. L’Huillier, and R. Lopez-Martens, “Physics of attosecond pulses produced via high harmonic generation,” *American Journal of Physics*, vol. 77, no. 5, pp. 389–395, 2009.
- [56] P. B. Corkum, N. H. Burnett, and M. Y. Ivanov, “Subfemtosecond pulses,” *Optics Letters*, vol. 19, no. 22, pp. 1870–1872, 1994.
- [57] C. Altucci, C. Delfin, L. Roos, M. B. Gaarde, A. L’Huillier, I. Mercer, T. Starczewski, and C.-G. Wahlström, “Frequency-resolved time-gated high-order harmonics,” *Physical Review A*, vol. 58, pp. 3934–3941, Nov. 1998.
- [58] O. Tcherbakoff, E. Mével, D. Descamps, J. Plumridge, and E. Constant, “Time-gated high-order harmonic generation,” *Physical Review A*, vol. 68, p. 043804, Oct. 2003.
- [59] I. J. Sola, E. Mével, L. Elouga, E. Constant, V. Strelkov, L. Poletto, P. Villoresi, E. Benedetti, J.-P. Caumes, S. Stagira, C. Vozzi, G. Sansone, and M. Nisoli, “Controlling attosecond electron dynamics by phase-stabilized polarization gating,” *Nature Physics*, vol. 2, pp. 319–322, Apr. 2006.
- [60] H. Mashiko, S. Gilbertson, C. Li, S. D. Khan, M. M. Shakya, E. Moon, and Z. Chang, “Double Optical Gating of High-Order Harmonic Generation with Carrier-Envelope Phase Stabilized Lasers,” *Physical Review Letters*, vol. 100, p. 103906, Mar. 2008.
- [61] X. Feng, S. Gilbertson, H. Mashiko, H. Wang, S. D. Khan, M. Chini, Y. Wu, K. Zhao, and Z. Chang, “Generation of Isolated Attosecond Pulses with 20 to 28 Femtosecond Lasers,” *Physical Review Letters*, vol. 103, pp. 28–31, Oct. 2009.
- [62] M. J. Abel, T. Pfeifer, P. M. Nagel, W. Boutu, M. J. Bell, C. P. Steiner, D. Neumark, and S. R. Leone, “Isolated attosecond pulses from ionization gating of high-harmonic emission,” *Chemical Physics*, vol. 366, pp. 9–14, Dec. 2009.

- [63] E. Goulielmakis, M. Schultze, M. Hofstetter, V. S. Yakovlev, J. Gagnon, M. Uiberacker, A. L. Aquila, E. M. Gullikson, D. T. Attwood, R. Kienberger, F. Krausz, and U. Kleineberg, “Single-cycle nonlinear optics,” *Science*, vol. 320, pp. 1614–1617, June 2008.
- [64] M. Schultze, E. M. Bothschafter, A. Sommer, S. Holzner, W. Schweinberger, M. Fiess, M. Hofstetter, R. Kienberger, V. Apalkov, V. S. Yakovlev, M. I. Stockman, and F. Krausz, “Controlling dielectrics with the electric field of light.,” *Nature*, vol. 493, pp. 75–78, Jan. 2013.
- [65] P. Antoine, A. L’Huillier, and M. Lewenstein, “Attosecond Pulse Trains Using High-Order Harmonics.,” *Physical Review Letters*, vol. 77, pp. 1234–1237, Aug. 1996.
- [66] P. Salieres, T. Ditmire, K. S. Budil, M. D. Perry, and A. L’Huillier, “Spatial profiles of high-order harmonics generated by a femtosecond Cr: LiSAF laser,” *Journal of Physics B*, vol. 27, pp. 217–222, 1994.
- [67] R. Trebino, K. W. DeLong, D. N. Fittinghoff, J. N. Sweetser, M. A. Krumbugel, B. A. Richman, and D. J. Kane, “Measuring ultrashort laser pulses in the time-frequency domain using frequency-resolved optical gating,” *Review of Scientific Instruments*, vol. 68, no. 9, p. 3277, 1997.
- [68] A. Baltuška, M. S. Pshenichnikov, and D. A. Wiersma, “Amplitude and phase characterization of 4.5-fs pulses by frequency-resolved optical gating.,” *Optics Letters*, vol. 23, pp. 1474–1476, Sept. 1998.
- [69] J. N. Sweetser, D. N. Fittinghoff, and R. Trebino, “Transient-grating frequency-resolved optical gating.,” *Optics Letters*, vol. 22, pp. 519–21, Apr. 1997.
- [70] T. E. Glover, R. W. Schoenlein, A. H. Chin, and C. V. Shank, “Observation of laser assisted photoelectric effect and femtosecond high order harmonic radiation.,” *Physical Review Letters*, vol. 76, pp. 2468–2471, Apr. 1996.
- [71] Y. Nabekawa, T. Shimizu, T. Okino, K. Furusawa, H. Hasegawa, K. Yamanouchi, and K. Midorikawa, “Interferometric Autocorrelation of an Attosecond Pulse Train in the Single-Cycle Regime,” *Physical Review Letters*, vol. 97, p. 153904, Oct. 2006.
- [72] P. M. Paul, E. S. Toma, P. Breger, G. Mullot, F. Audebert, P. Balcou, H. G. Muller, and P. Agostini, “Observation of a train of attosecond pulses from high harmonic generation,” *Science*, vol. 292, pp. 1689–92, June 2001.
- [73] J. Itatani, F. Quéré, G. Yudin, M. Ivanov, F. Krausz, and P. B. Corkum, “Attosecond Streak Camera,” *Physical Review Letters*, vol. 88, pp. 1–4, Apr. 2002.
- [74] J. Gagnon, E. Goulielmakis, and V. Yakovlev, “The accurate FROG characterization of attosecond pulses from streaking measurements,” *Applied Physics B*, vol. 92, pp. 25–32, June 2008.
- [75] V. Yakovlev, J. Gagnon, N. Karpowicz, and F. Krausz, “Attosecond Streaking Enables the Measurement of Quantum Phase,” *Physical Review Letters*, vol. 105, pp. 3–6, Aug. 2010.



- 
- [76] R. Kienberger, M. Hentschel, M. Uiberacker, C. Spielmann, M. Kitzler, A. Scrinzi, M. Wieland, T. Westerwalbesloh, U. Kleineberg, U. Heinzmann, M. Drescher, and F. Krausz, “Steering attosecond electron wave packets with light.,” *Science*, vol. 297, pp. 1144–1148, Aug. 2002.
- [77] F. Quéré, J. Itatani, G. Yudin, and P. B. Corkum, “Attosecond Spectral Shearing Interferometry,” *Physical Review Letters*, vol. 90, p. 073902, Feb. 2003.
- [78] Y. Mairesse and F. Quéré, “Frequency-resolved optical gating for complete reconstruction of attosecond bursts,” *Physical Review A*, vol. 71, p. 011401, Jan. 2005.
- [79] A. Laubereau and W. Kaiser, “Vibrational dynamics of liquids and solids investigated by picosecond light pulses,” *Reviews of Modern Physics*, vol. 50, no. 3, pp. 607–665, 1978.
- [80] T. Dekorsy, G. C. Cho, and H. Kurz, “Coherent phonons in condensed media,” in *Light Scattering in Solids VIII* (M. Cardona and G. Güntherodt, eds.), vol. 76, pp. 169–209, Berlin, Heidelberg: Springer, 76 ed., 2000.
- [81] K. Ishioka and O. V. Misochko, “Coherent Lattice Oscillations in Solids and Their Optical Control Part I . Fundamentals and Optical Detection,” in *Progress in Ultrafast Intense Laser Science* (K. Yamanouchi, A. Giullietti, and K. Ledingham, eds.), pp. 23–64, Berlin: Springer, v ed., 2010.
- [82] Y. Matsumoto and K. Watanabe, “Coherent Vibrations of Adsorbates Induced by Femtosecond Laser Excitation,” *Chemical Reviews*, vol. 106, pp. 4234–60, Oct. 2006.
- [83] A. V. Kuznetsov and C. J. Stanton, “Theory of coherent phonon oscillations in semiconductors,” *Physical Review Letters*, vol. 73, no. 24, pp. 3243–3246, 1994.
- [84] H. J. Zeiger, J. Vidal, T. K. Cheng, and E. P. Ippen, “Theory for displacive excitation of coherent phonons,” *Physical Review B*, 1992.
- [85] D. M. Riffe and A. J. Sabbah, “Coherent excitation of the optic phonon in Si: transiently stimulated Raman scattering with a finite-lifetime electronic excitation,” *Physical Review B*, vol. 76, pp. 1–12, 2007.
- [86] R. Merlin, “Generating coherent THz phonons with light pulses,” *Solid State Communications*, vol. 102, no. 2-3, pp. 207–220, 1997.
- [87] K. Sokolowski-Tinten, C. Blome, J. Blums, A. Cavalleri, C. Dietrich, A. Tarasevitch, I. Uschmann, E. Förster, M. Kammler, M. Horn-von Hoegen, and D. von der Linde, “Femtosecond X-ray measurement of coherent lattice vibrations near the Lindemann stability limit.,” *Nature*, vol. 422, pp. 287–9, Mar. 2003.
- [88] E. Seres, J. Seres, and C. Spielmann, “Time resolved spectroscopy with femtosecond soft-x-ray pulses,” *Applied Physics A*, vol. 96, pp. 43–50, Mar. 2009.
- [89] T. Brabec and F. Krausz, “Nonlinear Optical Pulse Propagation in the Single-Cycle Regime,” *Physical Review Letters*, vol. 78, pp. 3282–3285, Apr. 1997.
- [90] V. Apalkov and M. I. Stockman, “Theory of dielectric nanofilms in strong ultrafast optical fields,” *Physical Review B*, vol. 86, p. 165118, Oct. 2012.



- [91] S. Y. Kruchinin, M. Korbman, and V. S. Yakovlev, “Theory of strong-field injection and control of photocurrent in dielectrics and wide band gap semiconductors,” *Physical Review B*, vol. 87, p. 115201, Mar. 2013.
- [92] L. A. J. Garvie, P. Rez, J. R. Alvarez, P. R. Buseck, A. J. Craven, and R. Brydson, “Bonding in alpha-quartz (SiO<sub>2</sub>): A view of the unoccupied states,” *American Mineralogist*, vol. 85, no. 1, pp. 732–738, 2000.
- [93] D. K. Ferry, “Impact ionization in silicon dioxide,” *Solid State Communications*, vol. 18, no. 7, pp. 1051–1053, 1976.
- [94] D. Du, X. Liu, G. Korn, J. Squier, and G. Mourou, “Laser-induced breakdown from 7 ns to 150 fs by impact ionization in SiO<sub>2</sub> with pulse widths,” *Applied Physics Letters*, vol. 64, no. 23, pp. 3071–3073, 1994.
- [95] B. C. Stuart, M. D. Feit, A. M. Rubenchik, B. W. Shore, and M. D. Perry, “Laser-induced damage in dielectrics with nanosecond to subpicosecond pulses,” *Physical Review Letters*, vol. 74, no. 12, pp. 2248–2251, 1995.
- [96] M. Lenzner, J. Krüger, S. Sartania, Z. Cheng, C. Spielmann, G. Mourou, W. Kautek, and F. Krausz, “Femtosecond Optical Breakdown in Dielectrics,” *Physical Review Letters*, vol. 80, pp. 4076–4079, May 1998.
- [97] M. Li, S. Menon, J. Nibarger, and G. Gibson, “Ultrafast Electron Dynamics in Femtosecond Optical Breakdown of Dielectrics,” *Physical Review Letters*, vol. 82, pp. 2394–2397, Mar. 1999.
- [98] A.-C. Tien, S. Backus, H. Kapteyn, M. Murnane, and G. Mourou, “Short-Pulse Laser Damage in Transparent Materials as a Function of Pulse Duration,” *Physical Review Letters*, vol. 82, pp. 3883–3886, May 1999.
- [99] M. Mero, J. Liu, W. Rudolph, D. Ristau, and K. Starke, “Scaling laws of femtosecond laser pulse induced breakdown in oxide films,” *Physical Review B*, vol. 71, p. 115109, Mar. 2005.
- [100] B. Chimier, O. Utéza, N. Sanner, M. Sentis, T. Itina, P. Lassonde, F. Légaré, F. Vidal, and J. C. Kieffer, “Damage and ablation thresholds of fused-silica in femtosecond regime,” *Physical Review B*, vol. 84, p. 094104, Sept. 2011.
- [101] A. Kaiser, B. Rethfeld, M. Vicanek, and G. Simon, “Microscopic processes in dielectrics under irradiation by subpicosecond laser pulses,” *Physical Review B*, vol. 61, pp. 11437–11450, May 2000.
- [102] B. Rethfeld, “Unified Model for the Free-Electron Avalanche in Laser-Irradiated Dielectrics,” *Physical Review Letters*, vol. 92, p. 187401, May 2004.
- [103] B. Rethfeld, “Free-electron generation in laser-irradiated dielectrics,” *Physical Review B*, vol. 73, p. 035101, Jan. 2006.
- [104] T. Otobe, M. Yamagiwa, J.-I. Iwata, K. Yabana, T. Nakatsukasa, and G. Bertsch, “First-principles electron dynamics simulation for optical breakdown of dielectrics under an intense laser field,” *Physical Review B*, vol. 77, pp. 1–5, Apr. 2008.

- 
- [105] B. Rethfeld, O. Brenk, N. Medvedev, H. Kruttsch, and D. H. H. Hoffmann, “Interaction of dielectrics with femtosecond laser pulses: application of kinetic approach and multiple rate equation,” *Applied Physics A*, vol. 101, pp. 19–25, June 2010.
- [106] K. Yabana, T. Sugiyama, Y. Shinohara, T. Otobe, and G. F. Bertsch, “Time-dependent density functional theory for strong electromagnetic fields in crystalline solids,” *Physical Review B*, vol. 85, p. 045134, Jan. 2012.
- [107] C. B. Schaffer, A. Brodeur, and E. Mazur, “Laser-induced breakdown and damage in bulk transparent materials induced by tightly focused femtosecond laser pulses,” *Measurement Science and Technology*, vol. 12, pp. 1784–1794, Nov. 2001.
- [108] T. V. Kononenko, S. Schöneiseffen, V. I. Konov, and F. Dausinger, “Effect of laser pulse repetition frequency on the optical breakdown threshold of quartz glass,” *Quantum Electronics*, vol. 43, pp. 731–734, Aug. 2013.
- [109] P. Audebert, P. Daguzan, A. D. Santos, J. P. Geindre, S. Guizard, G. Hamoniaux, K. Krastev, P. Martin, and A. Antonetti, “Space-Time Observation of an Electron Gas in SiO<sub>2</sub>,” *Physical Review Letters*, vol. 73, no. 14, pp. 1990–1993, 1994.
- [110] P. Martin, S. Guizard, P. Daguzan, G. Petite, P. D’Oliveira, P. Meynadier, and M. Perdrix, “Subpicosecond study of carrier trapping dynamics in wide-band-gap crystals,” *Physical Review B*, vol. 55, pp. 5799–5810, Mar. 1997.
- [111] F. Quéré, S. Guizard, and P. Martin, “Time-resolved study of laser-induced breakdown in dielectrics,” *EPL (Europhysics Letters)*, vol. 56, pp. 138–144, 2001.
- [112] V. V. Temnov, K. Sokolowski-Tinten, P. Zhou, and D. von der Linde, “Femtosecond time-resolved interferometric microscopy,” *Applied Physics A: Materials Science & Processing*, vol. 78, pp. 483–489, Mar. 2004.
- [113] V. V. Temnov, K. Sokolowski-Tinten, P. Zhou, A. El-Khamhawy, and D. von der Linde, “Multiphoton Ionization in Dielectrics: Comparison of Circular and Linear Polarization,” *Physical Review Letters*, vol. 97, pp. 1–4, Dec. 2006.
- [114] S. W. Winkler, I. M. Burakov, R. Stoian, N. M. Bulgakova, A. Husakou, A. Mermillod-Blondin, A. Rosenfeld, D. Ashkenasi, and I. V. Hertel, “Transient response of dielectric materials exposed to ultrafast laser radiation,” *Applied Physics A*, vol. 84, pp. 413–422, July 2006.
- [115] J. R. Gulley, S. W. Winkler, W. M. Dennis, C. M. Liebig, and R. Stoian, “Interaction of ultrashort-laser pulses with induced undercritical plasmas in fused silica,” *Physical Review A*, vol. 85, p. 013808, Jan. 2012.
- [116] N. Dudovich, J. Levesque, O. Smirnova, D. Zeidler, D. Comtois, M. Ivanov, D. Villeneuve, and P. B. Corkum, “Attosecond Temporal Gating with Elliptically Polarized Light,” *Physical Review Letters*, vol. 97, p. 253903, Dec. 2006.
- [117] A. Mitrofanov, A. J. Verhoef, E. Serebryannikov, J. Lumeau, L. Glebov, A. Zheltikov, and A. Baltuška, “Optical Detection of Attosecond Ionization Induced by a Few-Cycle Laser

- Field in a Transparent Dielectric Material,” *Physical Review Letters*, vol. 106, pp. 1–4, Apr. 2011.
- [118] T. Hertel, E. Knoesel, M. Wolf, and G. Ertl, “Ultrafast electron dynamics at Cu(111): Response of an electron gas to optical excitation.,” *Physical Review Letters*, vol. 76, pp. 535–538, Jan. 1996.
- [119] F. Schmitt, P. S. Kirchmann, U. Bovensiepen, R. G. Moore, L. Rettig, M. Krenz, J.-H. Chu, N. Ru, L. Perfetti, D. H. Lu, M. Wolf, I. R. Fisher, and Z.-X. Shen, “Transient electronic structure and melting of a charge density wave in TbTe<sub>3</sub>,” *Science*, vol. 321, pp. 1649–1652, Sept. 2008.
- [120] R. Ernstorfer, M. Harb, C. T. Hebeisen, G. Sciaini, T. Dartigalongue, and R. J. D. Miller, “The formation of warm dense matter: experimental evidence for electronic bond hardening in gold.,” *Science*, vol. 323, pp. 1033–7, Feb. 2009.
- [121] D. M. Fritz, D. A. Reis, B. Adams, R. A. Akre, J. Arthur, C. Blome, P. H. Bucksbaum, A. L. Cavalieri, S. Engemann, S. Fahy, R. W. Falcone, P. H. Fuoss, K. J. Gaffney, M. J. George, J. Hajdu, M. P. Hertlein, P. B. Hillyard, M. Horn-von Hoegen, M. Kammiller, J. Kaspar, R. Kienberger, P. Krejčík, S. H. Lee, A. M. Lindenberg, B. McFarland, D. Meyer, T. Montagne, E. D. Murray, A. J. Nelson, M. Nicoul, R. Pahl, J. Rudati, H. Schlarb, D. P. Siddons, K. Sokolowski-Tinten, T. Tschentscher, D. von der Linde, and J. B. Hastings, “Ultrafast bond softening in bismuth: mapping a solid’s interatomic potential with X-rays.,” *Science*, vol. 315, pp. 633–636, Feb. 2007.
- [122] T. Elsaesser and M. Woerner, “Photoinduced structural dynamics of polar solids studied by femtosecond X-ray diffraction.,” *Acta crystallographica. Section A, Foundations of crystallography*, vol. 66, pp. 168–78, Mar. 2010.
- [123] D. Boschetto, E. Gamaly, A. Rode, B. Luther-Davies, D. Glijer, T. Garl, O. Albert, A. Rousse, and J. Etchepare, “Small Atomic Displacements Recorded in Bismuth by the Optical Reflectivity of Femtosecond Laser-Pulse Excitations,” *Physical Review Letters*, vol. 100, pp. 7–10, Jan. 2008.
- [124] M. Hase, M. Kitajima, A. M. Constantinescu, and H. Petek, “The birth of a quasiparticle in silicon observed in time frequency space,” *Nature*, vol. 426, no. November, pp. 51–54, 2003.
- [125] K. Ishioka, M. Hase, M. Kitajima, L. Wirtz, A. Rubio, and H. Petek, “Ultrafast electron-phonon decoupling in graphite,” *Physical Review B*, vol. 77, pp. 1–4, Mar. 2008.
- [126] E. S. Zijlstra, L. Tatarinova, and M. E. Garcia, “Laser-induced phonon-phonon interactions in bismuth,” *Physical Review B*, vol. 74, p. 220301, Dec. 2006.
- [127] E. M. Bothschafter, A. Paarmann, E. S. Zijlstra, N. Karpowicz, M. E. Garcia, R. Kienberger, and R. Ernstorfer, “Ultrafast Evolution of the Excited-State Potential Energy Surface of TiO<sub>2</sub> Single Crystals Induced by Carrier Cooling,” *Physical Review Letters*, vol. 110, p. 067402, Feb. 2013.

- [128] A. J. Taylor, D. J. Erskine, and C. L. Tang, "Femtosecond vibrational relaxation of large organic molecules," *Chemical physics letters*, vol. 103, no. 5, pp. 430–435, 1984.
- [129] D. W. Bahnemann, M. Hilgendorff, and R. Memming, "Charge Carrier Dynamics at TiO<sub>2</sub> Particles : Reactivity of Free and Trapped Holes," *Journal of Physical Chemistry B*, vol. 101, no. 21, pp. 4265–4275, 1997.
- [130] A. Fujishima, X. Zhang, and D. Tryk, "TiO<sub>2</sub> photocatalysis and related surface phenomena," *Surface Science Reports*, vol. 63, pp. 515–582, Dec. 2008.
- [131] A. J. Cowan, J. Tang, W. Leng, J. R. Durrant, and D. R. Klug, "Water splitting by nanocrystalline TiO<sub>2</sub> in a complete photoelectrochemical cell exhibits efficiencies limited by charge recombination," *The Journal of Physical Chemistry C*, vol. 114, no. 9, pp. 4208–4214, 2010.
- [132] A. Hagfeldt and M. Grätzel, "Molecular photovoltaics," *Accounts of Chemical Research*, vol. 33, no. 5, pp. 269–277, 2000.
- [133] K. Nakata, T. Ochiai, T. Murakami, and A. Fujishima, "Photoenergy conversion with TiO<sub>2</sub> photocatalysis: New materials and recent applications," *Electrochimica Acta*, vol. 84, pp. 103–111, Dec. 2012.
- [134] J. Muscat, V. Swamy, and N. Harrison, "First-principles calculations of the phase stability of TiO<sub>2</sub>," *Physical Review B*, vol. 65, p. 224112, June 2002.
- [135] M. Cardona and G. Harbeke, "Optical properties and band structure of wurtzite-type crystals and rutile," *Physical Review*, vol. 573, no. 1959, 1965.
- [136] J. Pascual, J. Camassel, and H. Mathieu, "Fine structure in the intrinsic absorption edge of TiO<sub>2</sub>," *Physical Review B*, vol. 18, no. 10, pp. 5606–5614, 1978.
- [137] A. Amtout and R. Leonelli, "Resonant Raman scattering from excitons in TiO<sub>2</sub>," *Physical Review B*, vol. 46, no. 23, pp. 550–553, 1992.
- [138] S. Wall, D. Wegkamp, L. Foglia, K. Appavoo, J. Nag, R. F. Haglund, J. Stähler, and M. Wolf, "Ultrafast changes in lattice symmetry probed by coherent phonons.," *Nature Communications*, vol. 3, p. 721, Jan. 2012.
- [139] C. Lee, P. Ghosez, and X. Gonze, "Lattice dynamics and dielectric properties of incipient ferroelectric TiO<sub>2</sub> rutile," *Physical Review B*, vol. 50, no. 18, pp. 13379–13387, 1994.
- [140] J. Zhang, M. Li, Z. Feng, J. Chen, and C. Li, "UV Raman spectroscopic study on TiO<sub>2</sub>. I. Phase transformation at the surface and in the bulk.," *The Journal of Physical Chemistry B*, vol. 110, pp. 927–35, Jan. 2006.
- [141] T. Lan, X. Tang, and B. Fultz, "Phonon anharmonicity of rutile TiO<sub>2</sub> studied by Raman spectrometry and molecular dynamics simulations," *Physical Review B*, vol. 85, p. 094305, Mar. 2012.
- [142] T. Nomoto, A. Sasahara, and H. Onishi, "Optically excited near-surface phonons of TiO<sub>2</sub> (110) observed by fourth-order coherent Raman spectroscopy.," *The Journal of chemical physics*, vol. 131, p. 084703, Aug. 2009.

- [143] K. Ishioka and H. Petek, “Raman generation of coherent phonons of anatase and rutile TiO<sub>2</sub> photoexcited at fundamental absorption edges,” *Physical Review B*, vol. 86, p. 205201, Nov. 2012.
- [144] E. Hendry, F. Wang, J. Shan, T. Heinz, and M. Bonn, “Electron transport in TiO<sub>2</sub> probed by THz time-domain spectroscopy,” *Physical Review B*, vol. 69, pp. 1–4, Feb. 2004.
- [145] W. A. Tisdale, K. J. Williams, B. A. Timp, D. J. Norris, E. S. Aydil, and X.-Y. Zhu, “Hot-electron transfer from semiconductor nanocrystals,” *Science*, vol. 328, pp. 1543–1547, June 2010.
- [146] V. P. Zhukov and E. V. Chulkov, “Ab initio approach to the excited electron dynamics in rutile and anatase TiO<sub>2</sub>,” *Journal of Physics. Condensed matter*, vol. 22, p. 435802, Nov. 2010.
- [147] Z. Wang, J. Liu, R. Li, and Z. Xu, “Wavefront control to generate ultraviolet supercontinuum by filamentation of few-cycle laser pulses in argon,” *Optics Letters*, vol. 35, no. 2, pp. 163–165, 2010.
- [148] E. Yagi, R. R. Hasiguti, and M. Aono, “Electronic conduction above 4 K of slightly reduced oxygen-deficient rutile TiO(2-x),” *Physical Review B*, vol. 54, no. 11, pp. 7945–7956, 1996.
- [149] L. Chiodo, J. M. García-Lastra, A. Iacomino, S. Ossicini, J. Zhao, H. Petek, and A. Rubio, “Self-energy and excitonic effects in the electronic and optical properties of TiO<sub>2</sub> crystalline phases,” *Physical Review B*, vol. 82, p. 045207, July 2010.
- [150] P. I. Sorantin and K. Schwarz, “Chemical bonding in rutile-type compounds,” *Inorganic Chemistry*, vol. 31, no. 4, pp. 567–576, 1992.
- [151] M. Landmann, E. Rauls, and W. G. Schmidt, “The electronic structure and optical response of rutile, anatase and brookite TiO<sub>2</sub>,” *Journal of Physics. Condensed matter*, vol. 24, p. 195503, May 2012.
- [152] P. Blaha, K. Schwarz, G. K. H. Madsen, D. Kvasnicka, and J. Luitz, *Wien2k, an Augmented Plane wave + Local Orbitals Program for Calculating Crystal Properties*. Wien: Technische Universitaet Wien, Austria, 2001.
- [153] M. S. Diakhate, E. S. Zijlstra, and M. E. Garcia, “Quantum dynamical study of the amplitude collapse and revival of coherent A<sub>1g</sub> phonons in bismuth: a classical phenomenon?,” *Applied Physics A*, vol. 96, pp. 5–10, Mar. 2009.
- [154] E. M. Bothschafter, A. Paarmann, N. Karpowicz, E. S. Zijlstra, M. E. Garcia, F. Krausz, R. Kienberger, and R. Ernstorfer, “Interband excitation and carrier relaxation as displacive driving force for coherent phonons,” *EPJ Web of Conferences*, vol. 41, p. 02021, Mar. 2013.
- [155] C. Zener, “A theory of the electrical breakdown of solid dielectrics,” *Proceedings of the Royal Society of London. Series A*, vol. 145, no. 855, pp. 523–529, 1934.
- [156] G. H. Wannier, “Wave functions and effective Hamiltonian for Bloch electrons in an electric field,” *Physical Review*, vol. 117, no. 2, pp. 432–439, 1960.

- 
- [157] W. Franz, "Einfluss eines elektrischen Feldes auf eine optische Absorptionskante," *Zeitschrift für Naturforschung. A*, vol. 13, no. 6, pp. 484–489, 1958.
- [158] L. V. Keldysh, "Behaviour of non-metallic crystals in strong electric fields," *Soviet Physics, JETP*, vol. 6, no. 4, pp. 763–770, 1958.
- [159] E. Goulielmakis, Z.-H. Loh, A. Wirth, R. Santra, N. Rohringer, V. S. Yakovlev, S. Zherebtsov, T. Pfeifer, A. M. Azzeer, M. F. Kling, S. R. Leone, and F. Krausz, "Real-time observation of valence electron motion.," *Nature*, vol. 466, pp. 739–743, Aug. 2010.
- [160] M. Fiess, M. Schultze, E. Goulielmakis, B. Dennhardt, J. Gagnon, M. Hofstetter, R. Kienberger, and F. Krausz, "Versatile apparatus for attosecond metrology and spectroscopy.," *The Review of Scientific Instruments*, vol. 81, p. 093103, Sept. 2010.
- [161] M. Schultze, A. Wirth, I. Grguraš, M. Uiberacker, T. Uphues, A. J. Verhoef, J. Gagnon, M. Hofstetter, U. Kleineberg, E. Goulielmakis, and F. Krausz, "State-of-the-art attosecond metrology," *Journal of Electron Spectroscopy and Related Phenomena*, vol. 184, pp. 68–77, Apr. 2011.
- [162] R. López-Martens, K. Varjú, P. Johnsson, J. Mauritsson, Y. Mairesse, P. Salières, M. B. Gaarde, K. J. Schafer, A. Persson, S. Svanberg, C.-G. Wahlström, and A. L'Huillier, "Amplitude and Phase Control of Attosecond Light Pulses," *Physical Review Letters*, vol. 94, p. 033001, Jan. 2005.
- [163] T. Kita, T. Harada, N. Nakano, and H. Kuroda, "Rapid communications.," *Applied Optics*, vol. 25, pp. 512–513, Dec. 1986.
- [164] D. Li, G. M. Bancroft, M. Kasrai, M. E. Fleet, R. A. Secco, X. H. Feng, K. H. Tan, and B. X. Yang, "X-ray absorption spectroscopy of silicon dioxide (SiO<sub>2</sub>) polymorphs : The structural characterization of opal," *American Mineralogist*, vol. 79, pp. 622–632, 1994.
- [165] G. Duscher, R. Buczko, S. J. Pennycook, and S. T. Pantelides, "Core-hole effects on energy-loss near-edge structure.," *Ultramicroscopy*, vol. 86, pp. 355–62, Feb. 2001.
- [166] W. T. Pollard and R. A. Mathies, "Analysis of femtosecond dynamic absorption spectra of nonstationary states," *Annual Review of Physical Chemistry*, vol. 43, pp. 497–523, 1992.
- [167] N. Karpowicz, "Simple Attosecond Nonlinear Spectroscopy in Bulk Solids (private communication)," 2012.
- [168] M. Durach, A. Rusina, M. Kling, and M. I. Stockman, "Metallization of Nanofilms in Strong Adiabatic Electric Fields," *Physical Review Letters*, vol. 105, pp. 1–4, Aug. 2010.
- [169] G. P. Agrawal, *Nonlinear Fiber Optics*. Academic Press, Elsevier, 5 ed., 2013.
- [170] M. Sheik-Bahae, A. A. Said, T.-H. Wei, D. J. Hagan, and E. W. Van Stryland, "Sensitive measurement of optical nonlinearities using a single beam," *IEEE Journal of Quantum Electronics*, vol. 26, pp. 760–769, Apr. 1990.





# Danksagung

An dieser Stelle möchte ich mich bei all jenen bedanken, die zum Gelingen dieser Dissertation beigetragen haben und mich in vielerlei Hinsicht unterstützt haben.

Allen voran danke ich meinem Doktorvater Professor Reinhard Kienberger dafür, dass er mir die Möglichkeit gegeben hat, in einem wissenschaftlich wie menschlich einzigartigen Umfeld zu forschen. Ich bin ausserordentlich dankbar für die Betreuung dieser Arbeit, seinen stets klugen wissenschaftlichen Rat und seine Unterstützung in allen Belangen des Doktorandenlebens. Sein Engagement und die von ihm organisierten Lehrstuhl-Feiern und -Ausflüge sind keine Selbstverständlichkeit und tragen wesentlich zum guten Arbeitsklima bei. Danke, Reini!

Ich danke ebenso Professor Ferenc Krausz für die intensive Betreuung, die interessanten Diskussionen und natürlich für die Möglichkeit, in seinen Laboren unter Bedingungen zu forschen, die kaum einen Wunsch offen lassen. Dank seiner Hartnäckigkeit und seines Ideenreichtums wurde viele Labornächte lang, aber einige auch erfolgreich.

Den Postdocs Ralph Ernstorfer, Martin Schultze und Nick Karpowicz danke ich für die Bereitschaft, ihre Erfahrung, ihr Wissen und ihre Begeisterung für die Wissenschaft mit mir zu teilen. Ihr Rat war und ist unersetzlich. Nick Karpowicz danke besonders dafür, dass er unermüdlich clevere Ideen entwickelt und immer Zeit hat, sie mit einem zu diskutieren.

Ein grosser Dank gilt natürlich auch meinen Büro- und Labor-Kollegen, allen voran Annkatrin Sommer mit ihrer unvergleichlichen guten Laune und Motivation, mit der sie unser Damenbüro erfüllt. Hanieh Fattahi danke ich für ihre Freundschaft, ihr Engagement in der der bayrisch-persischen Völkerverständigung und für ihre Hilfe beim Verstehen nichtlinearer Propagationseffekte. Sie verdient in jedem Fall den Titel 'best colleague ever'. Martin Schultze, Ralph Ernstorfer, Nick Karpowicz, Alexander Paarmann, Annkatrin Sommer, Wolfgang Schweinberger, Michael Jobst, Tobias Latka, Clemens Jakubeit, Luciana Vidas, Simon Holzner, Michael Stanislawski, Adrian Cavallieri, Markus Fiess und Stefan Nepl bin ich zu grossem Dank für die gute Zusammenarbeit an den verschiedenen Experimenten verpflichtet. Aleander Guggenmos hat durch seine Expertise und sein grosses Engagement, uns immer mit den richtigen und immer neu verbesserten Spiegeln für die Attosekundenpulse zu versorgen und uns bei der Probenpräparation zu helfen, wesentlich zum Erfolg der Experimente beigetragen, vielen Dank!

Martin Schultze, Tim Paasch-Colberg und Matthias Bernert danke ich für das aufmerksame Korrekturlesen dieser Arbeit und ihre hilfreichen Anmerkungen.

Martin Garcia und Eeuwe Zijlstra von der Universität Kassel danke ich für die tolle Zusammenarbeit im TiO<sub>2</sub>-Projekt. Ihre Erkenntnisse und unsere Diskussionen sind für diese Arbeit wesentlich. Ebenso danke ich Vladislav Yakovlev, Mark Stockman und Vadym Apalkov, deren Erkenntnisse und Diskussionen einen grossen Beitrag zur Interpretation der beobachteten Dynamik in SiO<sub>2</sub> lieferten.



Peter Feulner vom Lehrstuhl E20 an der Technischen Universität München danke ich für die Hilfe und seinen umfassenden Rat in allen Fragen der Festkörperphysik.

Den Mitarbeitern der mechanischen Werkstatt am Max-Planck-Institut für Quantenoptik danke ich sehr für ihre hervorragende, präzise Arbeit, aber auch für ihre Vorliebe für Herausforderungen und ihr Engagement, wenn mal etwas schnell gehen muss. Vielen herzlichen Dank!

An dieser Stelle sei natürlich auch den Technikern der Attosekunden-Abteilung und den Mitarbeitern in der Verwaltung, im Besonderen Claudia Schenker, für die reibungslose Zusammenarbeit und die stete Hilfsbereitschaft gedankt.

Ivanka Grguras, Yunpei Deng, Wolfram Helml, Konrad Hütten, Johann Riemensperger, Alexander Schwarz, Bidoor Alsaif, Tran Trung Luu, Antoine Moulet, Mohammed Hassan, Tim Paasch-Colberg, Agustin Schiffrin, Sabine Keiber und allen anderen früheren und jetzigen Kollegen aus dem Labor für Attosekundenphysik und am Max-Planck Institut für Quantenoptik danke ich für die gute Zusammenarbeit im Labor. Die Treffen der Doktoranden innerhalb der International Max-Planck-Research-School, organisiert und hervorragend betreut von der unersetzlichen Frau Wild, waren immer aussergewöhnlich, sowohl im wissenschaftlichen als auch im persönlichen Austausch von Erfahrungen und Meinungen und auch mal Kritik. Den Organisatoren auf wissenschaftlicher Seite Matthias Kling, Peter Hommelhoff, Nick Karpowicz und Vladislav Yakovlev danke ich für ihr Engagement, uns Doktoranden einen Rahmen zu geben, um unser wissenschaftliches Profil regelmässig zu überprüfen und zu schärfen.

Die grossartige Unterstützung durch meine Familie und meinen Freundeskreis während der letzten Jahre hat wesentlich zum Gelingen dieser Arbeit beigetragen. Margarethe und Matthias danke ich für ihre Freundschaft und ihr Verständnis, wenn ich während der Strahlzeiten manchmal kaum Zeit für andere Dinge hatte. Ebenso danke ich Julia, Daniel, Alexandre, Stephi, Evi und meinen Stuttgarter Studienkollegen.

Mein ganz besonderer Dank für all die Unterstützung gilt meinen Eltern Monika und August, meinem Bruder Christoph und natürlich meinem Tobias.



# Elisabeth Monika Ludmilla Bothschafter

Munich, November 2013

---

Nationality: German  
Date of birth: 18<sup>th</sup> December 1985  
Place of birth: Zwiesel

---

## Education and training

2010-present            Doctoral candidate at the Technical University Munich  
Member of the International Max Planck Research School of Advanced Photon Science (IMPRS-APS)

2010                    Diplôme d'Ingénieur des Arts et Manufactures (Master of Engineering), Ecole Centrale Paris

2009                    Diploma in Physics *with distinction*, University of Stuttgart

2008-2009            Diploma thesis research project: *Generation and characterization of ultrashort UV and XUV pulses for studying electron dynamics in solids* at the Max Planck Institute of Quantum Optics in Garching

2006-2008            Advanced studies in General Engineering, Ecole Centrale Paris  
Participation in the T.I.M.E. double diploma program (T.I.M.E.: Top Industrial Managers For Europe)

2004-2009            Studies in Physics, University of Stuttgart

2004                    Abitur (general qualification for university entrance) at the Comenius-Gymnasium in Deggendorf

## Professional experience

11/2012-present      Project leader in the group of Prof. Dr. Krausz at the Ludwig-Maximilians Universität München and at the Max Planck Institute of Quantum Optics

01/2010-10/2012      Research assistant in the group of Prof. Dr. Kienberger at the Technical University of Munich and at the Max Planck Institute of Quantum Optics

08/2008-10/2009      Diploma student at the Max Planck Institute of Quantum Optics

07-10/2008            Intern at the Max Planck Institute of Quantum Optics

06-07/2007            Intern at the European Synchrotron ESRF in Grenoble